CYCLONE GLOBAL NAVIGATION SATELLITE SYSTEM (CYGNSS)

Algorithm Theoretical Basis Document Level 2 Wind Speed Retrieval		
	UM Doc. No.	148-0138
	SwRI Doc. No.	N/A
	Revision	Rev 6
	Date	14 September 2020
	Contract	NNL13AQ00C

SPACE PHYSICS RESEARCH LABORATORY

NASA

CYCLONE GLOBAL NAVIGATION SATELLITE SYSTEM (CYGNSS)

Algorithm Theoretical Basis Document Level 2 Wind Speed Retrieval		
	UM Doc. No.	**148-0138**
	SwRI Doc. No.	**N/A**
	Revision	**Rev 6**
	Date	**14 September 2020**
	Contract	**NNL13AQ00C**

Prepared by: Maria Paola Clarizia, Valery Zavorotny, Darren McKague, Chris Ruf Date: 09/14/2020

Approved by: _____ Date: 09/14/2020

Chris Ruf, CYGNSS Principal Investigator

Approved by: _____ Date: 09/15/2020

Tim Butler, CYGNSS SOC Manager

Released by: _____ Date: 14 September, 2020

Darren McKague, CYGNSS UM Project Manager

SPACE PHYSICS RESEARCH LABORATORY

SwRI

NASA

REVISION NOTICE

Document Revision History		
Revision	**Date**	**Changes**
PRE-RELEASE DRAFT	17 June 2013	n/a
INITIAL RELEASE	17 January 2014	L1 calibration and L2a correction added. Delay-Doppler range optimized. Time averaging added. Full 13-day nature run used for algorithm development and performance assessment.
REVISION 1	11 August 2014	L2 Retrieval algorithm modified to account for modifications in the GMF derivation
REVISION 2	03 November 2015	Section on L1b corrections removed, equations (8.8) and (8.13) revised, a few typos corrected. Equation numbering revised from Section 5 to Section 10.
REVISION 2 CHANGE 1	18 November 2015	Equation numbering revised from Section 5 to Section 10.
REVISION 2 CHANGE 2	19 November 2015	Typos corrected. Caption of figure 4 corrected. Documents 17790-ConOp-01 and 17790-SMDP-01 properly referenced;
REVISION 2 CHANGE 3	02 December 2015	Typos corrected. Caption of figure 4 corrected. Documents 17790-ConOp-01 and 17790-SMDP-01 properly referenced;
REVISION 3	20 August 2016	Section 9 updated to reflect new definition of L2 quality flags
REVISION 4	24 January 2017	a) Entire Description of L2 wind speed retrieval algorithm modified to be consistent with algorithm implemented by the SOC. b) Definition of modified effective scattering area introduced, and definition of L1b DDMA and L1b LES updated to be normalised by the modified effective scattering area; c) Description of the original L2 algorithm developed to meet the performance requirements has been moved to appendix A. d) Appendix B added to describe all the lookup tables used by the algorithm, and the content of the L1 and L2 NetCDF files

		e) Format and numbering of Sections, figures and equations, and references made consistent across the whole document
REVISION 5	17 Aug 2018	a) Generate geophysical model function (GMF), to map 10 m referenced ocean wind speed to CYGNSS L1 observables, empirically from matchups between measurements and near-coincident ground reference winds. b) Generate two different GMFs, one for fully developed seas (FDS) and the other for young seas with limited fetch (YSLF). FDS GMF is generated using ECMWF and GDAS numerical prediction model ground reference winds. YSLF GMF is generated using SFMR measurements on hurricane hunter aircraft. c) add debiasing adjustment to final minimum variance FDS wind speed to match global cumulative distribution function to NWP matchup database.
REVISION 6	14 Sep 2020	Rev 6 incorporates the changes made from the v2.1 to v3.0 L2 wind speed data product. a) Update generation of FDS GMF to use globally distributed matchups with MERRA-2 reference wind speeds with CDF-matching method. b) Update generation of YSLF GMF to use matchups with HWRF reference wind speeds during storm overpasses. c) Modify YSLF retrieval algorithm to be a tapered linear combination of the retrievals produced from the FDS and YSLF GMFs, with more weight given to FDS at low wind speeds and more to YSLF at high wind speeds.

Table of Contents

1 INTRODUCTION AND SUMMARY 1

2 OVERVIEW AND BACKGROUND 2

2.1 Science Objectives and Algorithm Requirements 3
2.2 Measurement Overview 4
2.3 Algorithm Approach 6

3 MEASUREMENT DESCRIPTION 7

3.1 Satellite Constellation and Sampling 7
3.2 Observatory Platform 7
3.3 Delay Doppler Mapping Instrument 7
3.4 Delay Doppler Map Level 0 Data 10
3.5 Delay Doppler Map Level 1 Data Products 11

4 FORWARD MODEL 14

4.1 Propagation 14
4.2 Rough Surface Scattering 15
4.3 Conclusions on Rough Surface Scattering 31
4.4 Delay and Doppler Coordinate System 32
4.5 Mean Power and Signal-to-Noise Ratio for the GPS Reflected Signal 34
4.6 Speckle Noise 42

5 L2 WIND SPEED RETRIEVAL ALGORITHM 45

5.1 Sample populations for GMF training data 46
5.2 DDM Observables: DDMA and LES 47
5.3 Time Averaging 50
5.4 Generation of Geophysical Model Functions 52
5.5 Wind Estimation using the GMF 57
5.6 FDS Wind Speed Additional Processing 57
5.7 YSLF Wind Speed Additional Processing 58
Tapered blending of FDS and YSLF wind speeds 58
5.8 Quality Control Flags in the Retrieval Algorithm 60

6 REFERENCES 61

APPENDIX A: RETRIEVAL PERFORMANCE ASSESSMENT USING ON-ORBIT OBSERVATIONS 67

A.1. FDS Wind Speed validation and performance characterization 67
A.2. YSLF Wind Speed validation and performance characterization 67

APPENDIX B: IMPLEMENTATION OF ON-ORBIT WIND SPEED RRETRIEVAL ALGORITHM 70

B.2 Derivation of Coefficients for Minimum Variance Estimator 72
B.2.1 Minimum Variance Coefficients LUT 74
B.3 Debiasing Maps 74
B.4 Time-averaging LUT 76
B.5 Standard Deviation of the retrieval error LUT 76
B.6 L2 Data Dictionary 83

1 Introduction and Summary

The CYGNSS Project implements a spaceborne earth observation mission designed to collect measurements of ocean surface winds through variations in the direct vs. reflected Global Positioning System (GPS) signals. The observatory portion of this mission consists of a constellation of eight satellites. The CYGNSS mission objective is to provide new information about ocean surface winds in Tropical Cyclones (TC), enabling advances in the knowledge of TC genesis and intensification.

The CYGNSS goal is to understand the coupling between ocean surface properties, moist atmospheric thermodynamics, radiation, and convective dynamics in the inner core of TCs. The goal of CYGNSS directly supports the NASA strategic objective to enable improved predictive capability for weather and extreme weather events. Near-surface winds are major contributors to and indicators of momentum and energy fluxes at the air/sea interface. Understanding the coupling between the surface winds and the moist atmosphere within the TC inner core is key to properly modeling and forecasting its genesis and intensification. Of particular interest is the lack of significant improvement in storm intensity forecasts over the past two decades, relative to forecasts of storm track. Advances in track forecast have resulted in large part from the improvements that have been made in observations and modeling of the mesoscale and synoptic environment surrounding a TC. The CYGNSS team hypothesizes that the lack of an accompanying improvement in intensity forecasting is in part due to a lack of observations and proper modeling of the TC inner core. The inadequacy in observations results from two causes:

1. Much of the inner core ocean surface is obscured from conventional remote sensing instruments by intense precipitation in the eye wall and inner rain bands.

2. The rapidly evolving genesis and intensification stages of the TC life cycle are poorly sampled by conventional polar-orbiting, wide-swath imagers.

CYGNSS addresses these two limitations by combining the all-weather performance of GPS based bistatic scatterometry with the spatial and temporal sampling properties of a constellation of observatories. The constellation consists of individual GPS bistatic radar receivers flown on 8 microsatellites. This provides the ability to measure the ocean surface winds with high temporal resolution and spatial coverage under all precipitating conditions, up to and including those experienced in the hurricane eyewall. The 8 microsatellites are launched on a Deployment Module (DM) that is attached to the NASA government furnished equipment (GFE) launch vehicle.

The baseline CYGNSS instrument is a Delay Doppler Mapping Instrument (DDMI) which resides on each observatory in the constellation. The DDMI is a Global Navigation Satellite System (GNSS) Receiver-Remote sensing Instrument. Each instrument will use two nadir pointing antennas for collecting reflected GPS signals and a zenith facing antenna to collect direct GPS signals. The GPS transmission frequency enables the instrument to make surface scattering observations during most precipitation conditions.

2 Overview and Background

For some years, GPS receivers have been used to provide position, velocity, and time measurements to satellite platforms in low Earth orbit. In a similar way, they are also used for ground-based navigation. Beyond navigation however, GPS signals have been increasingly used for remote sensing. Signals at L-band – with a bandwidth between 2 and 20 MHz – are broadcast globally from an altitude of 20,000 km (~12,427 mi) and are used to measure, amongst other things, tectonic plate motion and ionospheric and tropospheric parameters.

The United Kingdom Disaster Monitoring Constellation (UK-DMC-1) space-based demonstration mission showed that a microsatellite-compatible passive instrument potentially could make valuable geophysical measurements using GPS reflectometry. The left side of the figure below diagrams how the process works. The direct GPS signal is transmitted from the orbiting GPS satellite and received by a right-hand circular polarization (RHCP) receive antenna on the zenith (*i.e.* top) side of the spacecraft that provides a coherent reference for the coded GPS transmit signal. The signal that is scattered back from the ocean surface is received by a downward looking left-hand circular polarization (LHCP) antenna on the nadir side of the spacecraft. The scattered signal contains detailed information about the ocean surface roughness statistics, from which local wind speed can be retrieved.

The image on the right below shows scattering cross section as measured by UK-DMC-1 and demonstrates its ability to resolve the spatial distribution of ocean surface roughness. This type of scattering image is referred to as a Delay Doppler Map (DDM). A DDM exhibit a typical horseshoe-like shape, which is linked to the space-to-DD coordinate transformation and consequent reshape of the spatial scattered power. The delay-Doppler coordinate system is explained in detail in Section 4.3.

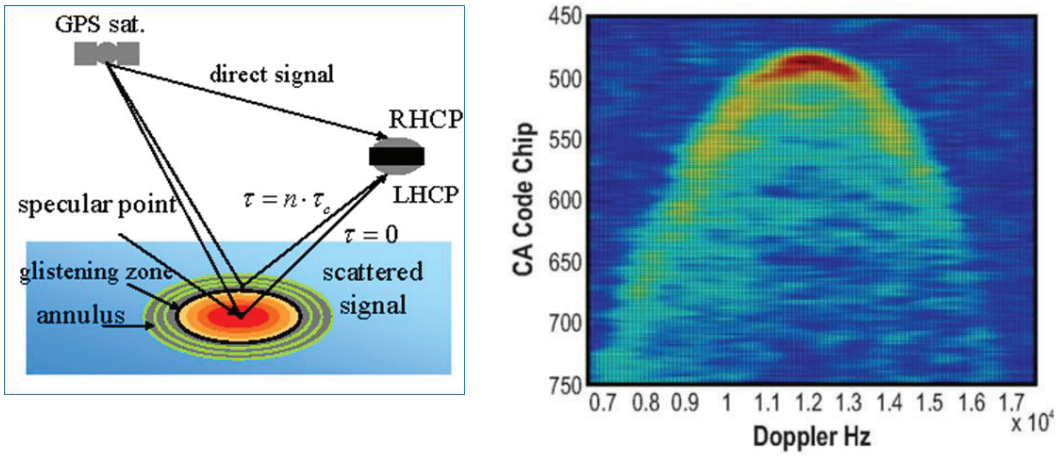

Figure 1. [left] GPS signal propagation and scattering geometries for *ocean surface bistatic quasispecular scatterometry*. The position of the spacecraft is determined from the direct GPS signal; the surface winds are determined by the indirect signal scattered off the ocean surface. Combining the position and scattering information allows for the creation of Delay Doppler Maps (DDM), from which ocean surface wind speeds can be inferred. [right] An example DDM measured by the UK-DMC-1, showing the spatial distribution of the ocean surface scattering. Scattering cross section is plotted as a function of Doppler Shift (x-axis) and relative propagation time of flight (y-axis), which is measured in units of Coarse Acquisition GPS Code, or "Chips".

The forward scattering is dominated by specular reflection. The reflected signal comes mostly from a point where a specular reflection occurs, called Specular Point (SP), and a variable area around the SP called the glistening zone, where quasi-specular reflections are in place, and where scattered power is redirected towards the receiver. A very calm sea (flat surface) would therefore only produce a strong specular reflection from the SP, whereas a rougher sea causes less power to be scattered from the SP, and more power scattered from the glistening zone, which expands with increasing roughness. The wind and sea surface roughness have therefore an impact on both the distribution of the scattered power, and the effective scattering area.

Stronger wind and sea surface roughness induce two main types of changes in the DDM. One is a decrease in the peak power of the horseshoe shape in the DDM, corresponding to the power at the specular point; the other is the increase in the power along and between the horseshoe branches, which stretch towards larger delays and Doppler frequencies. The horseshoe shaped power pattern in the DDM essentially represents the power scattered in space by the whole glistening zone, and the increase of the power along and between the branches of the horseshoe shape is a sign of increasing size of the glistening zone.

2.1 Science Objectives and Algorithm Requirements

The CYGNSS science goals are enabled by meeting the following mission objectives:

- Measure ocean surface wind speed in most naturally occurring precipitating conditions, including those experienced in the tropical cyclone eyewall;
- Measure ocean surface wind speed in the tropical cyclone inner core with sufficient frequency to resolve genesis and rapid intensification.

The CYGNSS baseline science requirements are:

a) The baseline science mission shall provide estimates of ocean surface wind speed over a dynamic range of 3 to 70 m/s as determined by a spatially averaged wind field with resolution of 5x5 km.
b) The baseline science mission shall provide estimates of ocean surface wind speed during precipitation rates up through 100 millimeters per hour as determined by a spatially averaged rain field with resolution of 5x5 km.
c) The baseline science mission shall retrieve ocean surface wind speed with a retrieval uncertainty of 2 m/s or 10%, whichever is greater, with a spatial resolution of 25x25 km.
d) The baseline science mission shall collect space-based measurements of ocean surface wind speed at all times during the science mission with the following temporal and spatial sampling: 1) temporal sampling better than 12 hour mean revisit time; and 2) spatial sampling 70% of all storm tracks between 35 degrees north and 35 degrees south latitude to be sampled within 24 hours.
e) The CYGNSS project shall conduct a calibration and validation program to verify data delivered meets the requirements in sections 4.1.1a, 4.1.1b, 4.1.1c and 4.1.1d within

individual wind speed bins above and below 20 m/s.

f) Support the operational hurricane forecast community assessment of CYGNSS data in retrospective studies of new data sources.

2.2 Measurement Overview

GPS-Reflectometry (GPS-R) exploits pre-existing signals of opportunity from the Global Positioning System (GPS) constellation. It measures the direct GPS signal, received through a zenith antenna, to pin-point the position of the transmitting and receiving satellite, and the reflected GPS signal from the surface of the ocean, through a downward pointing antenna, for retrieval of sea surface wind and roughness. GPS-R is based upon scattering in a bistatic geometry, where the transmitter and receiver are not collocated on the same platform. An illustration of the GPS-R overview and measurement is shown in Figure 2. The transmitting GPS satellites are a constellation of up to 32 Medium- Earth orbit Satellites in operation at any given time. They are in six different orbital planes, and have a near circular orbit with an inclination angle of 55◦, an orbital period of about 12 hours, and an altitude of about 20200 km.

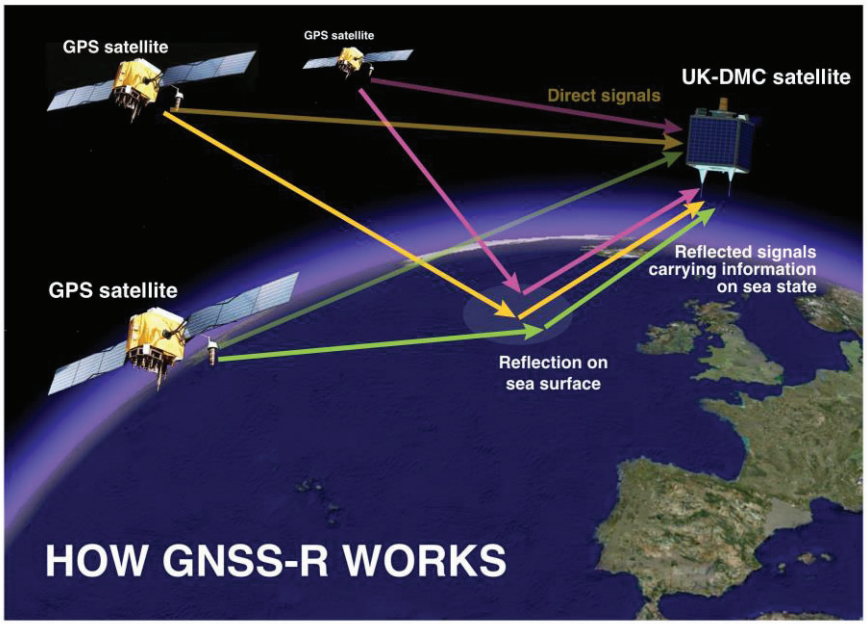

Figure 2. Measurement principle of GPS-Reflectometry over the ocean.

The CYGNSS mission is comprised of 8 microsatellites deployed into a common orbit plane of 35° inclination at ~525 km altitude. Each S/C is able to track up to four SP simultaneously, and generate a 1-second DDM for each SP. This results in 32 wind measurements (32 DDMs) per second across the globe, providing a wind field imagery of TC genesis, intensification and decay with unprecedented spatial and temporal resolution (Figure 3).

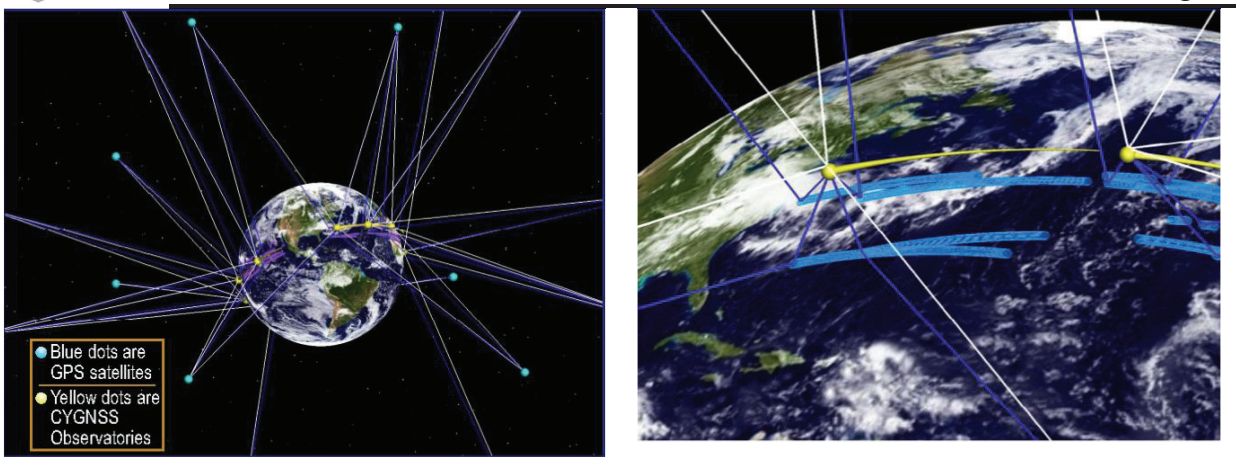

Figure 3. (left) overview of GPS Satellites and CYGNSS observatories. (right) illustration of the four simultaneous specular acquisitions for each observatory.

Each CYGNSS observatory is equipped with a Digital Doppler Mapping Instrument (DDMI). The DDMI generates DDMs continuously at a low data rate, which provides a source for ocean roughness measurements across the ocean. In special situations, such as when passing over an active tropical cyclone, the instrument is operated in Raw IF Mode, where ~60 seconds of raw sampled data is accumulated. This allows researchers to fully analyze and re-analyze the acquired data using different processing schemes to ensure that the nominal DDM mode of operation is not losing important geophysical data.

Each DDM pixel is obtained through a cross-correlation of the received scattered GPS signal with a locally generated replica of the C/A code of the transmitted signal, for the pair of delay-Doppler coordinate corresponding to that pixel. Such cross-correlation is done over 1 ms, and it is heavily affected by speckle noise, so that a number of incoherent accumulation of consecutive cross-correlation values is necessary to mitigate the noise. The incoherent accumulation time for DDM measured spaceborne is 1 second. A schematic of the blocks required to process the received signal to obtain a DDM is shown in Figure 4.

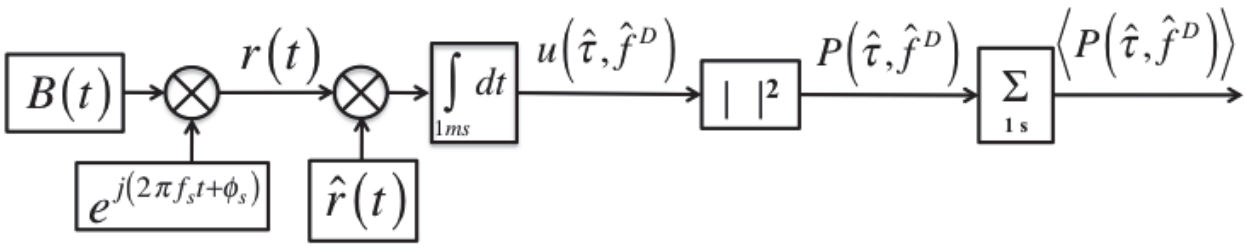

Figure 4. Schematic of a GPS receiver (modified from Gleason et al., 2005).

DDMs constitute the fundamental measurement for spaceborne GNSS-R, to which inversion algorithms are then applied directly to estimate the sea surface wind and roughness.

2.3 Algorithm Approach

There are three popular approaches for extracting sea surface winds from GPS-R DDMs. The first approach relies on a forward scattering model to simulate DDMs. This model, developed by Zavorotny and Voronovich [2000], and described in details in Section 4, generates the delay-Doppler scattered power as a function of geometrical parameters, receiver/antenna parameters, and sea surface parameters. The latter are so-called Mean-Square Slope (MSS), which represent the sea surface roughness, and are related to the sea surface wind speed through MSS-to-wind relationships [Elfouhaily et al., 1997, Katzberg et al., 2006]. The MSS is therefore retrieved by fitting the simulated DDMs to the measured ones, usually in either a Least-Square (LS) or Maximum likelihood (ML) sense [Germain et al., 2004, Clarizia et al, 2009]. For airborne GPS-Reflectometry, the Doppler spreading is so small that it is usually sufficient to apply such fitting to the delay Waveforms, namely the scattered power as a function of delays, at the Doppler shift of the specular point [Garrison et al., 1998, 2002, Komjathy et al., 2004, Gleason et al., 2005]. In some cases, a matched filter approach has been applied to delay waveforms, rather than a full Least-Square fitting [Katzberg et al., 2000], but the overall results do not change. Generally speaking, this fitting approach can be applied to a full DDM, as well as to waveforms derived from a DDM (i.e. delay waveforms, integrated delay and Doppler waveforms, etc.). Note once again that this approach usually extracts the optimal MSSs, from which the winds are then derived.

The second type of algorithm is based on the use of a so-called DDM observable, and an empirical regression approach. A DDM direct observable or direct descriptor is a quantity derived from the DDM, which varies with respect to changing underlying wind and roughness in the DDM. Examples of DDM observables are the average or volume of DD pixels around the specular point (DDMA or DDMV, [Marchan-Hernandez et al, 2008, 2010]), different types of distances defined within the DDM ([Rodriguez-Alvarez et al., 2013]), the rising edge slope of the waveform obtained as DDM integration along the Doppler frequencies, known as Integrated Delay Waveform, or IDW [Clarizia et al., 2014], and the width of the waveform obtained as DDM integration along the delays, known as Integrated Doppler Waveform, or IDoW [Clarizia et al., 2013] The approach is usually to calculate these quantities from the measured DDMs, regress them against the match-up winds measured locally by some other sources or instruments, and extrapolate the relationship between the observable and the wind through a Look-Up Table (LUT) function. In this case, there is no intermediate step of MSS calculation, since the measured observable is directly converted into a wind estimate.

A third approach is a hybrid algorithm, which combines the two approaches described above [Gleason, 2006]. It extrapolates the Normalized Radar Cross Section (NRCS) at the specular point from the DDMs, through inversion of the theoretical model, and then regresses the NRCS values against the wind measured by match-ups, and converting the NRCS into a wind measurement through the definition of a LUT function.

3 Measurement Description

3.1 Satellite Constellation and Sampling

The satellite constellation configuration and its resulting spatial and temporal sampling characteristics are described in the following CYGNSS Project Engineering Memoranda:

- UM EM No. 148-0132, On the Dependence of Science Coverage on Launch Time
- UM EM No. 148-0133, Specular Point Algorithm for GPS Reflected Signals
- UM EM No. 148-0134, Effect of Satellite Clustering on Science Coverage

3.2 Observatory Platform

The observatory platform design and performance are described in a series of CYGNSS Project Engineering Memorandums and summarized in the following released document of Concept of Operations:

- SwRI EM No. 17790-CONOP-01, Cyclone Global Navigation Satellite System (CYGNSS) Concept of Operations Plan

The software associated with observatory operation and related ground operations is described in the CYGNSS released document:

- SwRI EM No. 17790-SMDP-01, Software Management & Development Plan

3.3 Delay Doppler Mapping Instrument

Each CYGNSS spacecraft carries a Delay Doppler Mapping Instrument (DDMI) capable of locating and tracking GPS signal reflections on the Earth's surface. A DDMI consists of two Earth pointing nadir antennas with low noise amplifiers and internal blackbody calibration target, a single upward (space) pointing zenith antenna with a low noise amplifier and internal blackbody calibration target, and a Delay Mapping Receiver (DMR) electronics unit. These components, as they are mounted on the CYGNSS platform, are illustrated in Figure 5.

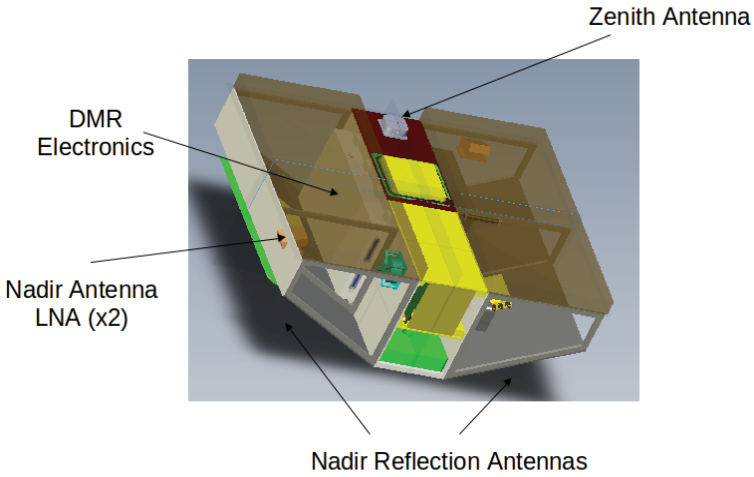

Figure 5. The Delay Doppler Mapping Instrument CYGNSS platform configuration.

The instrument is passive, with the signals being transmitted from the Global Positioning System (GPS) constellation. The instrument autonomously tracks and cross correlates the reflected signal power over a range of delay and Doppler bins. The DDMI outputs 4 DDMs every second to the S/C, which are compressed, sent to the ground, and calibrated into the Level 1 data products.

3.3.1 Zenith (Direct Signal) Antenna

The DDMI zenith antenna and processing channels serve two key functions. The first is to generate a navigation solution for the CYGNSS spacecraft, providing real-time position, velocity and time (PVT) information at 1 Hz. This is performed by tracking 4 or more direct GPS signal transmissions, making pseudorange measurements from each and generating an estimate of the receiver PVT data. The second function is to provide a direct signal power measurement for all of the tracked GPS satellites used in the navigation solution. This second function is an additional requirement on the navigation receiver, in that traditional satellite navigation usually does not place much emphasis on the strength of the tracked signal and rarely uses the received power for anything other than a general indicator of signal quality. However, in the case of GNSS-R the absolute power of the received signals is of critical importance. This presents an interesting problem when using GNSS constellations (including GPS): The transmit power of the GPS signal (and associated transmit antenna gain) is unpublished and only approximately known.

The solution to this problem is to use the received direct signal levels to map the effective isotropic radiated power (EIRP) of each GPS satellite. This is made possible because the direct signal does not undergo any surface scattering which makes the power relatively straightforward to estimate using the basic radar equation. With the positions of the CYGNSS receiver and transmitting GPS satellite known it is possible to accurately estimate the propagation path loss. Additionally, the zenith antenna gain pattern must be calibrated as a function of the azimuth and elevation of the incoming signal. Using these parameters, the EIRP of the transmitted GPS signal in the direction of the specular reflection point can be estimated from the measurement of the received direct signal power. This value is needed as an input into the Level 1b calibration calculation of the bistatic radar cross section, which is one of the basic surface observables used for wind retrieval.

3.3.2 Nadir (Reflected Signal) Antennas

Surface reflection signals are collected by two downward looking nadir antennas, which together result in the surface footprint shown in Fig. 6. Referring to Figs. 5-6, the nadir antennas are mounted on the spacecraft to project their patterns onto the surface. This high signal to noise coverage pattern in the cross track direction acts to capture signal reflections to the starboard (right) and port (left) sides of the satellite direction of motion.

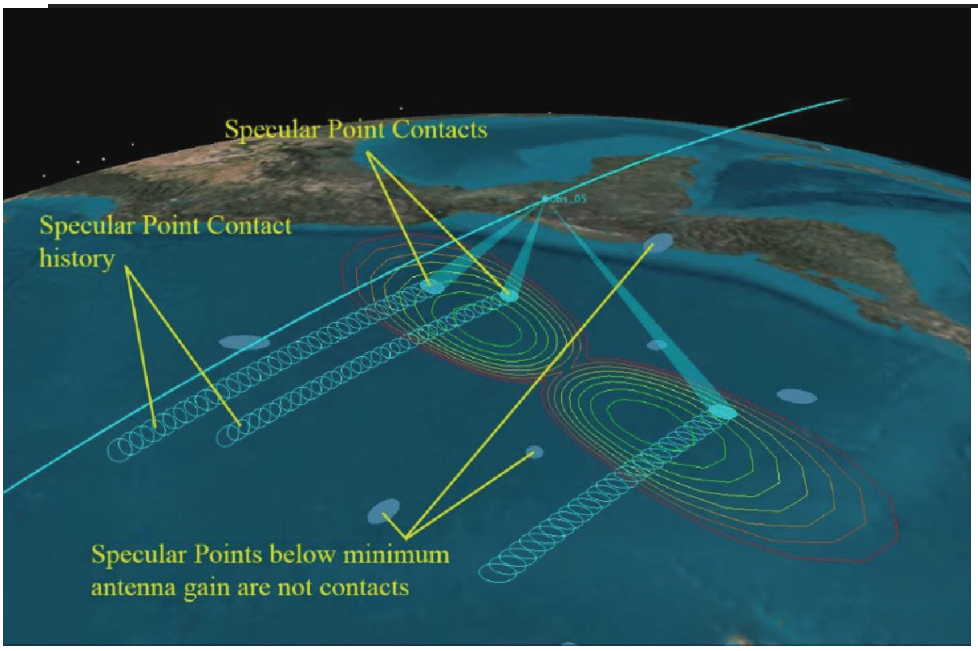

Figure 6. CYGNSS nadir antenna surface coverage footprint. The outermost (red) gain contour represents the threshold for acceptable received signal strength, inside of which scattered signals can be converted to near-surface wind speed with uncertainties that meet or exceed the Level 1 mission requirement.

3.3.3 Front End Receiver and Backend Digital Processor

The complete DDMI processing chain is shown in Figure 7, which includes both receiver RF front end components, on-board digital receiver back-end stages and ground based Level 1 data product processing steps.

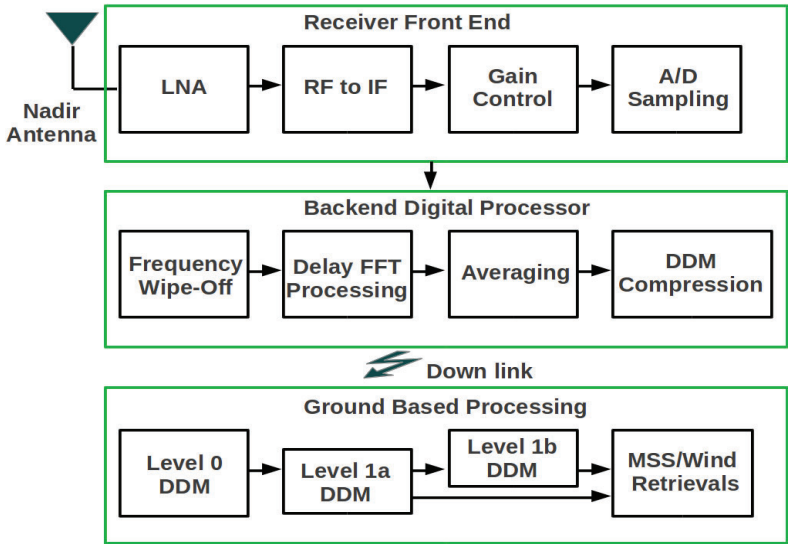

Figure 7. DDMI signal processing chain. Front end receiver, consisting of RF to IF and digitization stages, and the Back-end Digital Processor constitute the stages of DDM generation.

Upon acquisition by one of the nadir antennas, the signal goes through several stages of RF processing before it is sampled for the digital processor. Following, the Level 0 DDM product generated by the DMR is then calibrated in several stages on the ground at the science operations center. Referring to Figure 7, the hardware and processing stages of the DDMI processing chain are summarized below.

1. The signal is acquired by one of the two Nadir antennas.
2. The signal travels over a short cable and enters the low noise amplifier. This initial amplification stage largely determines the overall receiver noise figure.
3. The signal then travels to the DMR electronics where it is down converted and filtered in several stages by the RF front-end, transforming it from the L1 GPS frequency to an Intermediate Frequency (IF) suitable for digital processing.
4. The signal is then amplified by a gain control. The purpose of this last stage of amplification is to center the signal level into the optimal active range of the Analog to Digital (A2D) convertor.
5. The signal is then 2-bit sampled over 1 millisecond by the A2D convertor for digital processing by the DMR firmware.
6. The first stage of digital processing is the application of a digital carrier wipe-off technique to the incoming sample vector. This consists of generating sine and cosine sampling vectors at each Doppler frequency bin and mixing them with the incoming sampled signal.
7. The signal is then correlated with the unique GPS signal spreading code, isolating the surface reflection to the GPS satellite it originated from. The delay processing is implemented across the entire range of time samples using FFT based techniques. A multiplication of the GPS code and the carrier wiped off signal in the frequency domain results in a 1ms correlation at every delay in the time domain after an Inverse FFT is performed. This process is repeated at every frequency bin in the DDM and results in a single look 1ms DDM.
8. 500 single look DDMs are averaged over 0.5 seconds to produce the non-coherently summed DDM sent to the spacecraft. This averaging is performed to reduce the speckle and thermal noise present in the 1ms DDM looks.
9. The 0.5 second DDM's are then compressed on the spacecraft and sent to the ground. The DDM compression algorithm is documented in detail in [Ruf, 2013]. The compressed DDMs are then transmitted to the ground for processing at the Science Operations Center at the University of Michigan.

On the ground the raw Level 0 data is unpacked, and the Level 1a and Level 1b calibration algorithms are applied. The ocean mean square slope and wind retrievals can use either of the Level 1a or Level 1b data products for ocean roughness or wind speed estimation.

3.4 Delay Doppler Map Level 0 Data

The DDMI outputs (up to) 4 delay Doppler maps in uncalibrated counts to the spacecraft every second. These DDMs are be converted into the calibrated level 1 data products. An illustration of a raw Level 0 DDM and a Level 1a DDM calibrated to signal power units of Watts are shown

in Figure 8. The algorithms for converting Level 0 DDMs to Level 1 DDMs is described in detail in the Level 1 Calibration ATBD.

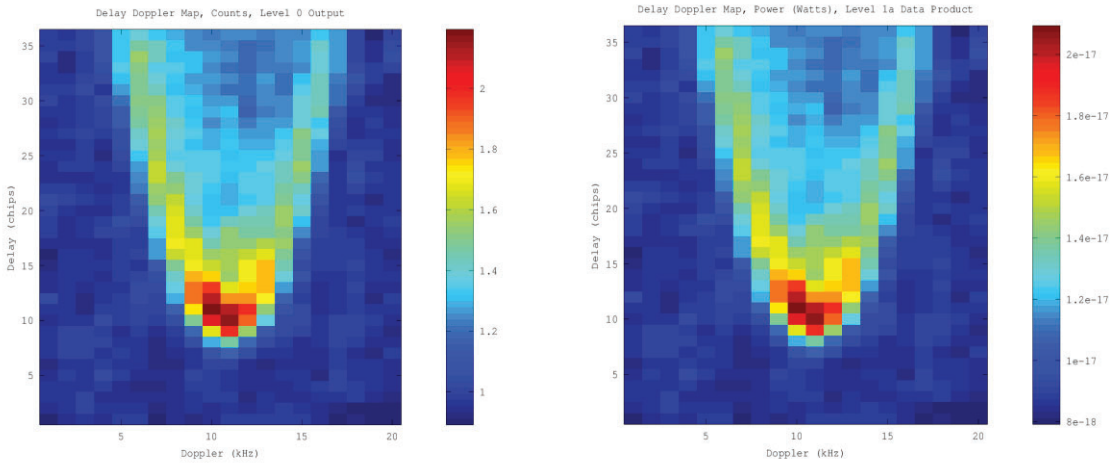

Figure 8. (left) raw Level 0 DDM in uncalibrated counts. (right) Level 1a calibrated DDM in units of Watts. DDMs generated by the CYGNSS End-to-End Simulator. Note the different magnitude scales before and after the Level 1a calibration.

The Level 0 raw data output by the DDMI to the spacecraft is a result of several levels of analog RF and digital processing steps. The resulting Level 0 DDM is in units of processed counts. This DDM is then compressed as detailed in (reference: DDM compression algorithm) and sent to the ground for calibration into the Level 1a and Level 1b data products.

3.5 Delay Doppler Map Level 1 Data Products

Both Level 1 data products are provided as a two dimensional DDM grid of floating point numbers. The content and units of each of the Level 1a and Level 1b products is listed below.

3.5.1 Level 1a Data Product and Calibration Approach

The Level 1a data product consists of a DDM calibrated to the units of Watts (in 1 second). Every DDM produced by the delay mapping receiver is calibrated to Level 1a product power values. There are three types of calibration environments and scenarios, each with specific input signal requirements. Below is a list of each scenario and the signals needed;

1. Pre-launch laboratory calibration: Black body load source. GNSS Signal simulator.
2. Regular on-orbit calibration: Black body load source. Estimate of antenna noise temperature over the open ocean.
3. Beacon on-orbit calibration: Ground based GNSS signal generator.

Pre-launch calibration in the lab was performed using a variety of known input noise temperatures. With two different input noise values it will be possible to perform initial estimates of the instrument calibration coefficients prior to launch.

The on-orbit approach is detailed in the Level 1 Calibration ATBD and involves making measurements with the instrument switched to the black body load source as well as over well modeled ocean noise temperatures.

The beacon calibration occurs occasionally and involves the reception of a beacon generated DDM signal, which can be used independently to re-validate the calibration coefficients used to generate the Level 1a product.

The Level 1a calibrated delay Doppler maps is provided as a data product to users as well as fed into the Level 1b algorithm for conversion to BRCS values.

3.5.2 Level 1b Data Product and Calibration Approach

The Level 1b data product consists of a calibrated DDM map of bistatic radar cross section values in units of dB.

The Level 1b calibration is performed after the Level 1a calibration and uses an extensive set of external meta-data to convert the Level 1a power in Watts to a DDM map of BRCS values. This conversion is done for every DDM and requires the following external information:

1. Absolute power, delay and Doppler of the direct signal. The GPS satellite processed in the DDM is tracked by the CYGNSS spacecraft navigation receiver, which provides an estimated of the GPS satellite signal to noise (which can then be converted to absolute power), the tracked delay code phase and Doppler.
2. The CYGNSS satellite GPS time, position and velocity in the Earth Centered Earth fixed (ECEF) reference frame and the receiver clock error terms. This is provided by the CYGNSS navigation receiver.
3. The GPS satellite position and velocity in the Earth Centered Earth fixed (ECEF) reference frame and clock error terms. This is downloaded from the International GNSS service (IGS) daily.
4. Detailed knowledge of the gain pattern and orientation of the CYGNSS spacecraft nadir and zenith antennas.

Information which is not directly provided as part of the Spacecraft telemetry downlink or external public GNSS services is calculated on the ground by the Science Operations Center (SOC) at the University of Michigan and includes,

1. An accurate geolocation of the specular reflection point in the Earth Centered Earth fixed (ECEF) reference frame.
2. The GPS satellite transmit power.
3. The GPS satellite antenna gain at the observation reflection geometry.
4. The path distances between the GPS satellite and specular point and between the specular

point and the CYGNSS receiving spacecraft.

5. The CYGNSS satellite antenna gain, calculated from the reflection geometry (as an azimuth and indecent angle) and the detailed knowledge of the antenna patterns.
6. The path distance between the GPS satellite and the CYGNSS spacecraft. For use in estimating the GPS satellite transmit power.
7. The effective scattering area on the surface of each delay/Doppler bin. Calculated as a function of the reflection geometry using the CYGNSS end-to-end simulation (E2ES).

The above parameters are then combined as described below to convert the Level 1a DDM power values into estimates of the bistatic radar cross section (BRCS) using the derived forward model. This algorithm is described in detail in the Level 1 Calibration ATBD.

4 Forward Model

4.1 Propagation

CYGNSS uses the GPS L1 frequency (1575 MHz) which exhibits negligible rain attenuation, even under heavy precipitating conditions. Nonetheless, the forward model accurately for rain attenuation, G_{rain}, using the formula

$$G_{rain} = \exp(-\alpha h(\csc\theta_t + \csc\theta_r)) \tag{4.1}$$

where h is the freezing height in km, α is the specific attenuation (dB/km), and θ_t and θ_r are the elevation angles to the transmitter and receiver, respectively. Note that all of these parameters will vary over the ocean surface, and this spatial variation is included in our modeling. For simplicity, the current rain attenuation model assumes that the rain rate is constant from the surface up to freezing height.

The specific attenuation α is obtained from the ITU R838-3 model

$$\alpha = aR^b \tag{4.2}$$

where R is the rain rate (mm/hr) and the coefficients a and b for circular polarization at the GPS L1 frequency are $a = 24.312 \times 10^{-5}$ and $b = 0.9567$. In the model, the values for the coefficients have been developed from curve-fitting to power-law coefficients derived from scattering calculations.

Figure 9 shows a plot of rain attenuation versus rain rate for a freezing height of 6 km. In the figure, each curve corresponds to a different elevation angle (the elevation angle to the receiver and transmitter are assumed equal, as would be the case at the specular point).

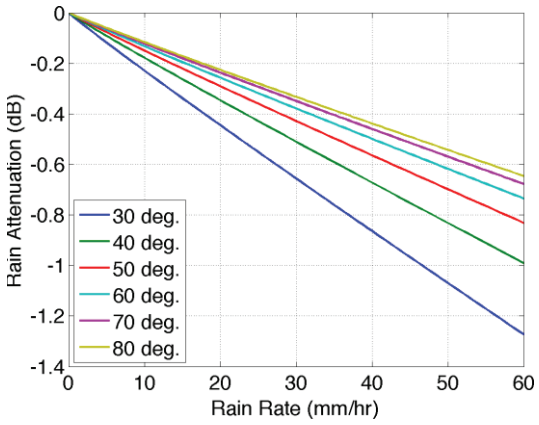

Figure 9. Rain attenuation versus rain rate for various elevation angles.

It should be noted that, in simulated hurricane wind fields, extremely large rain rates have been observed; however these convective cells are highly localized, move very rapidly, and evolve very rapidly. While they can have a very high rain rate, it may only be for a few minutes. So the peak rain rates are very high, but only occur for brief periods in fast-moving cells. Furthermore, the

nature of the GPS ambiguity function causes the rain field to be effectively smoothed over approximately a 20 km area (in the same way wind fields are smoothed), so that the effects of small regions of highest rain attenuation are effectively reduced.

4.2 Rough Surface Scattering

4.2.1 Introduction

In GNSS bistatic radar, the complex amplitude of the received signal (the voltage) is cross correlated with a replica of emitted signal over a coherent integration time, T_i. Frequently, this procedure is called a match-filter signal processing. The end result of this type of coherent signal processing is an ability to form a synthetic footprint which would ultimately determine the shape of the recorded 1D waveform, or 2D delay-Doppler map, and the spatial resolution of the GNSS bistatic radar. For every epoch t_0 the code cross-correlation relative to the received signal u taken at a variety of delays, τ, can be expressed as the integral [Parkinson et al, 1996, Zavorotny and Voronovich, 2000]

$$Y(t_0,\tau,f_c)=\int_0^{T_i} a(t_0+t')u(t_0+t'+\tau)\exp(2\pi i f_c t')dt' \tag{4.3}$$

Here T_i is the coherent integration time, and $a(t)$ is the replica of the PRN code sequence taking values of {-1,+1} on a time duration τ_c. The coherent integration time T_i should be comparable or smaller than the coherence time τ_{cor} of the scattered field at the receiver point in order to perform the convolution procedure (4.1) with linear phase shift between replica *a(t)* and signal *u(t)*. The oscillating factor containing f_c is meant to compensate for a possible Doppler shift of the signal *u(t)* associated with this phenomenon. For signals received from spacecraft, the signal coherence time τ_{cor}, has been observed to be on the order of 1ms [Gleason et al., 2005, Gleason, 2006], while signals received from aircraft can remain coherent for considerably longer durations, on the order of 5-10 ms depending on aircraft speed and altitude.

Only scattered waves with equal time delays and equal Doppler shifts could be successfully aligned with the code replica in order to produce maximum correlation according to (4.3), and it always happens within a so called glistening zone caused by a random distribution of the surface slopes. The size of the glistening zone is driven by the variance of surface slopes, where the larger the variance of surface slopes the larger the glistening zone extends across the surface.

The scattering toward the receiver is produced mostly by specular reflections from a statistical ensemble of large-scale (larger than several radio wavelengths) slopes of the surface. Therefore, the strongest scattered signal comes only from the center of the glistening zone near the nominal specular point on the mean sea surface. Away from the glistening zone, the contribution from the quasi-specular reflections diminishes, eventually to be replaced with significantly weaker diffraction scattering from a small-scale surface component. Here we neglect this type of scattering as it is too weak to make a significant contribution to the total received signal power. Using this understanding for the physical scattering mechanism, we can apply a Kirchhoff theoretical model to estimate the expected scattering behavior [Bass and Fuks, 1979]. In essence, we are combining

a multitude of "smooth" reflection surfaces together to represent the signal scattering from a rough ocean surface, where every point on the surface is approximated with a local tangent plane.

The scattered GNSS signal *u(t)* arriving at the receiver position $\vec{R}_r$ can then be modeled by the integral taken over the mean sea surface [Zavorotny and Voronovich, 2000]:

$$u(\vec{R}_r,t)=\int D(\vec{\rho})a[t-(R_0(t)+R(t))/c]g(\vec{\rho},t)d^2\rho \tag{4.4}$$

Where $D(\vec{\rho})$ is the amplitude footprint of the receiver antenna; $a(t)$ is the GNSS signal PRN code; $R_0(t)$ and $R(t)$ are distances to the transmitter and the receiver, respectively, to some point $(\vec{\rho},z=\zeta(\vec{\rho},t))$ on the "smoothed" rough sea surface with an elevation of $\zeta(\vec{\rho},t)$, fluctuating about the mean surface level. Over the individual local tangent planes the Earth's curvature is neglected; $\vec{\rho}=(x,y)$; the transmitter and receiver positions are in the $x = 0$ plane, and z is a vertical axis or local surface normal.

The above analysis applies to the scattering of signals from surface components with spatial scales of several wavelengths greater than the incident carrier wavelength (i.e. the GPS L1 wavelength is ~19cm). Alternatively, a contribution to scattering from surface components with spatial scales smaller than several radio wavelengths can be calculated separately using the perturbation theory. Additionally, serious limitations occur for scattering at low grazing angles and from very rough surfaces. In this case, more sophisticated scattering models that take into account multiple scattering and diffraction effects due to sharp edges are required. On the other hand, when surfaces are very even and flat, such as lakes and seas under low wind conditions, or first-year, young ice, the coherent component rises in the scattered GNSS signal. Writing an expression for the received coherent component is a rather simple task.

In the Kirchhoff approximation, the function *g* describes propagation and scattering processes:

$$g(\vec{\rho},t)=-\Re(\vec{\rho})q^2\exp\left[ik\left(R_0(t)+R(t)\right)\right]/4\pi iR_0Rq_z \tag{4.5}$$

where $\Re$ is the Fresnel reflection coefficient; $\vec{q}=k(\vec{n}-\vec{m})$ is the so-called scattering vector, where $k=2\pi/\lambda$ is a radio wave number; $\vec{m}$ is the unit vector of the incident wave; and, $\vec{n}$ is the unit vector of the scattered wave. Upon substituting (4.5) into (4.4), and then into (4.3), and assuming that integration over the accumulation time T_a is equivalent to averaging over a statistical ensemble of surface elevations

$$\left\langle\left|Y(\tau,f)\right|^2\right\rangle=\frac{1}{T_a}\int_0^{T_a}\left|Y(t_0,\tau,f)\right|^2dt_0 \tag{4.6}$$

after making some additional assumptions, we arrive at the bistatic radar equation for the delay-Doppler map [Zavorotny and Voronovich, 2000]

$$\left\langle \left|Y_s(t_0,\tau,f)\right|^2 \right\rangle = T_i^2 \frac{P_T G_T \lambda^2 G_R}{(4\pi)^3} \iint F(\vec{\rho})\Lambda^2(\tau,\vec{\rho})\left|S(f,\vec{\rho})\right|^2 R_0^{-2} R^{-2} \sigma_0(\vec{\rho}) d^2\rho. \quad (4.7)$$

where P_T is the transmitter power; G_T is the transmit antenna gain; G_R is the receive antenna gain; $F(\vec{\rho})$ is the normalized directivity (beam) pattern for the receive antenna; $\Lambda^2(\tau,\vec{\rho})$ is the annulus function due to the cross-correlation with the replica; $\left|S(f,\vec{\rho})\right|^2$ is the Doppler zone function due to the relative motions of both the transmitter and receiver with respect to the scattering surface; R_0, R are distances from a point $\vec{\rho}$ on the surface to the transmitter and receiver, respectively; $\sigma_0(\vec{\rho})$ is a bistatic radar cross section (BRCS) of the rough surface, and generally it is a function of two angles, the incidence angle and the scattering angle. Here, in (4.7) it is written as a function of surface coordinates. The scattered signal comes from the area formed by intersection of the equi-range zones, annular (function $\Lambda^2(\tau,\vec{\rho})$) and equi-Doppler, hyperbolic zones (function $\left|S(f,\vec{\rho})\right|^2$). The width of the equi-range zone depends on the code length (different for C/A code and P code) and on all geometric parameters of the problem. The width of the Doppler zone depends on the receiver velocity and it is the inverse of the coherent integration time, $f_{Dop} = 2/T_i$.

The product of correlation function $\Lambda(\tau)$ and the Doppler zone function constitutes a Woodward Ambiguity Function (WAF) originally introduced in radar technique. The WAF that enters (4.7) is similar to the WAF used in the unfocused SAR technique [Elachi, 1988]. For fixed positions of the transmitter and the receiver both WAF and BRCS are functions of reference surface S coordinates. Looking at (4.7) it is straightforward to conclude that the delay-Doppler map emerges as a convolution of the WAF with BRCS function σ_0. The WAF is close to unity within an area formed by the annulus zone and the Doppler zone, and tends to zero outside this area. The geometry of these zones for two different elevation angles for a typical spacecraft receiver are shown in Figure 10a and b.

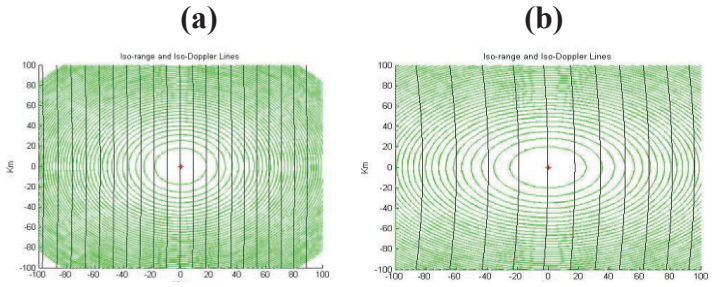

Figure 10. Geometries for two different elevation angles for a typical spacecraft receiver

4.2.2 The Bistatic Radar Cross Section – Geometric Optics Approximation

The effect of surface roughness is described by σ_0, the normalized bistatic radar cross section

In the geometric-optics limit of the Kirchhoff approximation the BRCS function σ_0 is represented by the following expression [Bass and Fuks, 1979, Barrick, 1968]:

$$\sigma_0 = \pi |\Re|^2 \left(q / q_z\right)^4 P\left(-q_\perp / q_z\right) \tag{4.8}$$

Though this value is a function of the scattering vector, $\vec{q}$, for fixed positions of the transmitter and the receiver above a surface, this vector can be regarded as a function of the coordinate $\vec{\rho}$ in the mean surface plane. The value of σ_0 depends on a complex Fresnel coefficient $\Re$ which in turn depends on a signal polarization state, a complex dielectric constant of the reflecting medium, ε, and the local incidence angle. In the case of the GNSS the polarization state of the reflected signal is a left-hand circular polarization (LHCP). In this case, the Fresnel reflection coefficient $\Re$ for sea water is [Zavorotny and Voronovich, 2000]:

$$\Re = \frac{1}{2}\left[\frac{\varepsilon\cos\theta - \sqrt{\varepsilon - \sin^2\theta}}{\varepsilon\cos\theta + \sqrt{\varepsilon - \sin^2\theta}} - \frac{\cos\theta - \sqrt{\varepsilon - \sin^2\theta}}{\cos\theta + \sqrt{\varepsilon - \sin^2\theta}}\right] \tag{4.9}$$

where ε is the complex dielectric permittivity of sea water, and θ is the local incidence angle.

According to Klein and Swift model [Kleain and Swift, 1977]:

at S = 35 ppt and T = 10 deg C ε = 74.62+i51.92 for L1 = 1.57542 GHz; ε = 75.02+i62.39 for L2 = 1.22760 GHz; at S = 30; T = 10 deg C ε = 76.16+i55.30 for L1; ε = 75.02+i62.39: for L2.

Factor $P(\vec{s})$ in (4.8) is the probability density function (PDF) of large-scale "smoothed" surface slopes $\vec{s} = \nabla_\perp \zeta(\vec{\rho})$. Usually, the most probable orientation of surface slopes is parallel to the mean plane, z = 0. Then, the PDF has a maximum at s = 0, and the bistatic cross-section σ_0 has a maximum at $\vec{q}_\perp = 0$, i.e., at the nominal specular direction with respect to the mean surface. Note that the width of σ_0 in terms of ρ describes a glistening zone produced by quasi-specular points on the surface.

Some GNSS reflection receivers have the capability to sample the waveform only with respect to time delay, τ, while the frequency offset f is fixed and intended to compensate the Doppler shift associated with the nominal specular point on the Earth's surface. In this case, we deal with 1-D delay waveforms, as shown in Figure 11 (a)-(d). The leading edge of such waveforms up to the peak value is produced by the central elliptic annulus zone (filtered by the S function) when it expands from zero to its maximal value. The 1-D waveform forms a decreasing trailing edge after the peak because of the WAF behavior over time lags, and/or of the BRCS recession along radial directions according to the distribution of surface slopes. Because of the latter reason, the specific shape of the leading edge and an exact position of the correlation power peak is a function of surface roughness. For rougher surfaces, the leading edge is more stretched and the peak is more shifted toward later time lags.

Equation (4.7) deals with values obtained by averaging over a limited number of independent samples. Such values themselves contain residual noise, which might affect our ability to accurately measure the average waveform. The issue of noise in waveforms and their impact on the accuracy of remote sensing of ocean wind is addressed in Section 4.4. Equation (4.7) relies on the condition that $T_i < \tau_{cor}$. The coherence time can be estimated as $\tau_{cor} = \rho_{coh} / v_r$, where ρ_{coh} is the coherence length of the scattered field at the reception point, and v_r is the velocity of the receiver. According to Van-Cittert-Zernike theorem, ρ_{coh} in the far zone increases linearly with the distance from the instantaneous footprint patch on a scattering surface. The size of the footprint patch, or in our case, an annulus zone, depends on the current time delay between the replica and the reflected signal. Therefore, a computation of the coherence time becomes a non-trivial problem which was addressed in [Zuffada and Zavorotny, 2001, You et al., 2004, Soulat, 2004].

The strength of the bistatically-scattered signal from the ocean surface is mostly affected by the surface roughness since variations in salinity of the ocean is rather small. It is believed that for linear surface gravity waves the slope PDF $P(\vec{s})$ can be approximated by the anisotropic bivariate Gaussian distribution [Zavorotny and Voronovich, 2000, Elfouhaily et al, 2002, Soulat, 2004]:

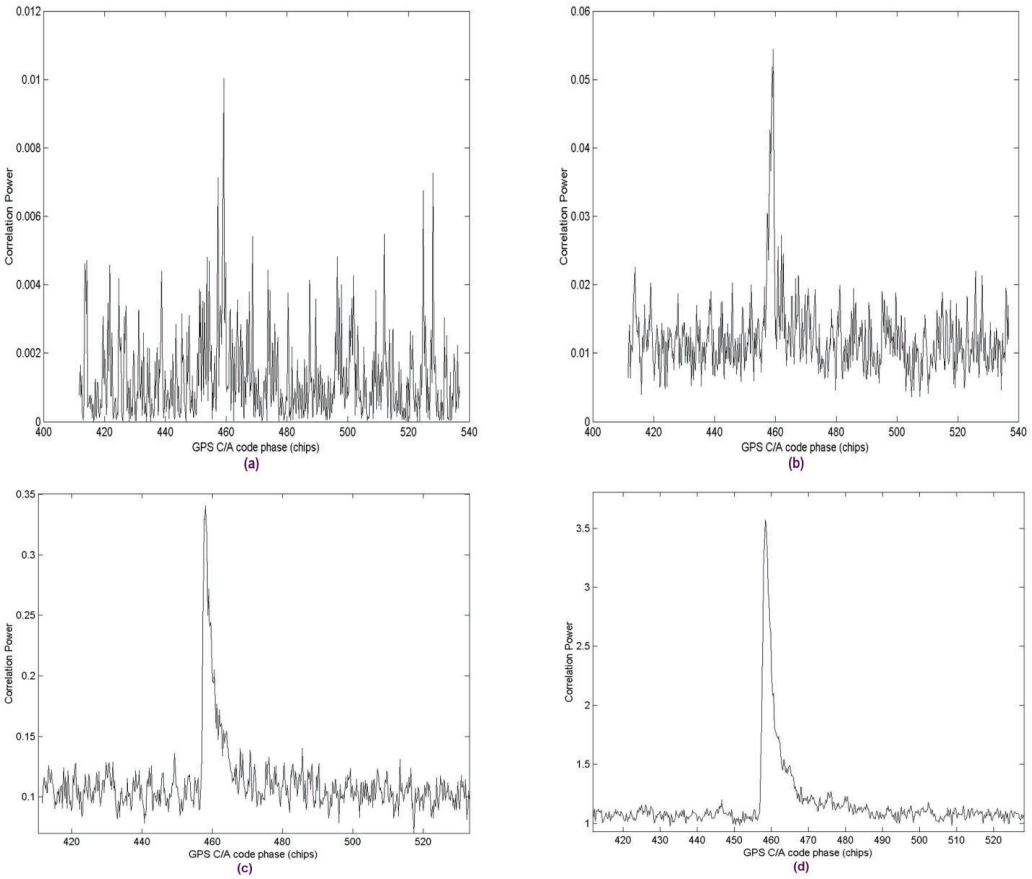

Figure 11. Examples of 1-D delay waveforms [from Gleason, 2006]

$$P(\vec{s}) = \frac{1}{2\pi\sqrt{\det(M)}} \exp\left[-\frac{1}{2} \begin{pmatrix} s_x \\ s_y \end{pmatrix} M^{-1} \begin{pmatrix} s_x \\ s_y \end{pmatrix} \right] \tag{4.10}$$

where matrix M is

$$M = \begin{pmatrix} \cos\varphi_0 & -\sin\varphi_0 \\ \sin\varphi_0 & \cos\varphi_0 \end{pmatrix} \cdot \begin{pmatrix} \sigma_u^2 & 0 \\ 0 & \sigma_c^2 \end{pmatrix} \cdot \begin{pmatrix} \cos\varphi_0 & \sin\varphi_0 \\ -\sin\varphi_0 & \cos\varphi_0 \end{pmatrix} \tag{4.11}$$

where φ_0 is the angle between the up-down wind direction and x axis, which is chosen here to lie within the incidence plane; σ_u^2 is an upwind mean-square slope (upwind mss); σ_c^2 is a cross-wind mean-square slope (cross-wind mss). $\sigma_{u,c}^2$ are wind-dependent and can be derived from a surface elevation spectrum $\Psi(\vec{\kappa})$ by integration over wave numbers κ smaller than a scale-dividing wave number κ_*. Sometimes, matrix M is called a directional mean-square slope in contrast to total mss which is defined as $2\sigma_u\sigma_c$.

When wind is directed along one of two axes (4.10) can be re-written in more common fashion:

$$P(\vec{s}) = \frac{1}{2\pi\sqrt{mss_x mss_y (1-b_{x,y}^2)}} \exp\left[-\frac{1}{2(1-b_{x,y}^2)} \left(\frac{s_x^2}{mss_x} - 2b_{x,y} \frac{s_x s_y}{\sqrt{mss_x mss_y}} + \frac{s_y^2}{mss_y} \right) \right] \tag{4.12}$$

where mss_x and mss_y are mean-square slopes of the sea surface for two orthogonal components; $b_{x,y}$ is the correlation coefficient between two slope components:

$$mss_{x,y} = \left\langle s_{x,y}^2 \right\rangle = \iint\limits_{\kappa<\kappa_*} \kappa_{x,y}^2 \Psi(\vec{\kappa}) d^2\kappa \tag{4.13}$$

$$b_{x,y} = \left\langle s_x s_y \right\rangle / \sqrt{mss_x mss_y} \tag{4.14}$$

$$\left\langle s_x s_y \right\rangle = \iint\limits_{\kappa<\kappa_*} \kappa_x \kappa_y \Psi(\vec{\kappa}) d^2\kappa \tag{4.15}$$

One advantage of a Gaussian distribution is that the variance of slopes in (4.13) can be derived solely from a wave spectrum $\Psi(\vec{\kappa})$, of full surface elevations by integrating it over wave numbers, κ, which are smaller than a dividing parameter, κ_*.

There are some indications that the actual PDF of slopes does not exactly follow a Gaussian shape at their tails [Cardellach and Rius, 2008]. In terms of the glistening zone, it implies that this departure affects a periphery of the zone. This would translate into some discrepancy for the value of the waveform, at relatively large time delays, τ, and large frequency offsets, f. An ability to

discern the difference caused by the departure from the Gaussian PDF of slopes depends on residual noise of measurements for the peripheral area of the DDM.

One of the most popular models for the spectrum $\Psi(\vec{\kappa})$ is the model proposed by [Elfouhaily et al., 1997]. The integrand in (4.13) is called a slope spectral density. An example of Elfouhaily et al. slope spectrum taken along the wind direction is shown in Figure 12.

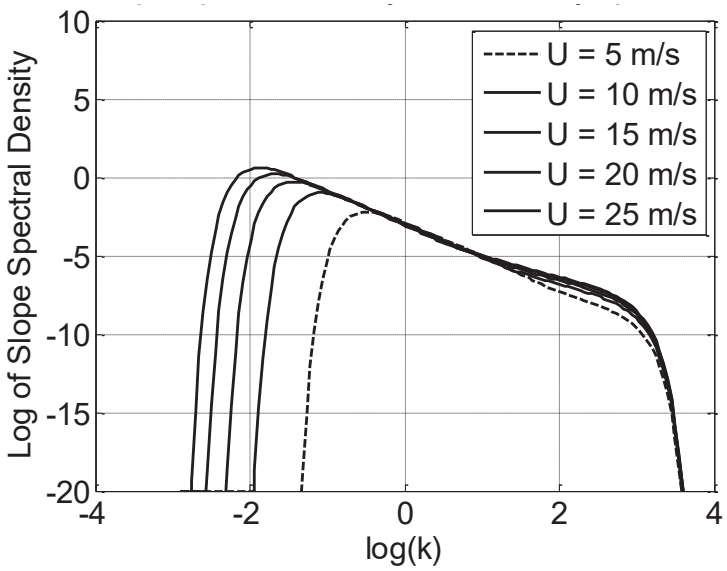

Figure 12. Example of Elfoihaily et al., slope spectrum

This model describes wind-driven waves in deep water under diverse wave age (often called 'fetch') conditions and agrees with the *in situ* observations of the first sun-glint derived wave slope measurements of [Cox and Munk, 1954], performed several decades ago. According to the Elfouhaily et al. model, an elevation spectrum of well-developed wind-driven sea surface can be represented as a product of the radial, or omnidirectional, part of the spectrum, and the azimuthal part of the spectrum. The azimuthal part of the spectrum reproduces two main features of the directional spectrum: its anisotropy, or directionality, and the wavenumber dependence of the angular spectral width. The azimuthal part of the spectrum is a two-sided function; it does not distinguish between up- and down-wind directions. There are other situations when wind direction does not coincide with the maximum of the spectrum, e.g., when gravity waves undergo refraction on currents or on bathymetry, or waves generated by a local wind are superimposed with a swell, or waves generated under the hurricane conditions. Such complicated scenarios are not described by Elfouhaily et al. spectrum.

As it was pointed out above, the mean-square slopes that determine the BRCS through the PDF of slopes are not full wave slopes. Even though, the sea surface contains wave harmonic components both larger and shorter than the L-band electromagnetic waves the short waves can be disregarded in a process of forward quasi-specular reflection under the geometric optics approximation adopted in (4.8). Therefore, the full surface spectrum should be cut off at high end of wave numbers. There

are various choices of cutoff wave number κ_*. For example, there exists a "three-lambda" heuristic criterion for κ_* proposed by [Brown, 1978] based on fitting modeled curves for microwave back scattering cross sections with cross sections obtained in experiments with satellite radar altimeters. The same criterion was initially applied for use of the Kirchhoff approximation for the two-scale calculations of the bistatic cross sections [Zavorotny and Voronovich, 2000]. Later on, a reasonable $\kappa_* = \kappa\cos\theta/3$ on the incidence angle θ was assumed in [Garrison et al., 2002]. In [Thompson et al., 2005], an expression for κ_* is obtained which contains also a dependence on wind speed, $\kappa_* = k\cos\theta\left(1+U_{10}/20\right)/7.5$. It was obtained by fitting modeled curves for GNSS bistatic scattering cross sections with cross sections obtained in that particular aircraft experiment.

An alternative approach is to obtain an empirical model for mss of slopes against wind speed by performing multiple measurements of GNSS waveforms under controlled wind conditions. The best fit between measured waveforms and modeled ones using (4.8) for various mss values will give the sought dependence mss vs wind speed. This approach was adopted in [Katzberg et al., 2006]. The empirical model from [Katzberg et al., 2006] gives the following expression:

$$\begin{aligned} mss_{\parallel} &= 0.45\cdot(0.00+0.00316)\,f(U) \\ mss_{\perp} &= 0.45\cdot(0.03+0.00192)\,f(U) \end{aligned} \tag{4.16}$$

where

$$f(U)=\begin{cases} U & 0.00 < U < 3.49 \\ 6\cdot\ln(U)-4.0 & 3.49 < U < 46 \\ 0.411\cdot U & 46.0 > U \end{cases} \tag{4.17}$$

Wind speed U here is m/s and measured at 10-m height. The extension of $f(U)$ beyond $U = 46$ m/s proposed in [Katzberg et al., 2006] was rather arbitrary because GPS reflection data were not available for such high winds.

Below in Figure 13 we present comparisons between mss calculated using all three approaches: two based on the Elfouhaily et al spectrum with two different cutoff numbers κ_* from [Garrison et al., 2002] and [Thompson et al., 2005], and the empirical one from [Katzberg et al., 2006].

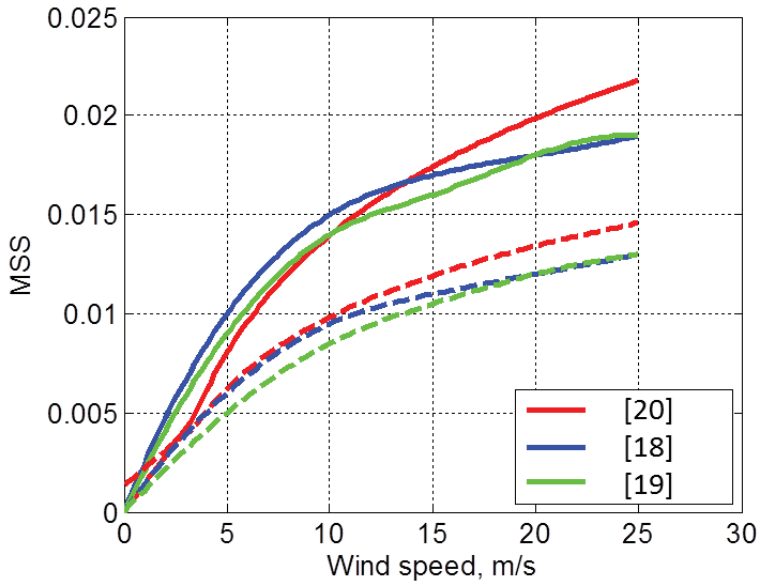

Figure 13. comparison between mss calculated using the approaches in [Garrison et al., 2002], [Thompson et al., 2005], and the empirical one from [Katzberg et al., 2006]. They are respectively indicated as [18], [19] and [20].

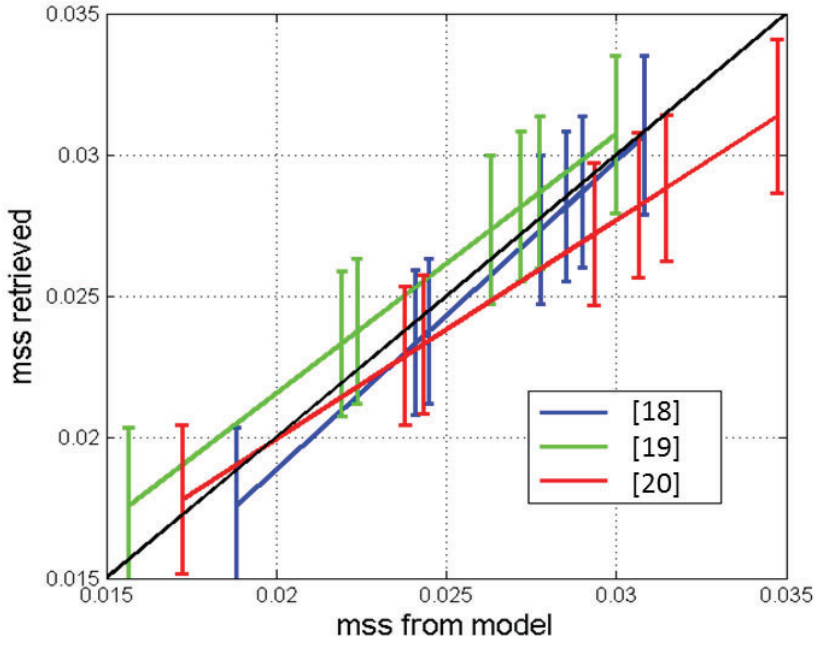

Figure 14. comparison between modeled mss and mss retrieved from DDM measurements during aircraft experiments, using the approaches in [Garrison et al., 2002], [Thompson et al., 2005], and the empirical one from [Katzberg et al., 2006]. They are respectively indicated as [18], [19] and [20].

Figure 13 demonstrates a comparison between three GO models for mss in the up-down wind direction (solid curves) and in the cross-wind direction (dashed curves) for the range of winds between 0 and 25 m/s. Some disagreement between them is seen but overall it is not significant. Figure 14 shows a comparison between three modeled mss and mss retrieved from DDM measurements during aircraft experiments [Rodriguez-Alvarez et al, 2013, Valencia et al., 2014].

In order to make a choice between these three models we performed calculations of σ_0 using a more accurate (than the GO) approximation, a so called small slope approximation which does not require use of spectral dividing parameter κ_*. This material is presented below.

4.2.2 Integrated Scattering Model: The Bistatic Radar Cross Section in Small Slope Approximation

The small slope approximation (SSA) was developed earlier in [Voronovich, 1994, Voronovich, 1999] and was used successfully for solving various scattering and radiometric problems (see, e.g., [Voronovich and Zavorotny, 2001, Elfouhaily and Guerin, 2004, Johnson, 2005, Johnson and Elfouhaily, 2007, Soriano and Guerin, 2008, Arnold-Bos, 2007, 2007b , Guerin et al., 2010, Voronovich and Zavorotny, 2014]). The geometry of the scattering problem is shown in Figure 15. Three typical scenarios are depicted, although the model considered below allows any possible combination of incident, scattering, and azimuthal angles and arbitrary polarization states. There are known two approximations of the SSA, the SSA of the 1st order and the SSA of the 2nd order. The latter is more accurate than the former, and is required for solving backscattering problems with shorter EM wavelengths such as the X- and K-band. Practice shows that for the L-band and for the forward scattering regime it is suffice to use the SSA of the 1st order, or SSA1.
Note that the expression for the scattering amplitude in SSA1 coincides with the expression for scattering amplitude in the Kirchhoff approximation (KA) to the accuracy of the pre-integral factor. The major difference, however, is that KA gives a correct answer only for the roughness

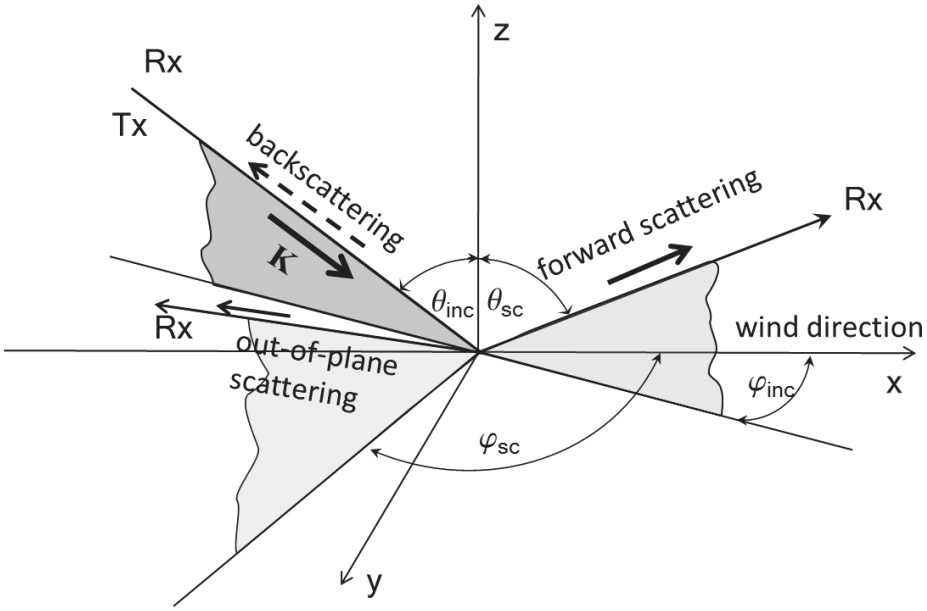

Figure 15. Geometry of the scattering problem for SSA.

$h(\vec{r})$ which is smooth on the wavelength scale; in this case, the corresponding integral can be evaluated by the stationary phase method, thus leading to the geometric optics (GO) approximation. The difference between the GO and KA approximations most likely exceeds the accuracy of the KA itself. In contrast to the KA, SSA1 allows $h(\vec{r})$ to contain a component with a horizontal scale comparable (or even less) than the wavelength, provided that the slope remains small. In this case the corresponding integral also describes the Bragg scattering process and cannot be calculated by the stationary phase method.

For the case of a large Rayleigh parameter, when the contribution from the average-field-related terms can be neglected, the SSA1 gives the following expression for the bistatic radar cross section [Johnson, 2005]:

$$\sigma_{\alpha\beta,\alpha'\beta'}(\vec{k},\vec{k}_0)=\frac{4q_k^2q_0^2}{\pi(q_k+q_0)^2}B_{\alpha\beta}(\vec{k},\vec{k}_0)\overline{B}^*_{\alpha'\beta'}(\vec{k},\vec{k}_0)\int_{r<r_{\max}}\exp\left[-i(\vec{k}-\vec{k}_0)\vec{r}-(q_k+q_0)^2(C(0)-C(\vec{r}))\right]d\vec{r} \qquad (4.18)$$

where $r_{\max}$ determines the area significant for integration. $\alpha,\beta,=1,2$ and $\alpha',\beta'=1,2$ are linear polarization indices for incident and scattering waves, respectively. Function $B_{\alpha,\beta}(\vec{k},\vec{k}_0)$ in (4.18) is a 2x2 matrix representing polarizations (1 stands for vertical and 2 stands for horizontal linear polarization), respectively; they depend on the scattering geometry and dielectric constant of the medium. Expressions for them can be found in [Voronovich and Zavorotny, 2001]. Expressions

for the LHCP bistatic scattering cross section can be expressed through corresponding cross sections for linear polarization as follows [Fung et al., 2001, Zuffada et al., 2004]:

$$\sigma_{RL} = \frac{1}{4}\left\{\sigma_{11,11} + \sigma_{22,22} + \sigma_{12,12} + \sigma_{21,21} + 2\left[-\mathrm{Re}\,\sigma_{11,22} + \mathrm{Re}\,\sigma_{12,21} - \mathrm{Im}\left(\sigma_{11,12} + \sigma_{11,21} + \sigma_{12,22} + \sigma_{21,22}\right)\right]\right\} \quad (4.19)$$

We performed calculations of BRCS using (4.18) and (4.19) and compared it with corresponding BRCS based on the above described GO models for a typical CYGNSS setting and for a range of incidence angles and winds. These results are discussed below.

4.2.3 4.2.4. BRCS as a function of the incidence angle and wind speed: comparisons between three models

Here, we present comparisons between the SSA results and results obtained with the GO model, one using an MSS based on the Elfouhaily spectrum and the cutoff frequency from [Garrison et al., 2002], and another one using the empirical MSS model from [Katzberg et al., 2006]. For short we will call these two GO models "VZ model" and "SK model," respectively. First, we present plots showing the corresponding LHCP BRCS σ_0 in a forward, specular direction as a function of the zenith scattering angle (which in this case equals to the incidence angle) for a range of wind speeds from 4 to 30 m/s. The results for the VZ, KS and SSA models are shown in Figure 16a, 16b and 17, respectively. Each plot has twelve curves. The top curve on each plot corresponds to wind speed U = 4 m/s. The rest of the curves correspond to 5, 6, 7, 8, 9, 10, 12, 15, 20, 25, 30 m/s consecutively.

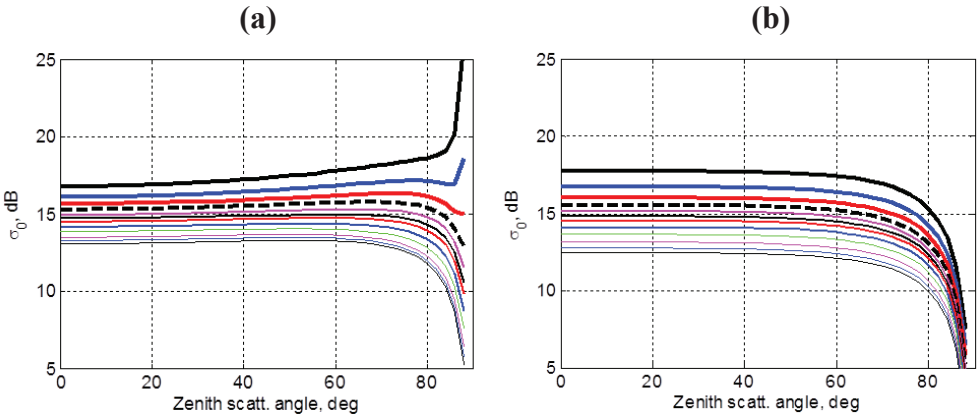

Figure 16. LHCP BRCS σ_0 in a forward, specular direction as a function of the zenith scattering angle for a range of wind speeds from 4 to 30 m/s, for the VZ (a) and KS (b) model.

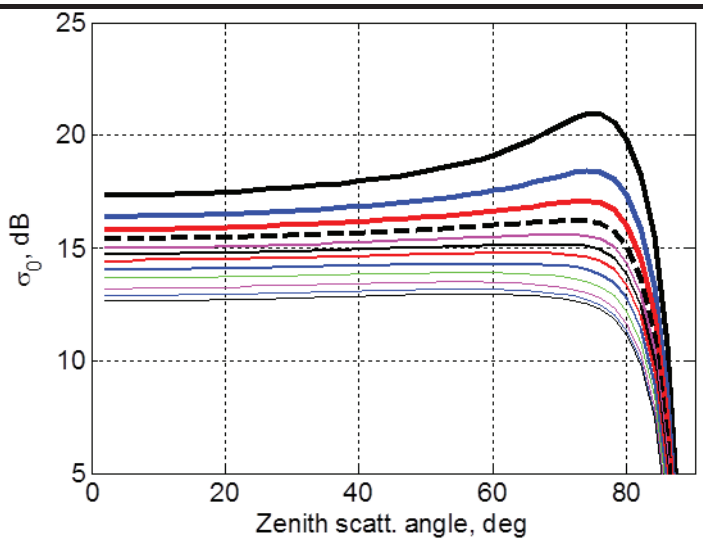

Figure 17. LHCP BRCS σ_0 in a forward, specular direction as a function of the zenith scattering angle for a range of wind speeds from 4 to 30 m/s, for the SSA model.

This dependence on wind speed reflects that fact that increased wind produces a stronger surface roughness which, in its turn, decreases scattering in a specular direction. One can see that σ_0 behaves differently for every of these models at scattering angles larger than 60°-70°. Remember, that any of those models are valid at large scattering angles so we can disregard this discrepancy. For the case of CYGNSS antenna pointing angle of about 30° this discrepancy is not relevant. Note only that the SK model was built on GPS reflection data obtained for low incidence/scattering angles, < 45°, therefore, it might not reflect the actual behavior of the scattering at larger angles. At the same time, all three models demonstrate a quite similar behavior over wind speeds for angles below 45°.

To investigate this behavior in more detail, we will plot the wind dependence of σ_0 for a set of small scattering angles and for a fixed moderate incidence angle below 45°. We would like to check how predictions for σ_0 from all three models correspond to each other for scattering originated from various point on the surface area limited to some number of delay zones that contributes to the Delay-Doppler Map. The corresponding scattering geometry is shown in Figure 18.

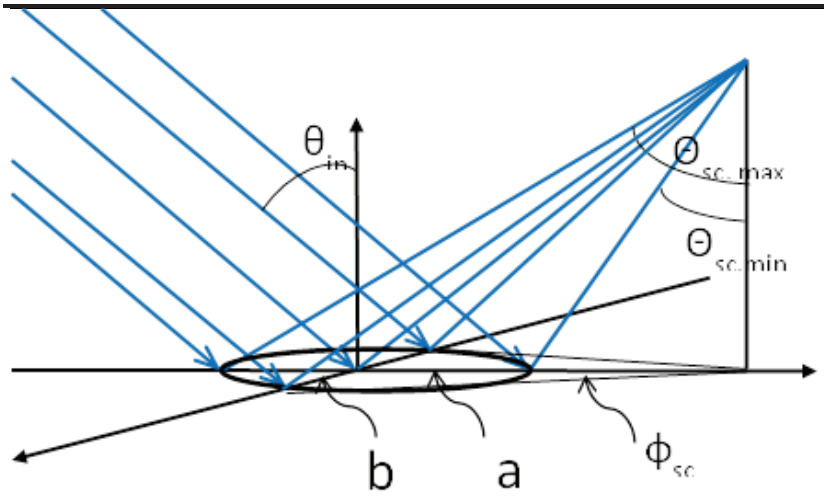

Figure 18. Scattering geometry for a fixed moderate incidence angle below 45°.

Notations in Figure 18 are as follows. a_n and b_n are major semi-axes of the elliptic delay zones where index n correspond to a . They can be expressed through the chip length l, receiver altitude H, and incidence angle θ_{in}, as: $a_n = b_n / \cos\theta_{in}$, $b_n = \left(2nlH / \cos\theta_{in}\right)^{1/2}$.

Figure 19 shows how angles $\theta_{sc,\min}, \theta_{sc,\max}$ and ϕ_{sc} from Figure 18 can be related to the corresponding points on the delay-zone ellipse for a range of delay-zone index (from 0 to 10). The curves are plotted for $\theta_{in} = 30°$, $H = 600$ km, and $l = 300$ m (C/A code).

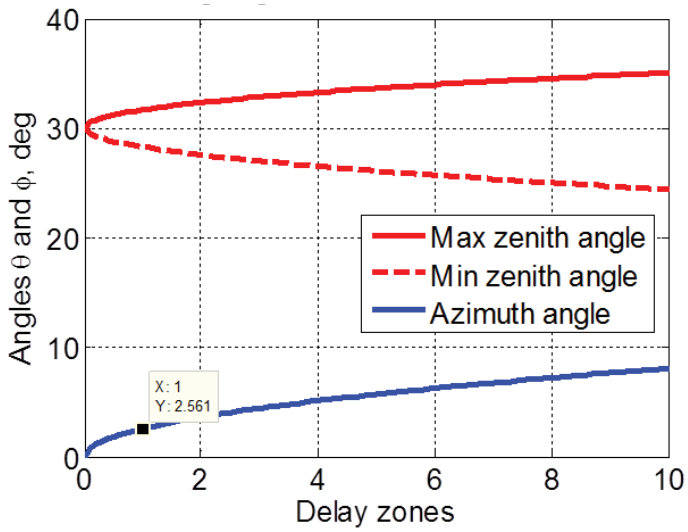

Figure 19. relationship between angles $\theta_{sc,\min}, \theta_{sc,\max}$ and ϕ_{sc} from Figure 18 and corresponding points on the delay-zone ellipse for a range of delay-zone index from 0 to 10.

The data tip in this figure shows that for the first delay zone the maximum azimuth scattering angle is equal to 2.56°.

Below in Figure 20(a-d) we present plots of σ_0 obtained with the three models for $\theta_{in} = 30°$, $H =$ 600 km, and for four directions of scattering vector described by following combinations of zenith and azimuth scattering angles: (a) $\theta_{sc} = 30^\circ, \phi_{sc} = 0^\circ$; (b) $\theta_{sc} = 30^\circ, \phi_{sc} = 2.56^\circ$; (c) $\theta_{sc} = 28^\circ, \phi_{sc} = 0^\circ$; and (d) $\theta_{sc} = 32^\circ, \phi_{sc} = 0^\circ$. This set of angles gives an angular extent for the first delay zone (n = 1). Case (a) describes a nominal specular direction originated from the center of the delay zone. Case (b) describes a scattering direction originated from both left and right most distant (in a cross direction) points of the first delay-zone ellipse. This is an example of out-of-plane scattering. Here, by "plane" we mean a specular plane which by definition passes through the specular point on the surface and both transmitter and the receiver points. Case (c) describes a scattering direction originated from the closest point on the first delay-zone ellipse. Correspondingly, case (d) is for the farthest point on the first delay-zone ellipse.

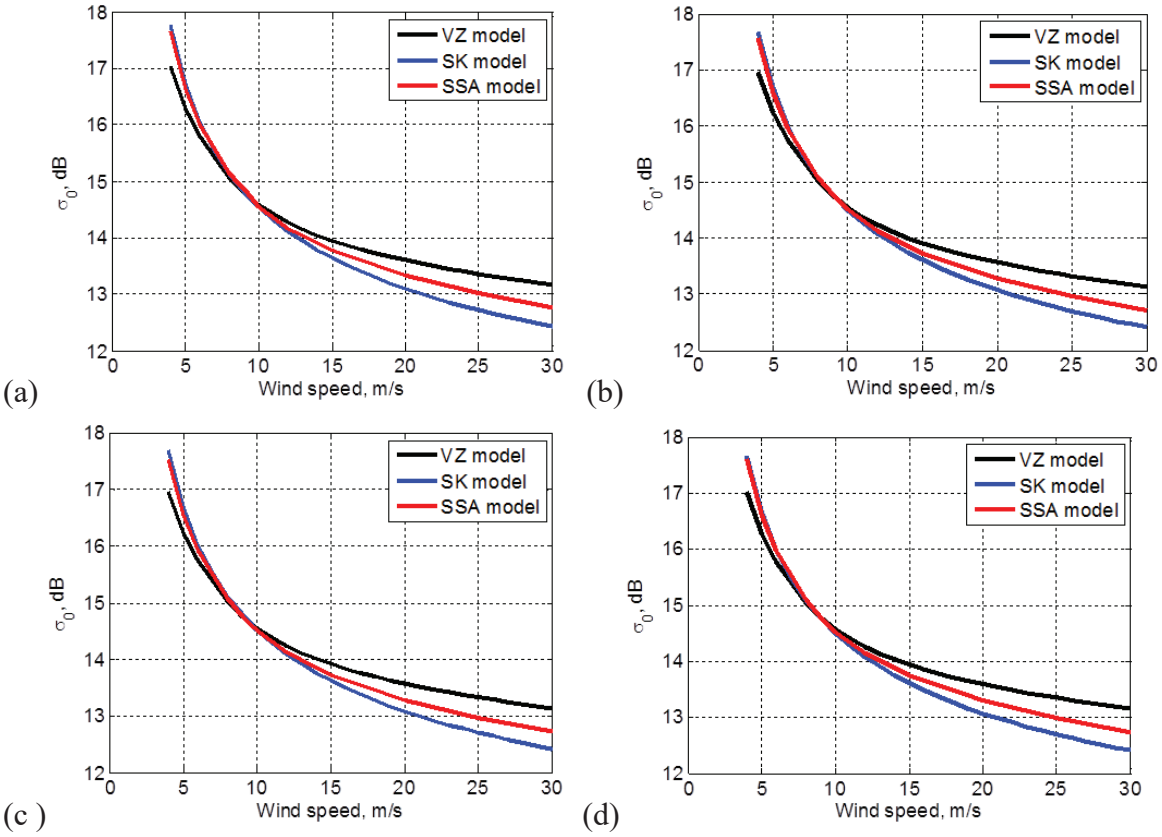

Figure 20. plots of σ_0 obtained with the three models for θ_{in} = 30°, *H* = 600 km, and for four directions of scattering vector described by following combinations of zenith and azimuth scattering angles: (a) $\theta_{sc} = 30^\circ, \phi_{sc} = 0^\circ$; (b) $\theta_{sc} = 30^\circ, \phi_{sc} = 2.56^\circ$; (c) $\theta_{sc} = 28^\circ, \phi_{sc} = 0^\circ$; and (d) $\theta_{sc} = 32^\circ, \phi_{sc} = 0^\circ$.

One can see that curves in Figure 20 practically repeat themselves at each panel. This means that while LHCP BRCS σ_0 is changing with the wind speed it does not appreciably change over the angles within the first delay zone. The discrepancy between curves for all three models are within 0.5 dB for wind speed below 15-17 m/s which is rather negligible given such adverse factors as speckle noise and natural wind speed variability that accompany real measurements. The discrepancy between the SSA curve and the SK curve (which we use in the end-to-end DDM simulator) is less than 0.5 dB for the entire range of wind speeds used for this simulation, i.e. below 30 m/s. More important, the steepness of these two curves is similar, which would result in a similar accuracy of the wind retrievals from the real GNSS-R data.

Below in Figure 21 (a-d) we present similar plots of σ_0 obtained with the three models for the same basic geometry but it gives an angular extent for the tenth delay zone (n = 10). The tenth delay zone covers the surface area which contributes to the DDM that will be routinely used during CYGNSS mission. Here, therefore: (a) $\theta_{sc} = 30^\circ, \phi_{sc} = 0^\circ$ (this plot repeats plot (a) from the previous figure; it is given for comparison purposes); (b) $\theta_{sc} = 30^\circ, \phi_{sc} = 8^\circ$; (c) $\theta_{sc} = 25^\circ, \phi_{sc} = 0^\circ$; and (d) $\theta_{sc} = 35^\circ, \phi_{sc} = 0^\circ$.

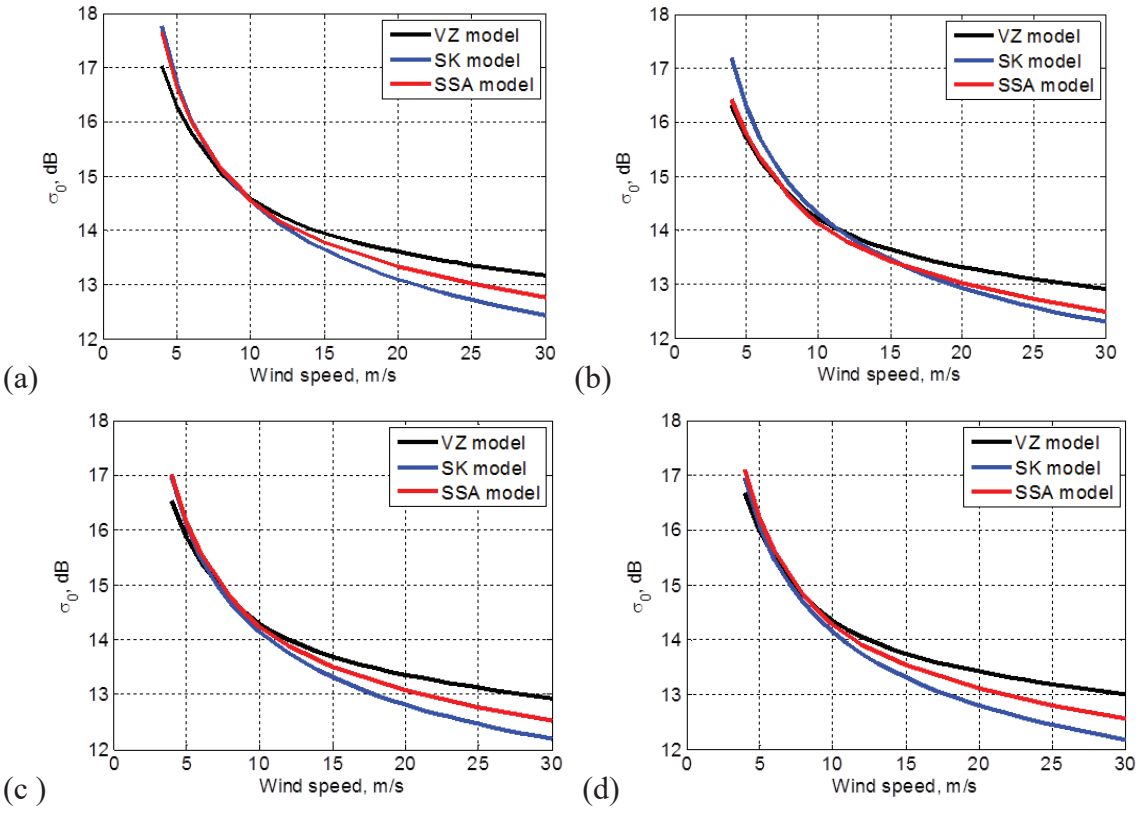

Figure 21. plots of σ_0 obtained with the three models for the same basic geometry and an angular extent for the tenth delay zone (*n* = 10). (a) $\theta_{sc} = 30^\circ, \phi_{sc} = 0^\circ$; (b) $\theta_{sc} = 30^\circ, \phi_{sc} = 8^\circ$; (c) $\theta_{sc} = 25^\circ, \phi_{sc} = 0^\circ$; and (d) $\theta_{sc} = 35^\circ, \phi_{sc} = 0^\circ$.

As one can see there is no significant difference between this set of plots and the one from the previous figure. Therefore, same statement about σ_0 behavior can be presented here for the case of the tenth delay zone.

4.3 Conclusions on Rough Surface Scattering

We described how the bistatic radar cross section σ_0 of the ocean, wind-driven rough surface emerges within the framework of the bistatic radar equation which governs the average GNSS-R signal in the delay-Doppler domain. We presented two alternative approaches to simulate σ_0. One of them is based on the geometric optics (GO) limit of the Kirchhoff approximation, and another one is the Voronovich small slope approximation (SSA) of the 1st order. The latter approach is superior to the former one because it combines two scattering mechanisms: quasi-specular reflections at steep incidence and the Bragg resonant scattering at the shallower incidence, whereas the GO approximation relies only on the first mechanism for the whole range of incidence angles. Both of these approaches require knowledge of the ocean wave spectrum, or, as in the case of the GO approach the model of the mean-square-slopes (MSS) will be suffice. To this end, the theoretical model based on Elfouhaily's ocean wave spectrum with two different frequency cutoffs was tested, as well as Dr. Katzberg's empirical MSS model. All these models demonstrate a good agreement for weak and intermediate winds. They depart from each other only for strong winds, and this departure is rather tolerable given such adverse factors as speckle noise and natural wind speed variability that accompany real measurements.

Originally, Katzberg's empirical MSS model has been chosen for the end-to-end simulator of the Delay-Doppler Map. This choice was made because this model is based on a collection of aircraft GPS reflection measurements obtained for a large variety of wind speeds including for hurricane conditions. Comparisons between σ_0 modeled with both the GO and the SSA approaches show that for the geometry of CYGNSS orbital observatories and for the range of winds up to 30 m/s the GO approximation with Katzberg's empirical MSS model works very well. The advantage of the GO approximation is its simplicity and high speed of calculations, whereas the SSA approximation is more time consuming. All this makes our choice for the σ_0 computational algorithm even more substantiated.

Previously, some concerns have been expressed (see, e.g., [Thompson et al., 2000]) that the GO approximation might not work well for the GNSS reflectometry because it cannot properly account for out-of-plane scattering. Generally, the GO approximation has its own limitations, especially for calculations of the RHCP σ_0, and particularly for the out-plane configuration. However, as it was demonstrated here, for small deviations from the specular plane, the LHCP σ_0 is quite close to that one predicted by the more accurate SSA approximation.

The more fundamental limitation of all above models lies in the fact that they either have been proven only for global winds below 25-30 m/s (such as for those based on the Elfouhaily spectrum), or their accuracy is not high for strong hurricane winds (such as in the case of Katzberg's MSS

model). For hurricane conditions, a feasible wave-spectral model should include, apart from a local wind speed, also several other parameters such as a distance from the hurricane center, azimuthal angle (a quadrant), hurricane velocity and other hurricane parameters.

Plans are to use an existing WAVEWATCH III wave model [Tolman et al, 1998] developed at the NOAA National Centers for Environmental Prediction (NCEP) which is now widely used for hurricane long-wave predictions (see, e.g., [Fan et al., 2009]). As a first step, it is expected that this model will be able to provide us with the long-wave portion of the sea state spectrum (so called "fresh swell") in the hurricane eye specifically and everywhere in general. More challenging would be a task to extend this model toward much shorter waves up to the cutoff frequency introduce above. Also, plans are to verify the DDM output of such a model with already available radiometric, scatterometric and GNSS-R data obtained in hurricanes. For this, archives of past aircraft GNSS-R overpasses of hurricane eyes can be used in order to assemble time series records of the MSS and to infer surface wind speed in the eye. Other surface wind estimates (e.g. from flight level winds or SFMR) are also available. Raw DDM-grade GNSS-R data from Hurricanes Ike (2008), Rafael (2012) and Sandy (2012) obtained with CU bistatic GNSS bistatic radar can also be used for validation purposes. The work on processing of these data for CYGNSS purposes is currently performed.

4.4 Delay and Doppler Coordinate System

The scattered signal can be thought of as a superposition of components scattered from various points on the sea surface. Each component will have a shift in both the time at which the signal arrives at the receiver (delay shift) and the frequency of the signal (Doppler shift). The diversity in delay is due to different paths followed by each scattered signal, while different frequency shifts are caused by the relative motion between transmitter, scattering point on the surface and receiver. Each point of the GZ is therefore characterized by its own delay and Doppler shift [Clarizia, 2012].

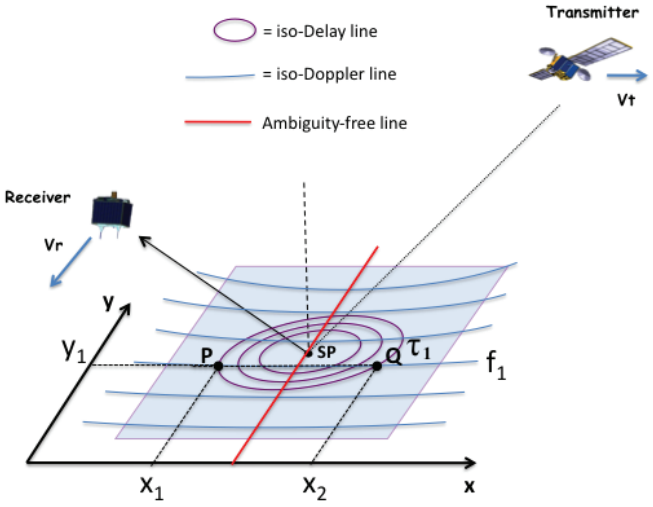

Figure 22. Delay-Doppler coordinates in GNSS-R and their relation to the space coordinate system (from [Clarizia, 2012]).

The pair of delay-Doppler values to which each point in space can be associated represents indeed a new domain in which the GZ can be mapped, and it is known as delay-Doppler domain. Such domain is fundamental for GNSS-R processing since it is the domain in which GNSS-R data are commonly presented and mapped, in the form of the so called delay-Doppler Maps (DDMs). However, different points on the sea surface will correspond to the same pair of delay-Doppler values. Lines corresponding to constant delays (iso-range) and constant Doppler shifts (iso-Doppler) can be identified on the sea surface, and they have respectively an elliptical and parabolic shape. Lines of constant delays, also called iso-range lines, are given by concentric ellipses around the SP, and they correspond to increasing delays for increasing distance from the SP, which is the point at minimum delay. Rigorously speaking, the iso-range lines are the intersections of spheroids (equi-range surfaces) having receiver and transmitter as foci, with the sea surface, which causes the ellipses to be not exactly concentric as their centers move towards the transmitter [Zuffada et al., 2004]. The iso-Doppler lines are parabolic shaped lines cutting through the GZ. They are also asymmetric and characterized by complicated equations, and lines of lower and higher Doppler frequency shifts cannot be predicted, since they strictly depend on the relative velocities among the transmitter, the scattering point and the receiver. From Figure 22, we can notice that a generic point P on the GZ can be described by a delay and Doppler coordinate. Such a correspondence is however not biunivocal, since there is an ambiguity since the intersection between an iso-range and iso-Doppler line is made of two points in space, which will have the same Delay and Doppler frequency, like points P and Q in Figure 22. Despite that, it is interesting to note that there exists a line free of ambiguity, which can be thought as the transverse axis of the hyperbolic iso-Doppler lines, shown in red in Figure 22.

The space-to-DD transformation of coordinates is also what gives the DDM a characteristic horseshoe shape. Such transformation operates on the spatial domain by “folding” the glistening zone along the free ambiguity line, and by “bending” it at the specular point, or the peak power in the DDM. The scattered power at the specular point corresponds therefore to the central point of the horseshoe shape, and the horseshoe branches correspond to the scattered power from the glistening zone, with areas farther from the SP spanning larger delays and Doppler shifts.

One other important aspect of the delay-Doppler coordinate system is its dependence on the geometry, and in particular on the incidence angle, which strongly influences the configuration of the iso-delay and Iso-Doppler lines. Figure 23 shows the change in the iso-delay contours over a footprint of 100 x 100 km^2, for different incidence angles, where the incidence angle is the angle between the transmitter or receiver range and the normal to the surface. The iso-delay ellipses tend to stretch out and become wider for higher incidence angles. Here the transmitter and receiver altitudes have been assumed to be respectively equal to the GPS (~20200 km, and 475 km).

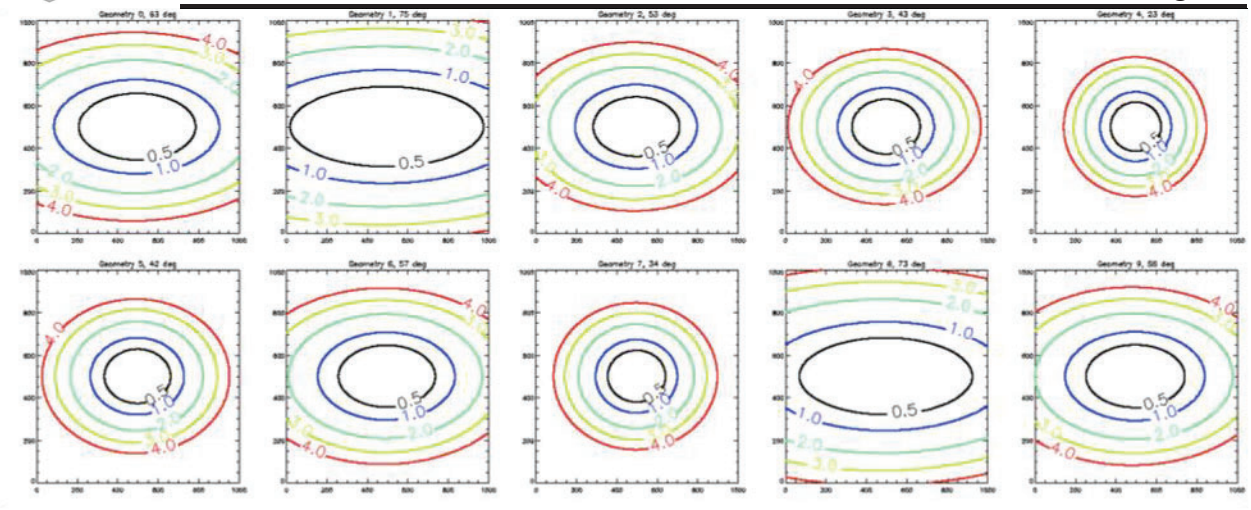

Figure 23. Iso-delay contours over a footprint of 100 x 100 km, for the following incidence angles (top, left to right): 63°, 75°,53°,43°,23°; (bottom, left to right): 42°, 57°, 34°, 73°, 58°.

Figure 24 shows the range of maximum delays (a) and maximum Doppler frequencies (b) within a 50 x 50 km footprint, as a function of incidence angle. In Figure 24(b), a specific velocity vector has been assumed for the GPS and the receiver satellite. In principle, once the whole geometry is known (i.e. transmitter and receiver altitudes, incidence angles and velocity vectors), the range of delays and Dopplers spanned by a footprint of given size can be calculated numerically.

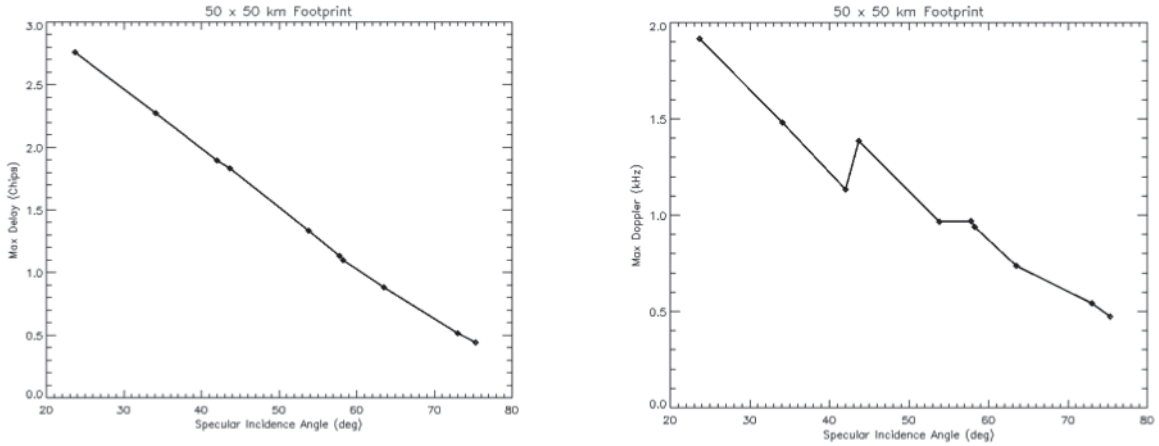

(a) **(b)**

Figure 24. (a) maximum delay as a function of incidence angle, within a 50 x 50 km^2 footprint; (b) maximum Doppler as a function of incidence angle, within the same footprint.

4.5 Mean Power and Signal-to-Noise Ratio for the GPS Reflected Signal

Let us represent the instantaneous complex signal (the voltage) u, which is acquired directly by the receiver from the antenna output, or as a result of some coherent processing, in the form:

$$u(t) = s(t) + n(t), \tag{4.20}$$

where $s(t)$ is the complex amplitude of the scattered signal, and $n(t)$ is the complex amplitude of the additive noise. We assume that $s(t)$ and $n(t)$ are two uncorrelated, stationary random processes, both obey circular Gaussian statistics and have different time scales, and different variances $\sigma_1^2 \equiv \sigma_{\mathrm{Re}\,s}^2 \equiv \sigma_{\mathrm{Im}\,s}^2$ and $\sigma_2^2 \equiv \sigma_{\mathrm{Re}\,n}^2 \equiv \sigma_{\mathrm{Im}\,n}^2$, both with zero means. The Gaussian statistics for $s(t)$ can be justified if the signal at the antenna is formed by contributions from a large number of independent surface scatterers. Here, we exclude from a consideration fluctuations of the signal caused by propagation through ionospheric and tropospheric irregularities. Fluctuations of $s(t)$ generate multiplicative, self-noise, (other names: interference noise, Rayleigh fading, speckle noise), which are proportional to the signal, whereas fluctuations of $n(t)$ produce additive, background noise (i.e., thermal noise or shot noise). In a more complex situation, the additive noise could include extraneous emitted signals. So, in what follows we limit that background noise to thermal noise.

A coherent processing of the scattered GPS signal by the correlator channel of the CYGNSS receiver consists of the convolution (correlation) of voltage $u(t)$ with the replica a of the GPS broadcast signal over a relatively short (milliseconds) coherent integration time T_i:

$$Y(t_0, \tau) = \int_0^{T_i} a(t_0 + t')u(t_0 + t' + \tau)dt'. \tag{4.21}$$

Taking into account (4.20), we obtain from (4.21) that

$$Y(t_0, \tau) = Y_s(t_0, \tau) + Y_n(t_0, \tau), \tag{4.22}$$

where

$$Y_s(t_0, \tau) = \int_0^{T_i} a(t_0 + t')s(t_0 + t' + \tau)dt', \tag{4.23}$$

$$Y_n(t_0, \tau) = \int_0^{T_i} a(t_0 + t')n(t_0 + t' + \tau)dt'. \tag{4.24}$$

Therefore, the quantities in (4.23) and (4.24) are short-integrated (practically, instantaneous) correlation voltages, respectively, for the signal and noise. The next step of the signal processing is obtaining the mean power of the correlator output. It is obtained by an additional averaging of $|Y(t_0, \tau)|^2$ over a long enough observation time, so both thermal and surface-induced fluctuations are substantially averaged out. The result is

$$\left\langle |Y(t_0, \tau)|^2 \right\rangle = \left\langle |Y_s(t_0, \tau)|^2 \right\rangle + \left\langle |Y_n(t_0, \tau)|^2 \right\rangle. \tag{4.25}$$

4.5.1 The Signal Term

The first term in Eq. (4.25) is known in the literature [Zavorotny and Voronovich, 2000] as the GPS radar bistatic equation:

$$\left\langle \left|Y_s(t_0,\tau)\right|^2 \right\rangle = T_i^2 \frac{P_T G_T \lambda^2 G_R}{(4\pi)^3} \times \iint F(\vec{\rho})\Lambda^2(\tau,\vec{\rho})\left|S(f_{dop},\vec{\rho})\right|^2 R_0^{-2} R^{-2} \sigma_0(\vec{\rho}) d^2\rho. \tag{4.26}$$

where P_T is the transmitter power; G_T is the transmit antenna gain; G_R is the receive antenna gain; $F(\vec{\rho})$ is the normalized directivity (beam) pattern for the receive antenna; $\Lambda^2(\tau,\vec{\rho})$ is the annulus function due to the cross-correlation with the replica; $\left|S(f_{dop},\vec{\rho})\right|^2$ is the Doppler zone function due to the relative motions of both the transmitter and receiver with respect to the scattering surface; R_0, R are distances from a point $\vec{\rho}$ on the surface to the transmitter and receiver, respectively; $\sigma_0(\vec{\rho})$ is a bistatic cross section of the rough surface, and generally it is a function of two angles, the incidence angle and the scattering angle. Here, in (4.26) it is written as a function of surface coordinates. The scattered signal comes from the area formed by intersection of the equi-range zones, annular (function $\Lambda^2(\tau,\vec{\rho})$) and equi-Doppler zones (function $\left|S(f_{dop},\vec{\rho})\right|^2$). The width of the annulus depends on the code length (different for C/A code and P code) and on all geometric parameters of the problem. The width of the Doppler zone depends on the receiver velocity and a coherent integration time, T_i.

The bistatic radar cross section used in this model is based on geometric optics approximation (see, e.g., [Barrick, 1968]). With regard to our problem it has the following form [Zavorotny and Voronovich, 2000]

$$\sigma_0(\vec{\rho}) = \frac{\pi\left|\Re\right|^2 q^4}{q_z^4} P\left(-\frac{\vec{q}_\perp}{q_z}\right). \tag{4.27}$$

The cross section is maximal at $\vec{q}_\perp = 0$ because the probability density function (PDF) of slopes $P(\vec{s})$ has a maximum at $\vec{s} = 0$, i.e., for the most probable orientation of slopes, parallel to z = 0.

Here, we use the Gaussian bivariate statistics of anisotropic slopes:

$$P(\vec{s}) = \frac{1}{2\pi\sqrt{mss_x mss_y (1-b_{x,y}^2)}} \exp\left[-\frac{1}{2(1-b_{x,y}^2)}\left(\frac{s_x^2}{mss_x} - 2b_{x,y}\frac{s_x s_y}{mss_x mss_y} + \frac{s_y^2}{mss_y}\right)\right] \tag{4.28}$$

where mss_x and mss_y are mean-square slopes of the sea surface for two orthogonal components; $b_{x,y}$ is the correlation coefficient between two slope components:

$$mss_{x,y} = \left\langle s_{x,y}^2 \right\rangle = \iint\limits_{\kappa<\kappa_*} \kappa_{x,y}^2 W\left(\vec{\kappa}\right) d^2\kappa \tag{4.29}$$

$$b_{x,y} = \left\langle s_x s_y \right\rangle / \sqrt{mss_x mss_y} \tag{4.30}$$

$$\left\langle s_x s_y \right\rangle = \iint\limits_{\kappa<\kappa_*} \kappa_x \kappa_y W\left(\vec{\kappa}\right) d^2\kappa \tag{4.31}$$

Here, $W(\vec{\kappa})$ is the surface elevation spectrum. For calculations we adopt the Elfouhaily spectrum [Elfouhaiyl et al., 1997]. The sea surface contains wave harmonic components both larger and shorter than the L-band electromagnetic waves. The short waves can be disregarded in a process of forward quasi-specular reflection. Because of this, the geometric optics approximation is applicable here but then the full surface spectrum should be cut off at high end of wave numbers. There are various choices of cutoff wave number κ_*. Here we choose one from [Thompson et al., 2005], since the author claimed that it gave the best fit with measurements:

$$\kappa_* = k\cos\theta\left(1+U_{10}/20\right)/7.5 \tag{4.32}$$

In (4.27) also enters $\Re$, the LHCP Fresnel reflection coefficient for sea water at L-band [Zavorotny and Voronovich, 2000]:

$$\Re = \frac{1}{2}\left[\frac{\varepsilon\cos\theta - \sqrt{\varepsilon - \sin^2\theta}}{\varepsilon\cos\theta + \sqrt{\varepsilon - \sin^2\theta}} - \frac{\cos\theta - \sqrt{\varepsilon - \sin^2\theta}}{\cos\theta + \sqrt{\varepsilon - \sin^2\theta}}\right] \tag{4.33}$$

where ε is the complex dielectric permittivity of sea water, and θ is the incidence angle.

According to Klein and Swift model:

at S = 35 ppt and T = 10 deg C ε = 74.62+i51.92 for L1 = 1.57542 GHz; ε = 75.02+i62.39 for

L2 = 1.22760 GHz; at S = 30; T = 10 deg C ε = 76.16+i55.30 for L1; ε = 75.02+i62.39: for L2.

Let us explore the behavior of the σ_0 as a function of the incidence angle with the scattering angle which corresponds to the nominal specular direction, i.e. $\theta_{inc} = -\theta_{sc}$. In this case

$$\sigma_0 = \frac{|\Re|^2}{2\sqrt{mss_x mss_y (1 - b_{x,y}^2)}} \tag{4.34}$$

Below is the plot of σ_0 for two winds (along the wind direction, $b_{x,y} = 0$) calculated according to above formulas and numbers. The roll-off at large incidence angle is due to the angular behavior of the LHCP reflection coefficient $\Re$.

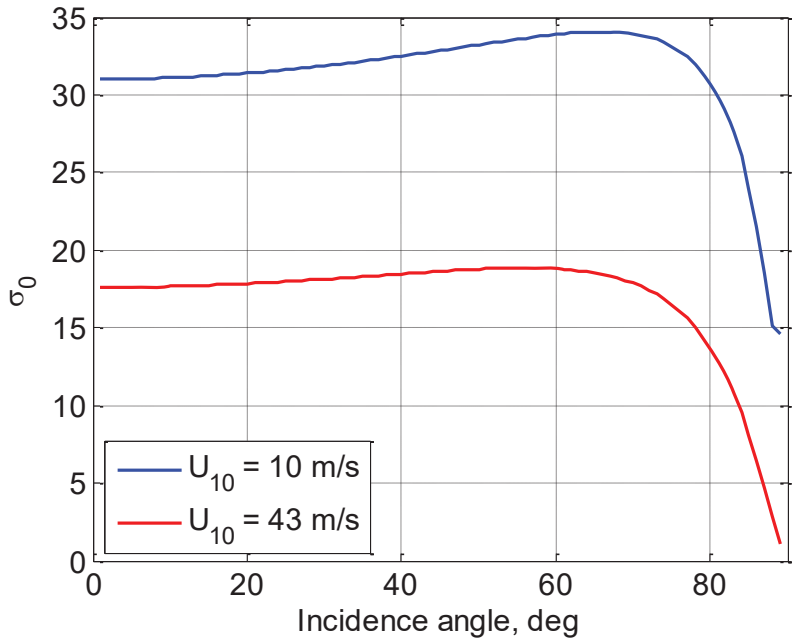

Figure 25. The bistatic radar cross section at the specular direction.

4.5.2 Thermal Noise

The second term in Eq. (4.25) is the background noise term. It can be written as double integral over the coherent integration time:

$$\left\langle \left| Y_n(t_0,\tau,f) \right|^2 \right\rangle = \int_0^{T_i} dt' \int_0^{T_i} dt'' a(t_0+t',f)a(t_0+t'',f). \\ \leftrightarrow \left\langle n(t_0+\tau+t')n^*(t_0+\tau+t'') \right\rangle. \tag{4.35}$$

Assume that the thermal noise is the "white" (delta-correlated) noise, i.e.:

$$\left\langle n(t')n^*(t'') \right\rangle = kT^\circ B_n b_n(t'-t''), \tag{4.36}$$

where k is Boltzmann constant; T° is the receiver noise equivalent temperature in Kelvin; $B_n = 1/T_{cor}$ is the receiver-front-end bandwidth, and T_{cor}, is a temporal correlation scale of the noise filtered by the front end;

$$b_n(t) = \int W_n(f)\exp(2i\pi ft)df; \qquad \int_0^{T_i} b_n(t)dt = T_{cor}. \tag{4.36}$$

Here $W_n(f)$ is the normalized temporal spectrum of the noise. Usually, background noise has a much smaller temporal correlation scale, T_{cor}, than the C/A chip-length, $\tau_{chip} = 1\,\mu$s. Or, in other words, that the noise bandwidth is much greater then the bandwidth of the C/A pseudo-random phase modulation of the GPS signals. Then, we can regard function $b_n(t'-t'')$ as a delta-function, so two integrations over time can be performed trivially. The result is:

$$\left\langle \left| Y_n(t_0,\tau,f) \right|^2 \right\rangle = T_i^2 kT^\circ B_D, \tag{4.37}$$

where $B_D = 1/T_i$ is the Doppler bandwidth of the signal.

The thermal noise is correlated between delay-Dopplers bins. The cross-correlation function of the noise in different bins is given by

$$\left\langle Y_n(t_0,\tau,f)Y_n^*(t_0,\tau',f') \right\rangle = \int_0^{T_i} dt' \int_0^{T_i} dt'' a(t_0+t',f)a^*(t_0+t'',f'). \\ \leftrightarrow \left\langle n(t_0+\tau+t')n^*(t_0+\tau'+t'') \right\rangle. \tag{4.38}$$

Since the noise is uncorrelated with the reference signal, the reference signal acts as a filter for the noise, causing it to be correlated with respect to delay and Doppler according to the GPS C/A code ambiguity function. (4.38) can be reduced to

$$\left\langle Y_n(t_0,\tau,f)Y_n^*(t_0,\tau',f')\right\rangle = T_i^2 kT^{\circ}B_D\Lambda^2(d\tau)\left|S(df)\right|^2 \tag{4.39}$$

In the forward model, zero mean white Gaussian noise is generated with respect to delay and Doppler using the power level in (4.37) and then convolved with the ambiguity function to produce the correct bin-to-bin correlations.

Now we can construct the signal-to-noise ratio (SNR). There are various definitions of SNR. We use here the simplest one, which shows how much the mean power of the signal exceeds the mean noise level:

$$SNR = \left\langle \left|Y_s(t_0,\tau)\right|^2 \right\rangle \Big/ \left\langle \left|Y_n(t_0,\tau)\right|^2 \right\rangle. \tag{4.40}$$

Remind that the SNR is the function of parameters τ and f_{dop}, i.e., the SNR is different for different portions of waveforms taken at different time delays and Doppler frequency offsets.

4.5.3 Statistics of the partially averaged GPS reflected signal affected by both thermal and speckle noise

Before, we considered an effect of additive thermal noise on the average SNR. It exists due to the physical temperature of both the receiver and the scene even in absence of the GPS reflected signal. Another type of noise, the multiplicative one, is a result of distractive and constructive interference of coherent signals arriving to the antenna upon scattering from a rough ocean surface. It is called Rayleigh fading, or speckle noise, and it is proportional to the signal itself. Below we consider statistics of the partially averaged signal affected by both thermal and speckle noise. In a real situation we deal with values averaged over a finite time interval. It happens because of, at least, two reasons. First, any measuring device has a finite time response. Second, often signals need to be accumulated over some time in order to improve signal-to-noise ratio. Since the integration, or averaging, time is finite the procedure doesn't lead to constant time-independent values. These partially averaged values are still random quantities and need to be described in statistical terms. Note that an instantaneous power U of the signal + noise does not comprise only of the sum of the instantaneous powers S and N for the signal and the noise, respectively. It contains also cross terms of s and n. Indeed

$$U(t) \equiv \left|u(t)\right|^2 = \left[s(t)+n(t)\right]\left[s^*(t)+n^*(t)\right] = S(t)+N(t)+C(t)+C^*(t), \tag{4.41}$$

where

$$C(t) = s(t)n^*(t). \tag{4.42}$$

During the measurement we obtain an estimate of the signal + noise from the power of the received signal + noise averaged over an arbitrary time interval T (a bar above refers to that type of averaging):

$$\overline{U}(t) \equiv \overline{S}(t) + \overline{N}(t) + \overline{C}(t) + \overline{C}^*(t) = \frac{1}{T}\int_{-T/2}^{T/2}\left[S(t+t') + N(t+t') + C(t+t') + C^*(t+t')\right]dt'. \quad (4.43)$$

An estimate of the signal can be done by obtaining an estimate of the signal + noise, then obtaining an estimate of noise from an independent measurement, and then subtracting one from another:

$$\widetilde{S}(t) = \overline{U}(t) - \overline{N}(t_0). \quad (4.44)$$

Since these estimates are obtained from an averaging over the finite period of time, the estimate of the signal, $\widetilde{S}(t)$, is a fluctuating quantity. The accuracy of the estimate is governed by the variance of estimate $\widetilde{S}(t)$. Since $\overline{U}(t)$ and $\overline{N}(t_0)$ are statistically independent the following equality holds

$$\sigma_{\tilde{S}}^2 = \sigma_{\overline{U}}^2 + \sigma_{\overline{N}}^2. \quad (4.45)$$

Observe that the mean value of the estimated power of the signal + noise is simply

$$\left\langle \overline{U} \right\rangle = \left\langle S \right\rangle + \left\langle N \right\rangle. \quad (4.46)$$

The variance of the total power of signal + noise is:

$$\sigma_{\overline{U}}^2 = \frac{1}{T^2}\left\langle \left| \int_{-T/2}^{T/2} \left[S(t') + N(t') + C(t') + C^*(t') \right] dt' \right|^2 \right\rangle - \left\langle \overline{U} \right\rangle^2. \quad (4.47)$$

The variance of the noise power is:

$$\sigma_{\overline{N}}^2 = \frac{1}{T^2}\left\langle \left| \int_{-T/2}^{T/2} N(t')dt' \right|^2 \right\rangle - \left\langle N \right\rangle^2. \quad (4.48)$$

Assuming that both the signal and the noise are stationary, and making several additional simplified assumptions without a loss of generality the standard deviation of the estimated signal power can be obtained in the following form:

$$\frac{\sigma_{\tilde{S}}}{\left\langle S \right\rangle} = \left[\left(1 + 2\left\langle S \right\rangle + 2T_{\text{int}} / \tau_{cor} \left\langle S \right\rangle^2 \right) / N \right]^{1/2}. \quad (4.49)$$

For $T >> \tau_{\text{cor}}$ the parameter $N = T / \tau_{cor}$ is the number of correlation intervals contained within the measurement time, *T*. Or, it could be interpreted as a number *N* of independent samples.

In order to proceed further we need to choose the value of the correlation time of the signal, τ_{cor}. The approach for calculation of the correlation time based on the power spectrum of the scattered signal, or equivalently, through the coherence function of the signal was developed in [Zuffada and Zavorotny, 2001, You et al., 2004, 2006].

Actually, the time correlation can be estimated using the Van Cittert-Zernike theorem. From it follows that the size of the field correlation zone at the wavelength λ is:

$$r_{cor} = \lambda R / D \tag{4.50}$$

where *R* is a distance from the surface to the receiver, and *D* is a size of the illuminated area. At the peak correlation power the illuminated area is the first annulus zone modified by the smaller, Doppler zone. The smallest size matters because it created the biggest r_{cor} which translates into largest correlation time $\tau_{cor} = r_{cor} / v_{sat}$ (See, e.g., Fig. 1. in [5]). The size of the Doppler zone is dictated by the coherent integration time. The analysis shows that $\tau_{cor} \approx 2T_i$, therefore, if T_i is 1 ms, $\tau_{cor} = 2$ ms. Taking this into account, (4.49) simplifies:

$$\frac{\sigma_{\tilde{S}}}{\langle S \rangle} = \left(1 + 2\langle S \rangle^{-1} + 2T_{\text{int}}\tau_{cor}^{-1}\langle S \rangle^{-2}\right)^{1/2} N^{-1/2} \approx \frac{1 + 1/\langle S \rangle}{\sqrt{N}} \quad . \tag{4.51}$$

From here we can produce an expression for the standard deviation of *S* (the SNR) after incoherent averaging over *N* statistically independent samples:

$$\sigma_{SNR} == \frac{\langle S \rangle + 1}{\sqrt{N}}. \tag{4.52}$$

Therefore, in this case, the standard deviation of partially averaged SNR is proportional to the average SNR plus one, and can be reduced by $\sqrt{N}$. In a general case of arbitrary τ_{cor} and T_i

$$\sigma_{SNR} = \frac{\sqrt{\langle S \rangle^2 + 2\langle S \rangle + 2T_{\text{int}}\tau_{cor}^{-1}}}{\sqrt{N}} \tag{4.53}$$

4.6 Speckle Noise

The reflected signal received by each CYGNSS observatory is formed by contributions from a large number of independent surface scatterers. This random scattering generates multiplicative, self-noise (i.e. Rayleigh fading or speckle noise), which is proportional to the signal. This is in contrast to thermal noise, which is additive. This section describes how this speckle noise is accounted for in the forward model.

Recall that the bistatic radar equation from Section 4.5.1. The expected value of the power of the reflected signal versus delay and Doppler can be rewritten as

$$\left\langle \left| Y_s(t_0,\tau,f) \right|^2 \right\rangle = \iint H(\vec{\rho})\Lambda^2(\tau,\vec{\rho}) \left| S(f,\vec{\rho}) \right|^2 d^2\rho, \tag{4.54}$$

where

$$H(\vec{\rho}) = T_i^2 \frac{P_T G_T \lambda^2 G_R}{(4\pi)^3} R_0^{-2} R^{-2} \sigma_0(\vec{\rho}) \tag{4.55}$$

represents the contribution of each location on the surface to the total expected power of the reflected signal at a particular delay and Doppler.

In the forward model, DDMs are formed from integrations performed over finite time intervals rather than expected values (such as in equation 4.54). We must model the effect of speckle noise, but, for the surface areas involved in space-borne GPS reflectometry, it would be unrealistic to instantiate the actual random rough surface and use a computational electromagnetics approach. Rather, we have chosen a suitable to accurately capture the effects of speckle noise.

First, we take the square root of the power contribution in equation 4.55 and include a time varying phase term $\phi(t,\rho)$ to make the contribution complex,

$$h(t,\rho) = \sqrt{H(\rho)} e^{j\phi(t,\rho)}. \tag{4.54}$$

This is an approximate representation of the contribution of each location on the surface to the voltage DDM, and can be thought of as the transfer function over the surface. The approximate voltage DDM is given by

$$Y_s(t,\tau,f) = \iint h(t,\vec{\rho})\Lambda(\tau,\vec{\rho}) S(f,\vec{\rho}) d^2\rho. \tag{4.55}$$

The DDM is formed by integrating for 1 second, t will be between t_0 and (t_0+1), where t_0 is the start of the integration. This produces

$$\left| Y_s(t_0,\tau,f) \right|^2 = \int_{t_0}^{t_0+T} Y_s(t,\tau,f) Y_s^*(t,\tau,f) dt, \tag{4.56}$$

where T =1. The phase term $\phi(t,\rho)$ must be chosen such that the expectation of equation 4.56 is equal to 4.54. Also, it must also result in the temporal correlation of speckle noise.

First, a random phase, $\phi_0(\rho)$, is associated with each location on the surface. This random phase is assumed uniformly distributed between 0 and 2π and represents the phase shift caused by the random rough surface at that location. This phase will evolve in time according to the changing geometry of the satellites. Thus, the total phase associated with the reflection of a particular point on the surface is a combination of the random phase and phase associated the total path length,

$$\phi(\rho) = \phi_0(\rho) + \frac{2\pi}{\lambda} R(t,\rho), \tag{4.57}$$

where λ is the wavelength at the GPS L1 center frequency, and $R(t,\rho)$ is the total path length from the transmitter to the surface location at ρ and up to the receiver at time *t*. Since it is such a short duration, the time variation in the path length can be accurately approximated using the Doppler at the start of the integration $f_D(t_0,\rho)$,

$$R(t,\rho) = R(t_0,\rho) - (t-t_0)\lambda f_D(t_0,\rho). \tag{4.58}$$

Each point of the surface will exhibit a different time varying phase, depending on the relative motion of the satellites. Over short time delays (i.e. less than one millisecond), the change in geometry will be small, and the speckle noise will exhibit time correlation. For longer delays, the speckle noise will be completely uncorrelated, as is expected from reflections from a real ocean surface.

5 L2 Wind Speed Retrieval Algorithm

The L2 wind speed retrieval algorithm described here is the version implemented in the CYGNSS Science Operation Centre (SOC) to produce the baseline Level 2 and 3 wind speed science data products. It is similar to the algorithm described in [Clarizia and Ruf, 2016], although the observable computation and the time-averaging approach are here slightly different, and some of the filters, which were implemented in [Clarizia and Ruf, 2016] to demonstrate that the resolution requirements are met, are not implemented by the SOC. The Geophysical Model Functions (GMFs) used to map the observables into wind speed are empirically derived from large populations of near-cincident matchups between on-orbit measurements by CYGNSS and an independent estimate of the wind speed. Two sets of GMFs are used. One is derived in Fully Developed Seas (FDS) conditions using coincident matchups with MERRA-2 model wind speeds. The other is derived using matchups with coincident HWRF numerical weather prediction wind speeds during CYGNSS obverpasses of tropical cyclones. The latter GMF is refered to as Young Seas with Limited Fetch (YSLF). Details about the generation of both GMFs are given below in Section 5.4.

The basic steps for the L2 retrieval algorithm can be summarized as follows:

1. Two DDM “observables”, the DDM Average (DDMA) and the Leading Edge Slope (LES), are derived from L1b DDMs of Radar Cross Section (RCS) and DDMs of effective scattering area, both output by the L1 calibration procedure described in [Gleason et al., 2016; Gleason et al., 2018];
2. FDS wind speeds are estimated from the individual L1 observables (either DDMA or LES) by inversion of their corresponding FDS GMF. The DDMA and LES winds are then optimally combined using a Minimum Variance (MV) Estimator to produce the final FDS wind speed.
3. YSLF wind speeds are more appropriate to use near strong, organized storms in which the sea state is not fully developed with respect to the local wind speed due to limited sea age and fetch length conditions. In this case, an initial YSLF wind speed is estimated from the DDMA L1 observable by inversion of the YSLF DDMA GMF. The DDMA but not LES is used as it has significantly greater sensitivity at high wind speeds. The YSLF DDMA wind speed is combined with the FDS MV wind speed using a tapered linear combination, in which the FDS wind is given more weight at low wind speeds and the YSLF wind is given more weight at high wind speeds, to produce the final YSLF wind speed.
4. Time averaging is applied to consecutive samples to produce a consistent 25 km spatial resolution data product, whenever it is appropriate to do so (the appropriate level of averaging depends on the incidence angle of the sample).

These steps are described further in the subsequent sections.

5.1 Sample populations for GMF training data

The L1 observables used to develop the FDS GMFs were obtained from on-orbit measurements made by the CYGNSS constellation during the period 1 Jan – 31 Dec 2019. Included are measurements over the entire globe matched up with coincident 10 meter referenced ocean surface wind speeds provided by the Modern-Era Retrospective analysis for Research and Applications, Version 2 (MERRA-2). The original MERRA reanalysis dataset was released in 2009 by the NASA Global Modeling and Assimilation Office (GMAO). MERRA is based on a version of the GEOS-5 atmospheric data assimilation system that was frozen in 2008. MERRA data were produced on a 0.5° × 0.66° grid with 72 layers. The version 2 of MERRA data, known as MERRA-2, provides data from the beginning in 1980 and runs a few weeks behind real time. Alongside the meteorological data assimilation using a modern satellite database, MERRA-2 includes an interactive analysis of aerosols that feed back into the circulation, uses NASA's observations of stratospheric ozone and temperature (when available), and takes steps towards representing cryogenic processes. More details and information on MERRA-2 products can be found at https://gmao.gsfc.nasa.gov/reanalysis/. Bilinear interpolation in space and linear interpolation in time of the reported MERRA-2 wind product are used to estimate u_{10} at the times and locations of the CYGNSS specular point observations.

The L1 observables used to develop the YSLF GMF were obtained from CYGNSS observations in summer/fall 2018 during overpasses of storms in the Atlantic and Pacific Oceans at and above Tropical Storm intensity. The measurements were matched up with coincident 10 m referenced ocean surface wind speeds produced by the NOAA/NCEP Hurricane Weather Research and Forecasting model (HWRF). For each storm overpass, all CYGNSS data within 400 km of the storm center are examined. The location of the storm center at the time of a CYGNSS observation is determind using the NOAA National Hurricane Center's Best Track center fixes. The storm center at that time is estimated by linear interpolation in time of the closest Best Track fixes before and after the observation. A matchup is defined if the location of a CYGNSS sample and HWRF grid point are within 3 km of one another. The HWRF wind speed for that matchup is the interpolation in time of the closest HWRF wind speed before and after the observation. However, if the two wind speeds differ by more than 5 m/s, that matchup is discarded from the population.

The storms included in the matchup population are:

- Atlantic: Florence, Gordon, Helene, Isaac, Michael, Oscar
- East Pacific: Hector, John, Miriam, Norman, Olivia, Rosa, Sergio, Willa
- West Pacific: Cimaron, Jebi, Jelawat, Jongdari, Mangkhut, Maria, Shanshan, Soulik, Trami, Yutu

A histogram of all the HWRF winds speeds included in the matchup data set are shown in Fig. 26. the high percentage of samples at lower wind speeds generally occur near the outer perimeter of the storms and the highest wind speeds are ~ 70 m/s.

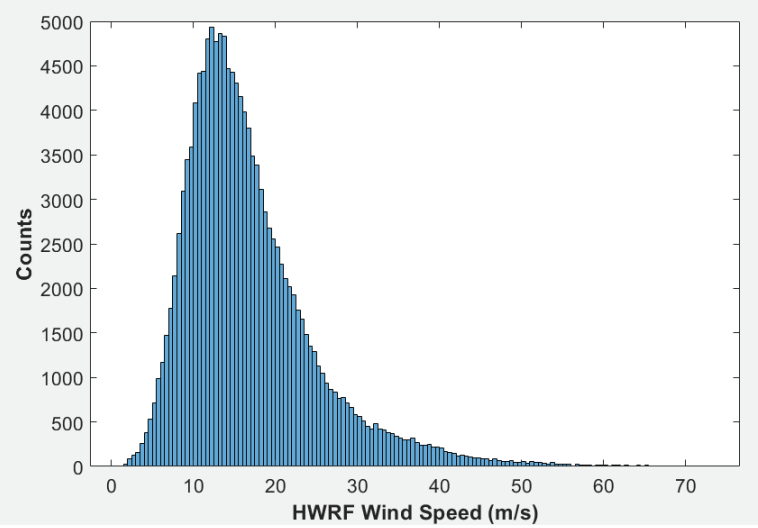

Figure 26. Histogram of wind speeds in the matchup population used to train the YSLF GMF.

5.2 DDM Observables: DDMA and LES

Here we present a definition of the observables we use for our retrieval algorithm, derived from the outputs of the L1b calibration described in [Gleason et al., 2016; Gleason eta al, 2018].

5.2.1 Definition of Delay-Doppler Map Average (DDMA)

The DDMA is the average of the L1b DDM of the Normalized Radar Cross Section (NRCS) over a given delay/Doppler range window around the specular point [Clarizia et al., 2014, Clarizia and Ruf, 2016]. The DDMA exploits the DDM region which is most sensitive to varying wind speed, namely the scattered power at and around the specular point. Notably, the DDMA has the advantage of mitigating the effect of noise, by averaging the power over the area around the SP, rather than the power value at the single SP pixel. An illustration of a DDM of scattered power simulated with the CYGNSS E2ES, and a qualitative example of the area where the DDMA is calculated (shown as the “black box”) is shown in Figure 22.

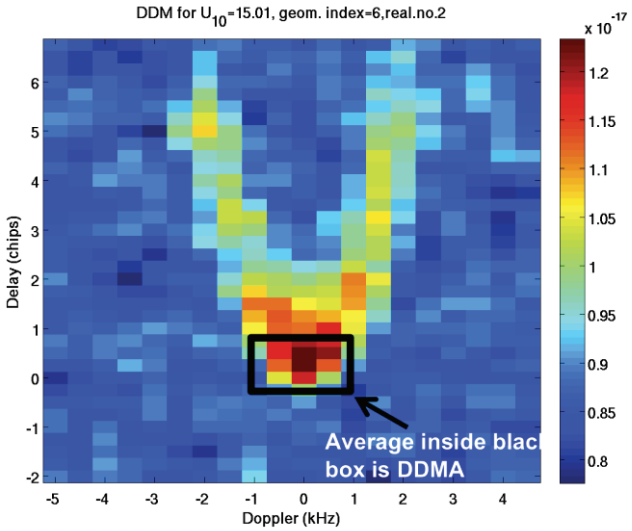

Figure 22. A simulated DDM and the DDM area where the DDMA is calculated.

5.2.2 Definition of Leading Edge Slope (LES)

The LES is the slope of the leading edge of the Integrated Delay Waveform (IDW), calculated over a specific delay range [Clarizia et al., 2014, Clarizia and Ruf, 2016]. IDWs are obtained as incoherent integration of DDMs of NRCS along the Doppler dimension, and over a range of Doppler frequencies. Figure 23 illustrates simulated IDWs of integrated power, for a fixed geometry and for different wind speeds. The corresponding IDWs of NRCS would only differ from these for a constant scaling factor. Figure 28 highlights how the slope of the IDW rising edge decreases for increasing wind speeds.

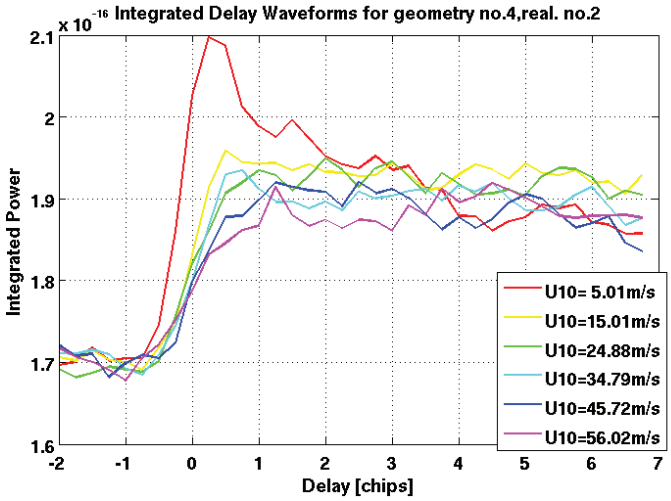

Figure 23. Integrated Delay Waveforms computed from DDMs simulated using different wind speeds.

5.2.3 Calculation of DDMA and LES Observables

The DDMA is computed as the sum of the L1b DDM of Radar Cross Section (RCS) over a delay/Doppler window of respectively -0.25 chips to 0.25 chips, and -1 kHz to 1 kHz, divided by the effective scattering area over the same window. The selected delay/Doppler window is a 3x5 matrix, due to the 0.25 chip delay resolution and the 500 Hz Doppler resolution of the CYGNSS DDMs.

The sum of L1b RCS DDMs can be expressed as follows:

$$\sigma_{DDMA} = \sum_{i=1}^{3} \sum_{j=1}^{5} d(i,j) \tag{5.1}$$

where $d(i,j)$ represents the $(i,j)^{th}$ delay/Doppler bin of the L1b DDM of RCS. The motivation for the choice of such a delay/Doppler window is documented in [Clarizia and Ruf, 2016].

The LES is calculated as the slope of IDWs obtained from L1a DDMs of received power using the same DD window as the DDMA. The IDWs are obtained by summing the 5 L1a DDM columns (along the Doppler axis) that span the Doppler interval from – 1 kHz to 1 kHz. The leading edge slope (LES) of the IDW leading edge is given by

$$a_{LES} = \frac{N\sum_{i=1}^{3} x_i y_i - \sum_{i=1}^{3} x_i \sum_{i=1}^{3} y_i}{N\sum_{i=1}^{3} x_i^{\,2} - \left(\sum_{i=1}^{3} x_i\right)^2} \tag{5.2}$$

where x_i is the *i-th* value of the delay within the [-0.25 0.25] chip interval, y_i is the corresponding IDW value, and $N=3$ is the number of points of the IDW used for the LES computation.

The effective scattering area of the 3x5 region that is used for the L1b DDMA and LES calculation is computed from the DDMs of ideal area and effective area for individual DDM bins, both outputs of the L1b calibration process. The DDM effective area of individual bins within the selected DD window are not simply summed as this would have the effect of accounting for the spreading of effective area into neighboring bins multiple times, which would result in too big of an effective area. Therefore, the approximation we use for the effective area A_{eff} is:

$$\begin{aligned} A_{eff} &= \sum_{i=1}^{3}\sum_{j=1}^{5} A_{id}(i,j) + \frac{1}{2}\sum_{i=1,3}\sum_{j=1,5} \Delta A(i,j) + \frac{1}{4}\sum_{i=1,3}\sum_{j=2,3,4} \Delta A(i,j) \\ \Delta A(i,j) &= A_{eff}(i,j) - A_{id}(i,j) \end{aligned} \tag{5.3}$$

where $A_{id}(i,j)$ and $A_{eff}(i,j)$ are the $(i,j)^{th}$ bin of the ideal and effective scattering area DDM, respectively.

The final equations for the DDMA and LES are given by:

$$DDMA = \frac{\sigma_{DDMA}}{A_{eff}}$$
$$LES = \frac{\alpha_{LES}}{A_{eff}} \quad (5.4)$$

Computation of the DDMA and LES is also explained in detail in [Clarizia and Ruf, 2016], although in that case the DDMA and LES of RCS are normalised by the ideal area, calculated simply as the sum of the DDM ideal area bins within the DD window considered for the observables.

5.3 Time Averaging

An extra processing step that contributes to improve the performances of the algorithm is to apply time averaging to the collected data.

The DD window chosen for the observable computation corresponds to a given Instantaneous Field of View (IFOV), and whose square root is shown as a function of incidence angle in Figure 24.

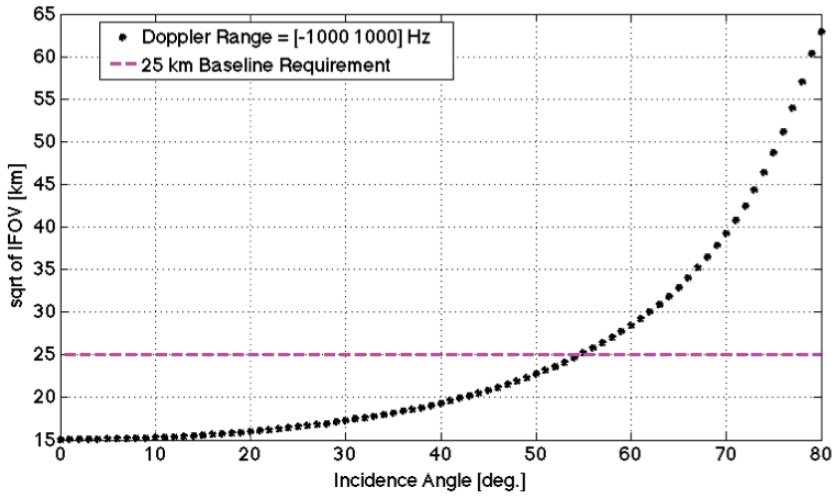

Figure 24. square root of Instantaneous Field of View (IFOV) versus incidence angle, for the DD window spanning -0.25 chip to 0.25 chip, and -1 kHz to 1 kHz (black dots), along with the requirements for the CYGNSS mission (dashed magenta line).

The IFOV is defined here as the physical area at the intersection between the iso-range ellipse at 0.25 chips, and the iso-Doppler lines at -1 kHz and 1 kHz. Full details about the relationship between physical area, IFOV and incidence angle are contained in [Clarizia and Ruf, 2016] and repeated also in Appendix A.

It is clear from Figure 24 that for a range of incidence angles lower than approximately 54.5°, the IFOV of the collected samples is below the spatial resolution requirement of 25 km. For all these cases, it is possible to average a number of consecutive samples in time to achieve the spatial resolution limit of 25 km. The maximum number of samples *n* that can be averaged can be easily calculated, using some simplifications, and after a few simple calculations it turns out to be [Clarizia and Ruf, 2016]:

$$n = \frac{EFOV^2}{6\sqrt{IFOV}} - \frac{\sqrt{IFOV}}{6} + 1 \tag{5.5}$$

For each incidence angle, it is therefore possible to know the exact number of samples that can be averaged, if a 25km requirement on the spatial resolution must be met. A pre-computed Lookup Table of *n* as a function of incidence angle is used in the time-averaging process of the algorithm, and this table is reported in Appendix B. Of course, the calculation of *n* uses simplified assumptions, and does not take into account several aspects, like the real trajectory of the specular point on the surface, or the real shape of the IFOV, which is ideally assumed to be a square in equation (5.5), but which depends instead on the configuration of the iso-delay and iso-Doppler lines at the ranges selected for the computation of the observables. However, these simplifications are valid enough to allow a reliable estimation of the number of samples to be averaged together.

Some graphical examples of time averaging are illustrated in Figure 5, where the different SP tracks for a single CYGNSS observatory are shown as blue crosses, the sample considered for time averaging is shown in red, and the consecutive samples to be averaged together with the red one are highlighted with black circles.

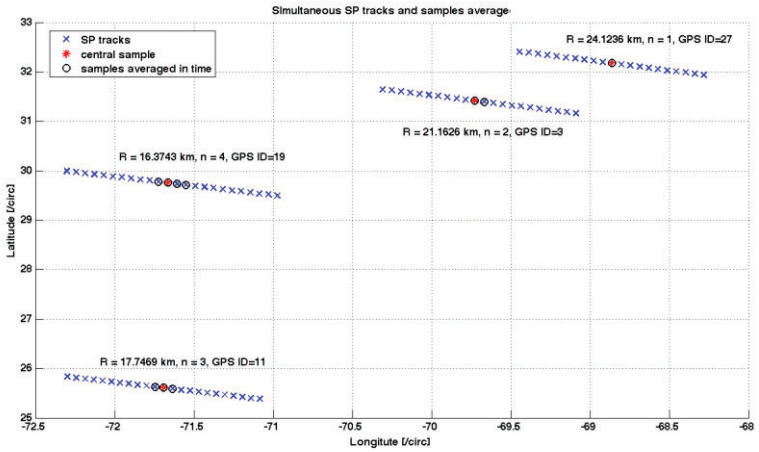

Figure 5. An illustration of how the Time Averaging (TA) algorithm works, for four simultaneous SP tracks acquired by a single CYGNSS observatory.

The time-averaging implementation used in the SOC algorithm follows a few simple rules which mostly aims at avoiding geolocation ambiguities in the resulting time-averaged samples, and that can be summarized as follows:

1) The non-valid samples are excluded from the time averaging. These are either the samples with the overall quality flag set to 0 (see section 5.7), or those whose DDMA or LES value is not valid (-9999).
2) The number of samples to time-average before the central sample (i.e. preceding the central samples in time along the track) is always equal or higher than the number of samples to time average after the central sample;
3) The difference between number of samples before and number of samples after cannot be greater than 1;

These rules were not applied in the algorithm presented in [Clarizia and Ruf, 2016], and as a result of them there are cases when the number of time-averaged samples (n) is less than that prescribed by the incidence angle. As a consequence of that, the amount of time-averaging applied to the SOC algorithm is in some cases less than that applied in [Clarizia and Ruf, 2016].

5.4 Generation of Geophysical Model Functions

5.4.1. Generating FDS GMF

The dataset used to generate the GMF is formed as the L1b observable, computed over a delay range of [-0.25 0.25] chips and a Doppler range of [-1000 1000] Hz, and acquired with high enough Range-Corrected Gain, or RCG. This is defined as the receiver antenna gain at the specular point multiplied by the range losses there, as given by

$$RCG = \frac{G_{RX}^{SP}}{\left(R_0^{SP} R^{SP}\right)^2} 10^{27} \tag{5.6}$$

where the range terms are in units of meters and the numeric (not dB) value of the receive antenna gain is used. The scale factor of 10^{27} is applied in order to produce values of order 1-100. The RCG represents those factors affecting the received signal strength which are related to the measurement geometry and are independent of the surface scattering cross section. It is used to filter data according to their expected signal-to-noise quality. Typical ranges of low, medium and high RCG are, respectively, <10, 10-30, and >30.

For GMF generation we use all CYGNSS measurements made in 2019 data with v3.0 Level 1 calibration and the following filters:

The L1 observables are filtered prior to use as part of the training used to derive the empirical GMF. The filters are for reasons of quality control. Specifically:

- The Doppler coordinate of the specular point in the DDM is required to be greater than the lowest possible value in the map and less than the highest possible value. This discards cases where it is at the edge of the map and the computed Doppler coordinate may be incorrect. In practice, this happens less than 0.1% of the time.
- The delay coordinate of the specular point in the DDM is required to be greater than the lowest possible value in the map and less than the highest possible value. This discards cases where it is at the edge of the map and the computed delay coordinate may be incorrect. In practice, this happens less than 0.1% of the time.
- All NaN values of the observables are discarded. This eliminates samples for which noise in the calibration data can produce non-physical calibrated L1 data. In practice, this happens less than 0.1% of the time.
- The observables are required to be non-negative. This eliminates samples for which noise in

the calibration data can produce non-physical calibrated L1 data, as well as measurements which are very close to the measurement noise floor. In practice, this happens less than 0.1% of the time.

- All measurements are discarded for which the spacecraft star tracker is not tracking due to solar contamination. Some reported spacecraft attitude data during sun outages are known to be erroneous (with inaccuracies greater than the error allocation in the L1 calibration algorithm for attitude knowledge). This only occurs when the outage is especially long, but all sun outage data are flagged and removed as a precaution. In practice, this happens less than 1% of the time.
- Measurements are discarded in the reported spacecraft roll angle and the commanded roll angle differ by more than than 1° in absolute value. In practice, this happens less than 1% of the time.
- All data with a CYGNSS Range Corrected Gain (RCG) of less than 3 are discarded. RCG is a composite measure of receive signal strength that combines the receive antenna gain in the direction of the specular point with the R^{-2} propagation range loss from the GPS transmitter to the specular point and from the specular point to the CYGNSS receiver. In practice, data with an RCG > ~1 can typically produce useful wind speed retrievals, but only data with a higher SNR are used to train the empirical GMF.

The GMF is 2-dimensional – a function of both wind speed and incidence angle – and is derived separately for the DDMA and LES observables. The GMF maps the selected observable to the MERRA-2 "ground truth" wind speed. The GMFs are computed in the form of LUTs of DDMA and LES values. The methodology used to derive the GMF is described in detail in [Clarizia and Ruf, 2020]. It was originally developed by [Freilich and Challenor, 1994] to derive an empirical altimeter wind speed model function. It is based upon the assumption that a model function M relating the wind speed w to the observable exists, as given be

$$w = M(O) \tag{5.7}$$

Where O denotes the observable. It is assumed that w varies monotonically with O, such that the inverse model function $O=M^{-1}(w)$ also exists.

The CDF of the observable $F_O(O')$ can be written as follows:

$$F_O(O') = P(O \le O') = P(M^{-1}(w) \le O') = \tag{5.8}$$

$$= P\big(w \ge M(O')\big) = 1 - F_w(M(O')) \tag{5.9}$$

If $F_O(O') = \beta$, then the corresponding wind speed $w' = M(O')$ is the wind speed for which $1 - F_w(w') = \beta$. The detailed application of this method to the case of CYGNSS is described in

[Clarizia and Ruf, 2020] and summarized here for the case of the DDM observable. A similar approach is followed for the LES observable.

1) Specific axes are set for the wind speed, the incidence angle, and the DDMA. The wind speed axis is chosen to span the range from 0.05 m/s to 69.95 m/s with a 0.1 m/s step. The incidence angle axis ranges from 1° to 70° with a step of 1°. The axis for the DDMA observable ranges from the minimum to the maximum value of the observable measured for the dataset and has 700 elements. We denote *wy* as the generic wind speed value of the wind speed axes, and *DDMA'* as the generic observable value of the observable axis;
2) The wind speed CDF values $F_{wy}(wy')$ are computed for each value of the wind speed axes.
3) For each 1° incidence angle bin the DDMA values *DDMAx* corresponding to *wy*, and forming the LUT are found as follows:
    a. The observables CDF values $F_{DDMA}(DDMA')$ are computed for each value of the DDMA observable axis.
    b. The CDF values of the observables corresponding to the wind speed axes are denoted as β and set as $\beta = 1 - F_{wy}(wy')$;
    c. The observables *DDMAx* corresponding to the wind speed axes are derived via linear interpolation of the $F_{DDMA}(DDMA')$ versus the DDMA axis, at the CDF values β;

After the CDF-matching GMF is generated, it is passed through a running average filter, first with respect to incidence angle (averaging window +/- 10 deg) and then with respect to wind speed (averaging window +/- 3 m/s), to smooth out variations in the dependence on both incidence angle and wind speed.

The final GMFgiven by (*DDMAx* and *wy*) for every incidence angle bin maps wind speed as a function of both the observable and the incidence angle. The advantage of this method, compared to the one previously used in the baseline algorithm to derive the FDS GMF, is its simplicity, effectiveness, and the fact that it does not require empirical tuning of the GMF [Clarizia and Ruf, 2020]. The current method is entirely based the empirical CDFs of the observables used and geophysical parameters to retrieve, and it can be applied to any GNSS-R observable, provided that the wind speed varies monotonically with the observable.

Examples of the resulting GMFs for both DDMA and LES observables are shown in Fig. 31.

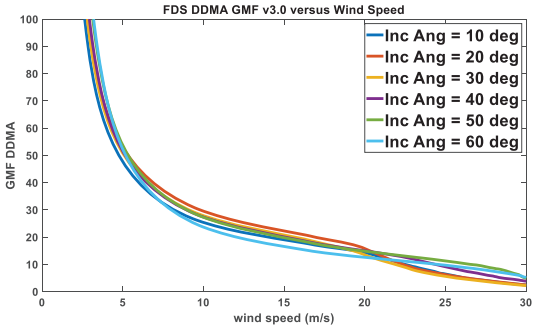

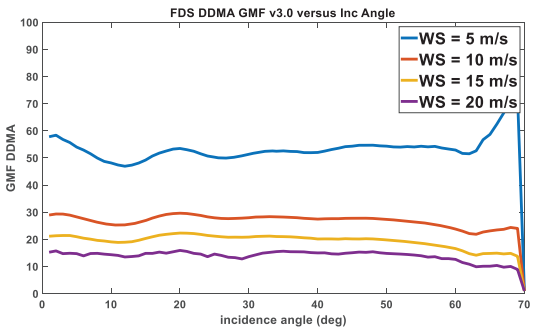

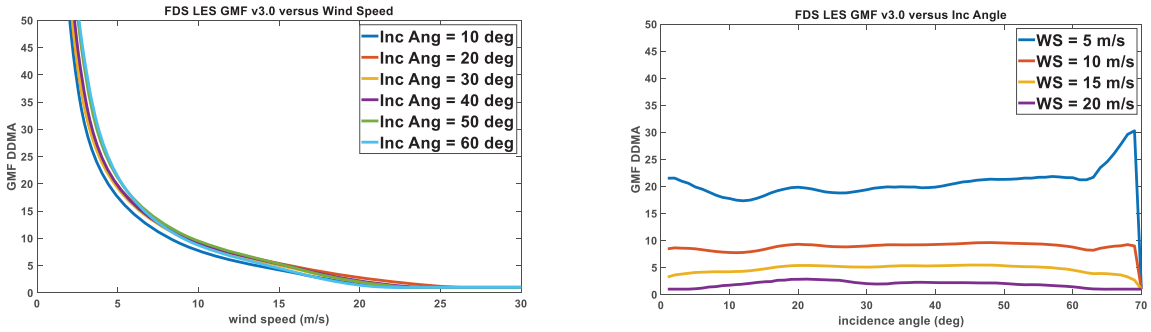

Figure 6. FDS GMFs for the two Level 1 observables, σ_o or DDMA (top) and LES (bottom), as functions of wind speed (left) and incidence angle (right).

5.4.2. Generating YSLF GMF

The population of wind speed matchups used to generate the YSLF GMF is considerably smaller than that used for the FDS case because it is restricted to storm overpasses. In addition, the CDF-matching technique used in the FDS case would be less appropriate to use here because the statistical distribution of wind speeds in storms is much less repeatable. For this reason, the YSLF GMF is created by binning the L1 observables into discrete steps in HWRF wind speed and in the incidence angle of the measurement geometry and averaging the L1 samples in each bin. In addition, only the DDMA L1 observable is used for retrieval of YSLF wind speeds in sorm conditions because the LES observable has insufficient sensitivity to changes in wind speed under high wind conditions.

The L1 observables are filtered prior to use as part of the training used to derive the empirical GMF for reasons of quality control. The filters used are the same as those in the FDS case except that the minimum threshold for acceptable RCG values is raised from 3 to 10. This is done to raise the minimum acceptable signal-to-noise quality of the observations since, in general, scattering from the ocean in high wind conditions tends to be weaker.

The behavior of the empirical GMF as a function of u_{10} and θ_{inc} is smoothed by allowing sequential bins in either dimension to overlap. In the incidence angle dimension, the bin center is incremented every 1 deg from 1 to 70 deg and all samples are included within +/- 20 deg of the center. In the wind speed dimension, the bin center is incremented every 0.1 m/s from 0.05 to 34.95 m/s and all samples are included within a variable bin width that varies according to the population density of samples as a function of wind speed. Specifically, the bin widths used are:

- +/- 0.4 m/s ($u_{10} \leq 1$ m/s)
- +/- 0.5 m/s ($1 < u_{10} \leq 2$ m/s)
- +/- 0.6 m/s ($2 < u_{10} \leq 3$ m/s)
- +/- 0.7 m/s ($3 < u_{10} \leq 5$ m/s)
- +/- 0.8 m/s ($5 < u_{10} \leq 9$ m/s)
- +/- 1.0 m/s ($9 < u_{10} \leq 11$ m/s)

- +/- 1.5 m/s ($11 < u_{10} \leq 14$ m/s)
- +/- 2.0 m/s ($14 < u_{10} \leq 17$ m/s)
- +/- 2.5 m/s ($17 < u_{10} \leq 25$ m/s)
- +/- 3.0 m/s ($25 < u_{10} \leq 35$ m/s)
- +/- 4.0 m/s ($35 < u_{10} \leq 45$ m/s)
- +/- 5.0 m/s ($45 < u_{10}$)

A weighted average of all samples within twice these bin width ranges is performed. Samples within +/- one bin width of the bin center are given twice as much weight as those between 1×binwidth and 2×binwidth from the bin center. This tapered weighting approach reduces the introduction of artificial higher frequency components into the GMF than are present in the original discrete empirical samples.

The GMF is also forced to be monotonic as a function of wind speed. The GMF value at 7.05 m/s is computed first (since this is generally the most probable wind speed and so has the largest population of samples in its near vicinity). GMF values are then sequentially computed in steps of 0.1 m/s above and below this value using the averaging scheme described above. However, values are allowed to either decrease or stay the same with increasing wind speed, and increase or stay the same with decreasing wind speed. This limits the introduction of non-physical variations into the GMF due to undersampling of certain parts of the (wind speed, incidence angle) state space. In practice, this monotonicity algorithm is only enforced at the highest and lowest wind speeds in the population, where the sampling density tends to be lowest.

After the bin-averaged GMF is generated, it is passed through a final running average smoothing filter, first with respect to incidence angle (averaging window +/- 10 deg) and then with respect to wind speed (averaging window +/- 3 m/s).

Examples of the resulting YSLF GMFas a function of wind sped and incidence ang;e are shown in Fig. 32.

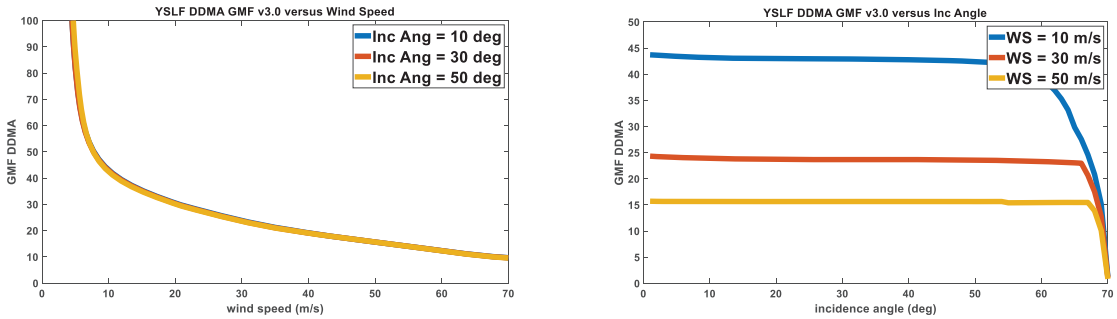

Fig. 32. YSLF GMF of σ_0 (DDMA) versus wind speed at different incidence angles (left) and versus incidence angle at different wind speeds (right).

5.5 Wind Estimation using the GMF

For each point of the performance evaluation dataset (either DDMA or LES), a wind speed is estimated using the GMF. The estimation is done through interpolation, when the observable value falls within the range of values spanned by the GMF, and through extrapolation outside of such range. The mathematical equations to estimate the wind through interpolation is given by (referring to DDMA):

$$\hat{U}_{10}^{DATA} = U_{10}^{LUT} + \alpha\left(DDMA^{DATA} - DDMA\left(U_{10}^{LUT}\right)\right)$$
$$\alpha = \left(V_{10}^{LUT} - U_{10}^{LUT}\right) \Big/ \left(DDMA\left(V_{10}^{LUT}\right) - DDMA\left(U_{10}^{LUT}\right)\right) \quad (5.10)$$

where $DDMA^{DATA}$ is the DDMA value within the DDMA range of the GMF, $\hat{U}_{10}^{DATA}$ is the wind estimation for DDMA value, the pair of values $\left(U_{10}^{LUT}, DDMA\left(U_{10}^{LUT}\right)\right)$ are the y and x coordinates of the GMF entry whose DDMA value (x coordinate) is immediately below $DDMA^{DATA}$, and the pair of values $\left(V_{10}^{LUT}, DDMA\left(V_{10}^{LUT}\right)\right)$ are the y and x coordinates of the GMF whose DDMA value is immediately above $DDMA^{DATA}$.

The mathematical expression for estimating the wind through extrapolation is given by

$$\hat{U}_{10}^{EXT} = U_{10}^{i\ LUT} + \alpha^{EXT}\left(DDMA^{DATA} - DDMA\left(U_{10}^{iLUT}\right)\right) \quad i = 1, n \quad (5.11)$$

where the values *1* and *n* for the index *i* refer, respectively, to the smallest and largest value of the wind range, $\hat{U}_{10}^{EXT}$ is the wind value to estimate through extrapolation, and α^{EXT} is the slope estimated from the 2 points of the LUT with lowest wind (if *i=1*) or from the 3 points of the GMF with highest wind (if *i=n*).

5.6 FDS Wind Speed Additional Processing

5.6.1 MV Estimator

The FDS wind speed estimates from DDMA and LES are combined together to produce a Minimum Variance (MV) estimator. The MV estimator exploits the degree of decorrelation between the errors in the individual estimates to minimize the net RMS error in the combined wind speed estimate. An advantage of such an estimator lies in the fact that its RMS error will always be better than or equal to the lowest RMS error in the retrieved wind speeds among the individual observables. The lower the correlation between errors in pairs of individual estimators, the more independent information is provided by each estimate and the better the performance of the combined MV estimate. The MV estimator is built as a linear combination of the original estimators, as shown in [Clarizia et al., 2013]:

$$u_{MV} = \boldsymbol{m} \square \boldsymbol{u} \quad (5.12)$$

where $\boldsymbol{u}$ is the vector of individual estimates (from DDMA and LES) and $\boldsymbol{m}$ is the vector of coefficients. The coefficients are obtained by requiring that the MV estimator be unbiased (i.e. the expected value of its retrieval is equal to the true quantity to be estimated) and by minimizing its variance. The mathematical derivation of the coefficients for the estimator is given in [Clarizia et al., 2013], [Clarizia and Ruf, 2016].

The matrix of covariance values is estimated from the retrieval errors and is determined separately for different ranges of mean DDMA and LES wind speeds. This is done because the correlation between the errors in the retrievals from the two observables varies with wind speed due to the inverse relationship between wind speed and SNR for GNSS-R estimates. This allows the MV estimator to contribute more to the performance improvement for those data where the performance is worse due to a lower SNR, so in a sense the MV approach will help where it is needed most. Detailed descriptions of the relative weights given to the DDMA- and LES-based wind speed estimates as they are combined to produce the MV estimate are given in Appendix B.

A wind speed uncertainty is also associated with each final retrieved wind. The uncertainty values are stored in the form of a LUT indexed by RCG interval and by wind speed interval, and then assigned to each retrieved wind depending on the RCG of the sample and the retrieved wind itself. The numerical values of this LUT are reported in table B4 in Appendix B.

5.6.2 CDF-Matching Debias

An adjustment is made to both the DDMA and LES winds as well as to the MV wind speed to produce the final 'wind_speed' data product reported in the L2 data files. They are debiased so their probability distribution, assembled using a global set of measurements over a full year, matches that of near-coincident wind speeds produced by MERRA-2. The debiasing algorithm consists of a re-mapping of the original wind speeds to their debiased value. At very high winds, where sample populations are low and there is less confidence in the representativeness of the empirical probability distributions, the re-mapping tapers from full adjustment to the MERRA-2 distribution (at low winds) to no adjustment of the MV winds (at highest retrieved winds). The exact transition wind speed from full to tapered adjustment is determined by the sample size of the wind speed population and is typically near 20-25 m/s. Re-mapping parameters are derived independently for each antenna (starboard and port) of each FM and as a function of incidence angle, azimuth angle, and commanded roll state. Example CDF matching wind speed maps are shown in Appendix B.

5.7 YSLF Wind Speed Additional Processing

Tapered blending of FDS and YSLF wind speeds

The relationship between L1 DDMA observable and near surface wind speed depends on the degree to which local wind speed has forced the local sea state development. Specifically, in full developed sea conditions, the local wind has had sufficient time and fetch length to influence the surface roughness on all spatial scales and the mean square slope (MSS) of the surface, which is

inversely proportional to σ_o or DDMA, has a particular and well defined relationship with the forcing winds. In young seas with limited fetch length, on the other hand, the longer wavelength portion of the patial roughness spectrum is less well coupled to the local winds and tends to be under developed. This results in a lower MSS and higher DDMA observation for a given wind speed. This bifurcation of the mapping between wind speed and the observable is particularly evident in the young seas conditions typically associated with storms. It is demonstated empirically by the differences between the FDS and YSLF GMFs at higher wind speeds. The DDMA values corresponding to a particular (high) wind speed tend to be lower in the FDS case.

The YSLF GMF is derived using matchups between DDMA observations and HWRF wind speeds during storm overpasses. Wind speed retrievals based on this GMF will, then be appropriate in and near the regions of highest winds. To address the transition zone between high wind/young seas conditions in and near the inner core of storms and lower wind/fully developed conditions far from the storm center, a tapered linear combination of the winds retrieved using the YSLF and FDS GMFs is produced. The taper gives more weight to the FDS retrieval at low wind speeds and more to the YSLF retrieval at high wind speeds. Specifically, the blended YSLF wind speed, u_{YSLF}, is given by

$$u_{YSLF} = \begin{Bmatrix} u_{FDS} & u_{YSLF\_NBRCS} < 0 \\ a u_{FDS} + (1-a) u_{YSLF\_NBRCS} & 0 \le u_{YSLF\_NBRCS} < c \\ u_{YSLF\_NBRCS} & c \le u_{YSLF\_NBRCS} \end{Bmatrix} \tag{5.13}$$

where

$$a = \left(\frac{c - u_{YSLF\_NBRCS}}{c} \right)^d$$

and where u_{FDS} is the FDS MV retrieved wind speed and u_{YSLF_NBRCS} is the wind speed retrieved using the YSLF DDMA GMF. The tapering parameters in eqn. (5.9) are found empirically, by minimizing the RMS difference between the blended YSLF retrieval and matchup HRWF wind speeds, to be c = 80 m/s and d = 3.0. The resulting tapering function, a in eqn. (5.9), is shown in Fig. 33.

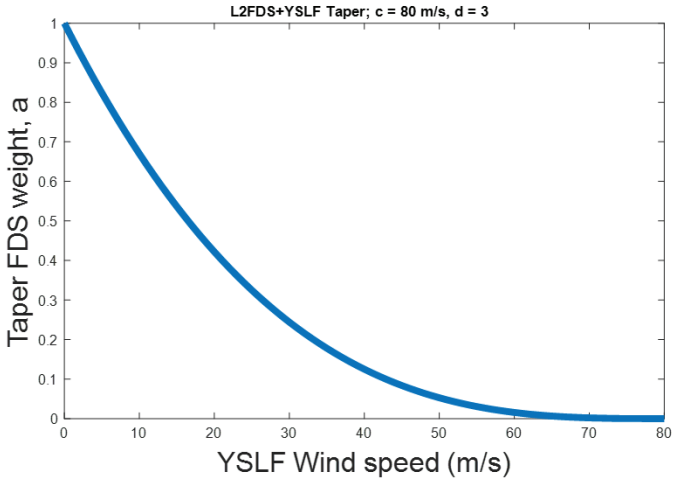

Fig. 33. Weighting given to the FDS retrieved wind in the tapered, blended YSLF retrieval.

5.8 Quality Control Flags in the Retrieval Algorithm

The retrieval algorithm reports a number of quality control (QC) flags associated with each L2 wind speed estimate. Some are designated as “fatal” and indicate that the reported wind speed is either highly non-physical (e.g. a large negative value) or has an estimated uncertainty that is much higher than npormal. Some are designated as “non fatal” and are triggered by anamolous conditions which may affect the accuracy of the estimate. A complete list of the flags is provided in tabular form in Appendix B.

6 References

[Arnold-Bos et al., 2007] A. Arnold-Bos, A. Khenchaf, and A. Martin, "Bistatic radar imaging of the marine environment — Part I: theoretical background," *IEEE Trans. Geosci. Remote Sens.,* vol. 45, no. 11, pp. 3372–3383, Nov 2007.

[Arnold-Bos et al., 2007b] A. Arnold-Bos, A. Khenchaf, and A. Martin, "Bistatic radar imaging of the marine environment — Part II: simulation and result analysis," *IEEE Trans. Geosci. Remote Sens.,* vol. 45, no. 11, pp. 3384–3396, Nov 2007.

[Barrick, 1968] Barrick, D. E., "Relationship between slope probability density function and the physical optics integral in rough surface scattering," *Proc. IEEE*, vol. 56, pp. 1728–1729, 1968.

[Bass and Fuks, 1979] F. G. Bass and I. M. Fuks, *Wave Scattering From Statistically Rough Surfaces*. New York: Pergamon, 1979.

[Brown, 1978] Brown, G.S., "Backscattering from a Gaussian-distributed, perfectly conducting rough surface," *IEEE Trans. Antennas Propag.*, Vol. AP-26, pp. 472–482, May 1978.

[Cardellach and Rius, 2008] Cardellach, E., and A. Rius, "A new technique to sense non-Gaussian features of the sea surface from L-band bistatic GNSS reflections," *Remote Sens. Environ.*, vol. 112, pp. 2927–293, 2008.

[Clarizia et al., 2009] Clarizia, M., Gommenginger, C., Gleason, S., Srokosz, M., Galdi, C., di Bisceglie, M., "Analysis of GNSS-R delay-Doppler maps from the UK-DMC satellite over the ocean", Geophys. Res. Lett. 36, 2009.

[Clarizia, 2012] Clarizia, M. P., "Investigating the Effect of Ocean Waves on GNSS-R Microwave Remote Sensing Measurements", PhD Thesis, University of Southampton, September 2012.

[Clarizia et al., 2013] Clarizia, M.P., Gommenginger C., "Spaceborne GNSS-Reflectometry Instrument and Algorithms: investigating mean square slope retrieval with UK-DMC GNSS-R data", Technical Note, ESTEC contract no. 4000106450/12/NL/FF/LF, August 2013.

[Clarizia et al., 2014] Clarizia, M. P., C. Ruf, C. Gommenginger and P. Jales, "Spaceborne GNSS-R Minimum Variance Wind Speed Estimator", in *IEEE Transactions on Geoscience and Remote Sensing*, vol. 52, no. 11, pp. 6829-6843, 2014.

[Clarizia and Ruf, 2016] Clarizia, M.P., and C. S. Ruf, "Wind Speed Retrieval Algorithm for the Cyclone Global Navigation Satellite System (CYGNSS) Mission," in *IEEE Transactions on Geoscience and Remote Sensing*, vol. 54, no. 8, pp. 4419-4432, 2016, doi: 10.1109/TGRS.2016.2541343.

[Clarizia and Ruf, 2020] M. P. Clarizia and C. S. Ruf, "Statistical Derivation of Wind Speeds From CYGNSS Data," in *IEEE Transactions on Geoscience and Remote Sensing*, vol. 58, no. 6, pp. 3955-3964, June 2020, doi: 10.1109/TGRS.2019.2959715.

[Cox and Munk, 1954] Cox, C., and W. Munk, "Measurement of the roughness of the sea surface from photographs of the Sun's glitter," *J. Opt. Soc. Am.,* Vol. 44, 1954, pp. 835–850.

[Elachi, 1988] Elachi, C., *Spaceborne Radar Remote Sensing: Applications and Techniques*, IEEE Press, New York, 1988.

[Elfouhaily et al., 1997] Elfouhaily, T., Chapron, B., Katsaros, K., Vandemark, D., "A unified directional spectrum for long and short wind-driven waves", Journal of Geophysical Research 102(C7), 15781–15796, 1997.

[Elfouhaily et al., 2002] Elfouhaily T., D.R. Thompson and L. Lindstrom. "Delay-Doppler analysis of bistatically reflected signals from the ocean surface: theory and application," *IEEE Trans. Geosci. Remote Sens.*, vol. 40, No. 3, March 2002.

[Elfouhaily and Guerin, 2004] T. Elfouhaily and C. A. Guérin, "A critical survey of approximate scattering wave theories from random rough surfaces," *Waves Random Media*, vol. 14, pp. R1–R40, 2004.

[Fan et al., 2009] Fan Y., I. Ginis, T. Hara, C.W. Wright, and E. J. Walsh, "Numerical simulations and observations of surface wave fields under an extreme tropical cyclone," *J. Phys. Oceanogr.*, vol. 39, pp. 2097–2116, Sep. 2009.

[Freilich and Challenor, 1994] Freilich M. and P. Challenor, "A New Approach for determining Fully Empirical Altimeter Wind Speed Model Functions", *Journal of Geophysical Research*, Vol. 99, No. C12, December 1994.

[Fung et al., 2001] A. K. Fung, C. Zuffada, and C. Y. Hsieh, "Incoherent bistatic scattering from the sea surface at L band," *IEEE Trans. Geosci. Remote Sens.*, vol. 39, no. 5, pp. 1006–1012, May 2001.

[Garrison et al., 1998] Garrison, J., Katzberg, S., Hill, M., "Effect of sea roughness on bistatically scattered range coded signals from the global positioning system", Geophysical Research Letters 25(13), 2257–2260.

[Garrison et al., 2002] Garrison, J., Komjathy, A., Zavorotny, V., S.J.Katzberg, "Wind speed measurements using forward scattered GPS signals", IEEE Transactions on Geoscience and Remote Sensing 40 (1), 50–65, 2002.

[Germain et al., 2004] Germain, O., Ruffini, G., Soulat, F., Caparrini, M., Chapron, B., Silvestrin, P., "The Eddy experiment: GNSS-R speculometry for directional sea-roughness retrieval from low altitude aircraft" Geophys. Res. Letters 31 (L12306), 2004.

[Gleason et al., 2005] Gleason, S., Hodgart, S., Yiping, S., Gommenginger, C., Mackin, S., Adjrad, M., Unwin, M., "Detection and processing of bistatically reflected GPS signals from Low-Earth Orbit, for the purpose of ocean remote sensing", IEEE Transactions on Geoscience and Remote Sensing 43 (6), 1229–1241, 2005.

[Gleason, 2006] Gleason, S. T., "Remote sensing of ocean, ice and land remote sensing using bistatically scattered GNSS signals from low earth orbit", PhD Thesis, University of Surrey, 2006.

[Gleason et al., 2016] Gleason, S., C., S. Ruf, M. P. Clarizia and A. J. O'Brien, "Calibration and Unwrapping of the Normalized Scattering Cross Section for the Cyclone Global Navigation Satellite System," in *IEEE Transactions on Geoscience and Remote Sensing*, vol. 54, no. 5, pp. 2495-2509, 2016, doi: 10.1109/TGRS.2015.2502245.

[Gleason et al., 2018] Gleason, S., C. S. Ruf, A. O'Brien, D. S. McKague, "The CYGNSS Level 1 Calibration Algorithm and Error Analysis Based On On-Orbit Measurements," IEEE J. Sel. Topics Appl. Earth Obs. Remote Sens., doi: 10.1109/JSTARS.2018.2832981, 2018.

[Guerin et al., 2010] C.-A. Guérin, G. Soriano, and B. Chapron, "The weighted curvature approximation in scattering from sea surfaces," *Waves Random Complex*, vol. 20, no. 3, pp. 364–384, Aug. 2010.

[Johnson, 2005] J. T. Johnson, "A study of ocean-like surface thermal emission and reflection using Voronovich's small slope approximation," *IEEE Trans. Geosci. Remote Sens.*, vol. 43, no. 2, pp. 306–314, Feb. 2005.

[Johnson and Elfouhaily, 2007] Johnson, J.T. and T. M. Elfouhaily, "Computation of oceanlike surface thermal emission and bistatic scattering with the reduced local curvature approximation," *IEEE Trans. Geosci. Remote Sens.*, vol. 45, no. 7, pp. 2108–2115, Jul 2007.

[Katzberg et al., 2000] Katzberg, S. J., J.L. Garrison, "Wind speed retrieval of GPS surface reflection data using a matched filter approach, *paper presented at Sixth International Conference, 2000.*

[Katzberg et al., 2006] Katzberg, S. J., O. Torres, and G. Ganoe, Calibration of reflected GPS for tropical storm wind speed retrievals, *Geophys. Res. Lett.*, 33, L18602, doi:10.1029/2006GL026825, 2006.

[Klein and Swift, 1977] L. A. Klein and C. T. Swift, "An improved model for the dielectric constant of sea water at microwave frequencies," *IEEE Trans. Antennas Propag.*, AP-25(1): pp. 104–11, Jan 1977.

[Komjathy et al., 2004] Komjathy, A., Armatys, M., Masters, D., Axelrad, P., Zavorotny, V., Katzberg, S., "Retrieval of ocean surface wind speed and wind direction using reflected GPS signals", Journal of Atmospheric and Oceanic Technology 21, 515–526, 2004.

[Marchan-Hernandez et al., 2008] Marchan-Hernandez, J., Rodriguez-Alvarez, N., Camps, A., Bosch-Lluis, X., Ramos- Perez, I., Valencia, E., "Correction of the sea state impact in the L-band bright- ness temperature by means of delay-doppler maps of global navigation satellite signals reflected over the sea surface", IEEE Transactions on Geoscience and Remote Sensing 46 (10), 2914–2923, 2008.

[Marchan-Hernandez et al., 2010] Marchan-Hernandez, J., Valencia, E., Rodriguez-Alvarez, N., Ramos-Perez, I., Bosch- Lluis, X., Camps, A., Eugenio, F., Marcello, J., "Sea-state determination using GNSS-R data", IEEE Geoscience and Remote Sensing Letters 7(4), 621–625, 2010.

[Nolan et al., 2013]: David S. Nolan, Robert Atlas, Kieran T. Bhatia, and Lisa R. Bucci, "Development and Validation of a Hurricane Nature Run Using the Joint OSSE Nature Run and the WRF Model", *Journal of Advances in Modeling Earth Systems* (accepted for publication), April 2013.

[O'Brien, 2014] O'Brien, A., "End-to-End Simulator Technical Memo", CYGNSS Technical Document, 2014;

[Parkinson et al., 1996] Parkinson B.W., J.J. Spilker, P. Axelrad, and P. Enge (eds.) *Global Positioning System: Theory and Applications,* Vol. I & II, AIAA, Washington, DC, 1996.

[Rodriguez-Alvarez et al., 2013] Rodriguez-Alvarez, N., D.M. Akos, V.U. Zavorotny, J.A. Smith, A. Camps, and C.W. Fairall, "Airborne GNSS-R wind retrievals using delay-Doppler maps," *IEEE Trans. Geosci. Remote Sens*., vol. 51, no. 1, pp. 626–641, Jan. 2013.

[Ruf, 2013] Ruf, C. S., "DDM Data Compression and Decimation Algorithm", *SPRL Technical Memorandum No. 148-0046-X1*, May 2013.

[Ruf and Balasubramaniam, 2018] Ruf, C., R. Balasubramaniam, "Development of the CYGNSS Geophysical Model Function for Wind Speed," IEEE J. Sel. Topics Appl. Earth Obs. Remote Sens., doi: 10.1109/JSTARS.2018.2833075, 2018.

[Ruf et al., 2018] Ruf, C., S. Gleason, D. S. McKague, "Assessment of CYGNSS Wind Speed Retrieval Uncertainty," IEEE J. Sel. Topics Appl. Earth Obs. Remote Sens., doi: 10.1109/JSTARS.2018.2825948, 2018.

[Soriano and Guerin, 2008] G. Soriano and C-A. Guérin, "A cutoff invariant two-scale model in electromagnetic scattering from sea surfaces," *IEEE Geosci. Remote Sens. Lett*., vol. 5, no. 2, pp. 199-203, Apr 2008.

[Soulat, 2004] Soulat, F., *Sea Surface Remote Sensing With GNSS and Sunlight Reflections*. Ph.D. Thesis. Universitat Politecnica de Catalunya, 2004.

[Thompson et al, 2000] Thompson, D.R., T. M. Elfouhaily, and R. F. Gasparovic, "Polarization dependence of GPS signals reflected from the ocean," In: *Proc. IGARSS'*00, Honolulu, HI, pp. 3099-3101, 2000.

[Thompson et al., 2005] Thompson, D. R., T. M. Elfouhaily, and J. L. Garrison, "An improved geometrical optics model for bistatic GPS scattering from the ocean surface, *IEEE Trans. Geosci. Remote Sens*., vol. 43, No. 12, pp. 2810–2821, 2005.

[Tolman, 1998] Tolman, H. L., "Validation of a new global wave forecast system at NCEP." *Ocean Wave Measurements and Analysis*, B. L. Edge and J. M. Helmsley, Eds., ASCE, pp. 777–786, 1998.

[Valencia et al., 2013] Valencia, E. V. U. Zavorotny, D. M. Akos, and A. Camps, "Using DDM asymmetry metrics for wind direction retrieval from GPS ocean-scattered signals in airborne experiments," *IEEE Trans. Geosci. Remote Sens*., 10.1109/TGRS.2013.2278151, 2014 (in press).

[Voronovich, 1994] Voronovich, A.G., "Small-slope approximation for electromagnetic wave scattering at a rough interface of two dielectric half-spaces," *Waves Random Media,* vol. 4, pp. 337–367, 1994.

[Voronovich, 1999] Voronovich, A.G., *Wave Scattering from Rough Surfaces,* 2nd edn (Berlin: Springer), 236p, 1999.

[Voronovich and Zavorotny, 2001] A. G. Voronovich and V. U. Zavorotny, "Theoretical model for scattering of radar signals from rough sea-surface with breaking waves at Ku- and C-bands," *Waves Random Media*, vol. 11, pp. 247–269, 2001.

[Voronovich and Zavorotny, 2014] Voronovich, A.G., and V. U. Zavorotny, "Full-polarization modeling of monostatic and bistatic radar scattering from a rough sea surface," *IEEE Trans. Antennas Propag*., vol. 62, no. 3, pp. 1362-1371, Mar 2014.

[You et al., 2004] You, H. G. Heckler, J. L. Garrison, and V. U. Zavorotny, Stochastic voltage model and experimental measurement of ocean-scattered GPS signal statistics, *IEEE Trans Geosci. Remote Sens*., vol. 42, No. 10, pp.2160–2169, Oct. 2004.

[You et al., 2006] You, H., J. L. Garrison, G. Heckler, and D. Smajlovic, "The autocorrelation of delay-Doppler waveforms generated from ocean-scattered GPS signals," *IEEE Geosci. Remote Sens. Lett.*, vol. 3(1), pp.78-82, 2006.

[Zavorotny and Voronovich, 2000] Zavorotny, V., Voronovich, A., "Scattering of GPS signals from the ocean with wind remote sensing applications", IEEE Transactions on Geoscience and Remote Sensing 38 (2), 951–964, 2000.

[Zuffada and Zavorotny, 2001] Zuffada, C., and V. Zavorotny, "Coherence time and statistical properties of the GPS signal scattered off the ocean surface and their impact on the accuracy of remote sensing of sea surface topography and winds," In: *Proc. IGARSS'01,* pp. 3332–3334, 2001.

[Zuffada et al., 2004] Zuffada, C., Fung, A., Parker, J., Okolicanyi, M., Huang, E., "Polarization properties of the GPS signal scattered off a wind-driven ocean", IEEE Transactions on Antennas and Propagation 52 (1), 172–187, 2004.

Appendix A: Retrieval Performance Assessment Using On-orbit Observations

A.1. FDS Wind Speed validation and performance characterization

FDS wind speed retrieval performance is assessed by comparing the retrieved wind speed to near-coincident matchup wind speeds by MERRA-2. The matchup population consists of all samples during the period 1 Jan 2019 – 31 Dec 2019 after the removal of samples for which the fatal quality control flags has been set. Fig. A1 shows a scatterplot of the two populations and the RMS and mean difference between them as a function of the MERRA2 wind speed. The statistics are derived using a +/- 0.5 m/s wind speed bin width.

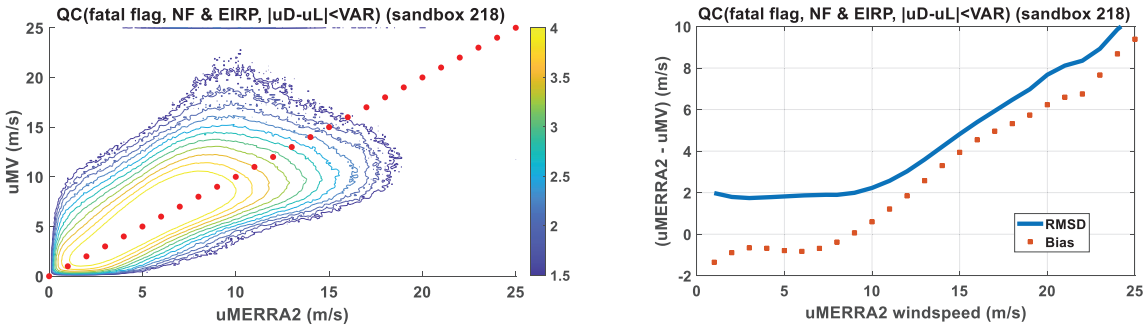

Figure A1. (left) Log(density) scatter plot of groundtruth vs. MV retrieved wind speed along with red dotted line of 1:1 agreement; and (right) RMS and mean retrieval difference vs. groundtruth wind speed.

This matchup population can be partitioned to determine the uncertainty in retrieved wind speed as function of the incidence angle and RCG of the measurement geometry, of the ground truth wind speed, and of the GPS block type. This last partition is used because the quality of the retrieval has been found to vary depending on which model GPS satellite provides the transmitting signal. Research is underway to better characterize the differences between the block types and then to incorporate improved block type-dependent corrections into the Level 1 calibration algorithm. A complete table of wind speed retrieval uncertainities is provided in Appendix B3.

A.2. YSLF Wind Speed validation and performance characterization

The YSLF wind speed product is assessed in two ways. A direct comparison is made between it and near coincident matchups with wind speeds produced by the NOAA HWRF model, using all storm overpasses during August – October 2018. And case studies of individual storm overpasses are examined to consider the physical reasonableness of the imaged storm structure and the uncertainty in the observed storm intensity.

A density scatterplot comparing CYGNSS YSLF winds to near coincident winds modeled by HWRF is shown in Fig. A2. Details concerning assembly of the matchup population are provided in Section 5.1 above. In the figure, there is considerable scatter about the 1:1 line of

perfect agreement evident between the two wind speeds. It results largely from the additive noise that is present in the Level 1 observations from which the Level 2 wind speeds are retrieved. The L1 noise is amplified by the inverse slope of the GMF, which becomes very shallow at higher wind speeds (see Fig. 32 above), when mapped to noise in the L2 wind speed.

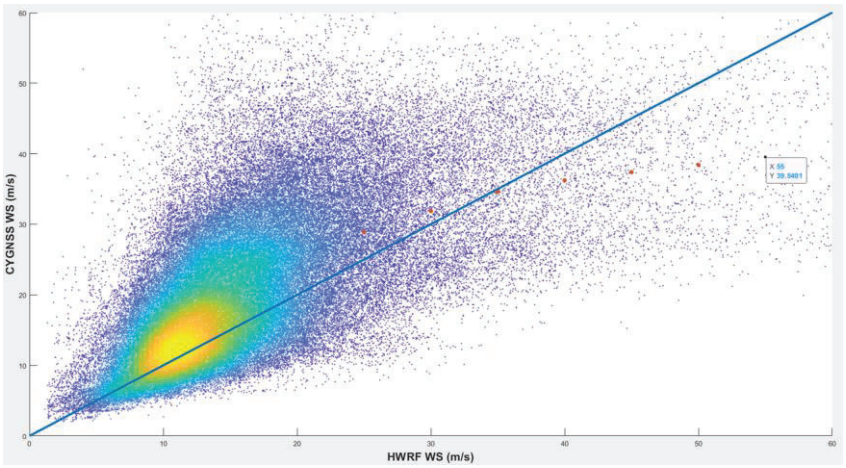

Figure A2. L2 YSLF wind speed vs. HWRF for complete 2018 matchup population.

The effects of noise present in individual L2 wind speed samples can be reduced significantly by binning and averaging of the individual samples in an L3 gridded data product. This is demonstarted in Fig. A3, which shows the L3 gridded wind speed for one-hour of data during overpass of Hurricane Isaias on 2 Aug 2020 at 19:00-20:00 UTC. All measurements made by any of the 8 CYGNSS spacecraft are included, and measurements made in the same 25x25 km^2 grid box are averaged together. Both FDS and YSLF verions of the l3 winds are shown for comparison. They are similar away from the storm center, where the wind speeds are low to moderate. In the inner core of the storm, the FDS wind speed peak intensity is 15-20 m/s whereas the YSLF wind speed, which is more appropriate to use in these conditions, peaks in the 30-35 ms range. By comparison, peak 1-min sustained wind speeds reported on 2 Aug by the National Hurricane Center were in the 28-32 m/s range.

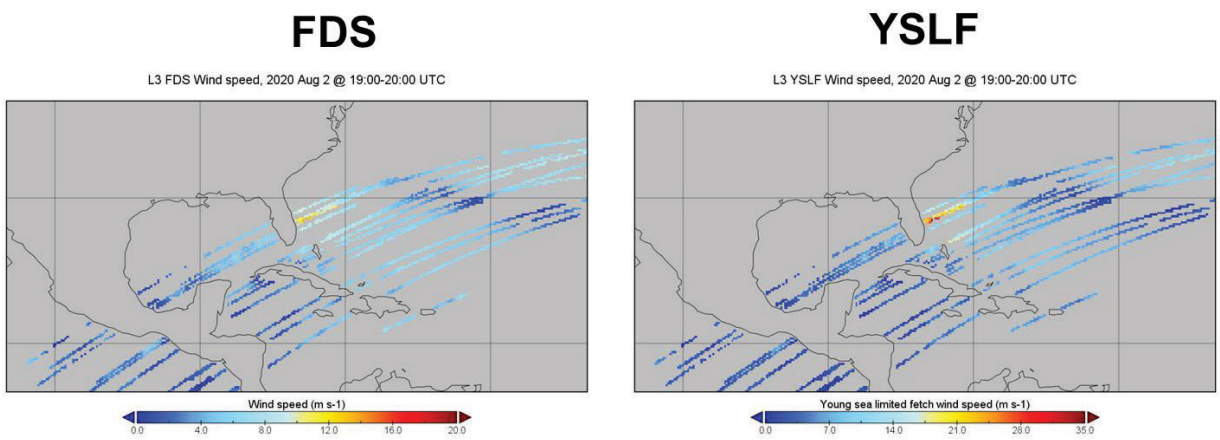

Figure A3. Hurricane Isaias, Standard L3 Gridded Wind Speed, 2 Aug 2020 19:00-20:00 UTC.

A second example of a storm overpass is shown in Fig. A4, of Hurricane Florence on 11 Sep 2018. In this case, a more sophisticated version of the L3 gridded product is used. Whereas Fig. A3 collects all samples made within a one hour window and spatially grids them according to their absolute location, regardless of the time of each sample, Fig. A4 uses a storm centric regridding algorithm and a much wider 6 hour time window. Each sample is located in a relative coordinate system with respect to the time varying location of the storm center. The storm center location is determined from National Hurricane Center best track storm fixes. Storm centric gridding serves two primary purposes. It reducing smearing out of the storm structure due to storm motion during the time window over which the data are assembled. And it allows for wider time windows to be used, which produces images of the storm with less gaps and allows more samples to be averaged together to reduce the effects of L1 measurement noise. Comparing Figs. A3 and A4, the storm features can be seen to be better resolved by the storm centric L3 product.

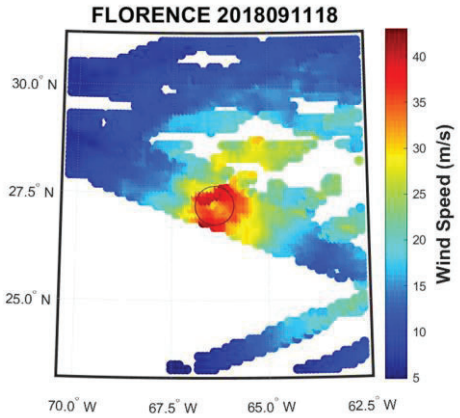

Figure A4. Hurricane Florences, Storm centric L3 gridded wind speed, 11 Sep 2018 15:00-21:00 UTC.

Appendix B: Implementation of On-orbit Wind Speed Rretrieval Algorithm

B.1 Choice of Delay/Doppler Range for Observable Calculation

A very important aspect for the computation of DDMA and LES is the delay and Doppler range, over which the observables are computed. The choice of the delay and Doppler ranges is a trade-off between the improvement in SNR that results from averaging across more of the diffuse scattered signal in the glistening zone, versus the improvement in spatial resolution that results from only averaging over a limited region. The delay and Doppler range depends on the requirement on spatial resolution that one wishes to comply with. For CYGNSS, the baseline requirement on the spatial resolution of the retrieved winds is 25 km x 25 km, ad therefore this is the spatial resolution we focus on. Fig. B1 illustrates two examples of how, for a spatial resolution requirement of 25x25 km, the corresponding delay and Doppler range varies. Note that the iso-range ellipses become closer to each other as the delay increases; furthermore, they widen and stretch out with increasing incidence angles without changing their orientation, so the geometrical parameter that mostly influences the configuration of the iso-delay lines is the incidence angle. In the case of iso-Doppler lines, the spacing between them also increases with increasing incidence angle, but they are also strongly affected by the velocity vectors of the transmitter and above all of the receiver, which change their orientation.

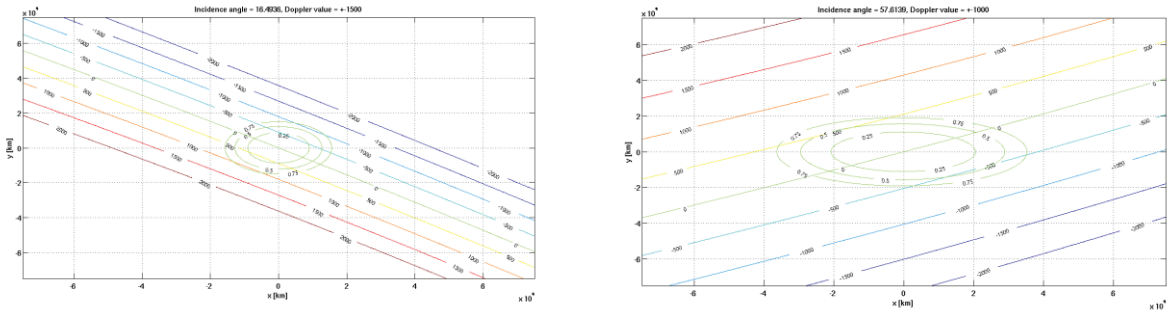

Figure B1. Iso-delay and Iso-Doppler lines for an incidence angle of 16.5° (left) and of 57.6° (right).

Fig. B2 shows curves of the square root of the Instantaneous Field of View (IFOV) versus the incidence angle, for different delay ranges. All the delay ranges considered begin one delay sample before the 0 chip sample to improve the SNR, since the samples adjacent to the specular point one still contain a good amount of the scattered power from the specular point pixel, due to the power spreading caused by the Woodward Ambiguity Function (WAF). The IFOV is defined here as the physical area included in the iso-range ellipse corresponding to a given delay. It is clear from Fig. B2 that for a 25 km x 25 km requirement on the spatial resolution (shown as black continuous line) the only suitable choice is a delay range from -0.25 to 0.25.

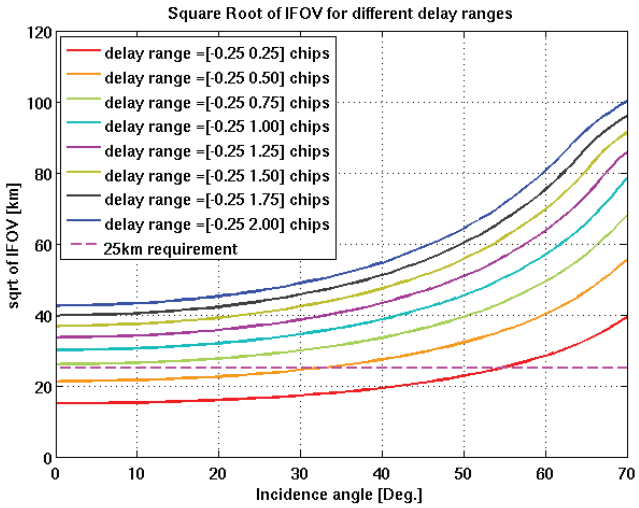

Figure B2. illustration of curves of square root of IFOV versus incidence angle, for a variety of delay ranges. The dashed magenta line shows the 25 km requirement.

Having selected the delay range, the Doppler range has to be chosen such that the iso-Doppler lines will not truncate some of the scattered signal within the iso-delay ellipse at 0.25 chips, but also will not lie too far from the iso-delay ellipse at 0.25 chips and introduce additional noise without adding more signal. Hence, the Doppler range is then chosen to try to satisfy the following two conditions:

- Iso-Doppler lines are the closest possible to the iso-delay line selected
- Iso-Doppler lines are always outside the iso-delay line selected

Since the iso-delay ellipses change depending on geometry, and iso-Doppler lines change their distance to one another and their orientation for different geometries (as shown in Figure B6), the Doppler range that satisfies the above conditions for a given iso-delay line is not unique, and depends on the particular geometry. Furthermore, the Doppler range has an overall much lower influence on the final IFOV, as it is illustrated in Fig. B3, where curves of square root of IFOV versus incidence angle are shown for a single delay range, and a number of different Doppler ranges. It is interesting to observe that the first case of Doppler range of [-250 250] Hz is different from the others, and noisier, since the very small Doppler range chops off part of the area within the iso-delay ellipse at 0.25 chips. Instead, small differences can be observed for the other cases, and mostly at lower incidence angles. This happens because at higher incidence angles, the iso-Doppler lines stretch out more rapidly than the iso-delay lines and tend to fall quickly outside the 0.25 iso-delay ellipse, thus the IFOV for higher incidence angles is entirely determined by the delay range. Furthermore, there is no difference in the IFOV between the [-1000 1000] Hz Doppler range, and the [-1500 1500] Doppler range, suggesting that these iso-Doppler lines fall outside the 0.25 chip iso-Delay lines for all geometries.

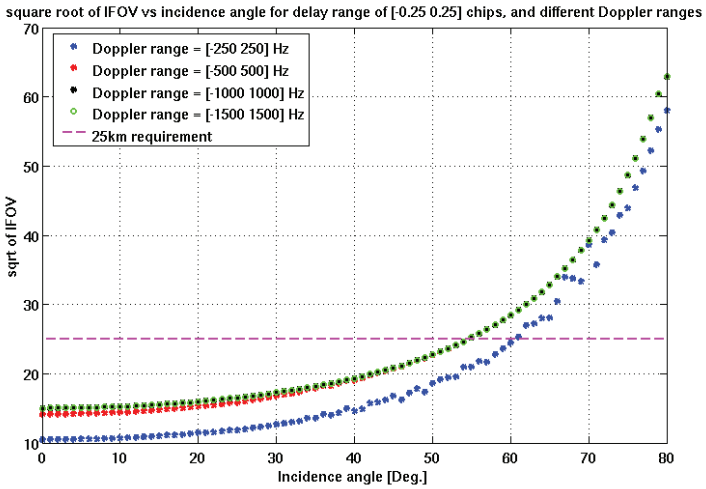

Figure B3. illustration of curves of square root of IFOV versus incidence angle, for a fixed delay range of [-0.25 0.25] chips, and different Doppler ranges. The dashed magenta line shows the 25 km requirement.

Thus, the final choice has been for a Doppler range of [-1000 1000] Hz. This choice has then been confirmed by applying the full L2 retrieval algorithm to DDMA observables computed using the three different Doppler ranges, and by verifying that the Doppler range of [-1000 1000] is the one providing the lowest RMS error among the three

Note that in this case only the physical area included in the iso-delay and iso-Doppler lines is considered. Several additional factors need to be taken into account in order to properly relate the delay and Doppler ranges to the spatial region These include: (1) The spatial boundaries defined by lines of constant iso–delay and iso–Doppler do not conform to a line of constant iso-distance from the specular point. An effective spatial resolution, based, for example, on equal area coverage, needs to be defined; (2) The Woodward ambiguity function and Doppler filter impulse response define weighted response functions for the contribution of different regions of the delay/Doppler domain to the measurements. These weightings should also be accounted for by a suitable definition of the effective spatial resolution; and (3) Multiple samples of the DDM can be averaged together in ground-processing to reduce measurement noise. This will produce spatial smearing in the direction of motion of the specular point. Each of these factors will be included in a more complete definition of the spatial resolution, which is currently under development.

B.2 Derivation of Coefficients for Minimum Variance Estimator

The coefficients to combine wind estimates from different observables to form a minimum variance estimator are given by [Clarizia et al., 2014]

$$\boldsymbol{m} = \left(\sum_{i=1}^{N} \sum_{j=1}^{N} c_{i.j}^{-1} \right)^{-1} \boldsymbol{C}^{-1} \boldsymbol{1} \tag{B.1}$$

where ***1*** is a vector of ones, $\boldsymbol{C}^{-1}$ is the inverse of the covariance matrix between the individual retrieval errors, and $c_{i,j}^{-1}$ are its elements. The variance of the MV estimator is given by

$$\sigma_{MV}^2 = \left(\sum_{i=1}^{N} \sum_{j=1}^{N} c_{i.j}^{-1} \right)^{-1} \tag{B.2}$$

The MV estimator requires knowledge of the covariance matrix of the individual retrieval errors. The covariance is estimated empirically from the retrieval errors, and can be factored into two component matrices, as

$$\boldsymbol{C} = \boldsymbol{SRS} \tag{B.3}$$

where *S* is a diagonal matrix of standard deviations of the retrieval errors for each observable (i.e. the square root of the diagonal elements of the covariance matrix), and *R* is the matrix of correlation coefficients, whose elements are always between -1 and 1.

In practice, the correlation between DDMA and LES retrieval errors varies as a function of the wind speed. For this reason, the covariance matrix assumed by the estimator is varied accordingly, in a manner referred to as Adaptive Covariance (AC). This approach consists of estimating a different covariance matrix, and therefore a different pair of coefficients for the linear combination, for different ranges of estimated wind speed, for which a weighed average of the DDMA and LES retrieved wind speed estimtes (80% DDMA, 20% LES) is used. Using this weighed mean wind speed (WS) in this AC approach, the estimated minimum variance wind speed u_{MV} becomes:

$$u'_{MV} = \boldsymbol{m}^i \cdot \boldsymbol{u}^i \quad WS_{low} < WS < WS_{high} \tag{B.4}$$

where *i* refers to each of the WS intervals used to compute the coefficients in the linear combination, ***m*** is the vector of coefficients defined in (B.1) and ***u*** is the vector of wind speed estimates from DDMA and LES.

The covariance matrices used to compute the best weighted estimate coefficients are derived empirically from the population of retrievals, since neither the individual PDFs of DDMA and LES wind retrieval errors nor the joint PDF between the two retrieval errors are available in analytical form. The bias between true and retrieved winds is first computed for each observable, and for each WS interval, and removed, so as to compute the coefficients from unbiased DDMA and LES wind estimates. The coefficients ***m*** as well as the bias are calculated from a training

dataset where the true wind speeds are known, and then used in the test dataset, where the wind speeds are not known, to assess algorithm performance. This means that the coefficients may be suboptimal when applied to the test dataset, but we expect the performance to be asymptotically optimal for increasing number of observations, and assuming that the statistical properties of the training dataset are the same as those of the test dataset.

B.2.1 Minimum Variance Coefficients LUT

The coefficients used to combine the DDMA and LES wind estimates to obtain the final estimated wind are shown in Figure B4 as a function of the weighted mean DDMA/LES wind speed. These coefficients are derived from error covariance analysis based on the 2019 matchups between CYGNSS MV retrievals and MERRA-2 wnds.

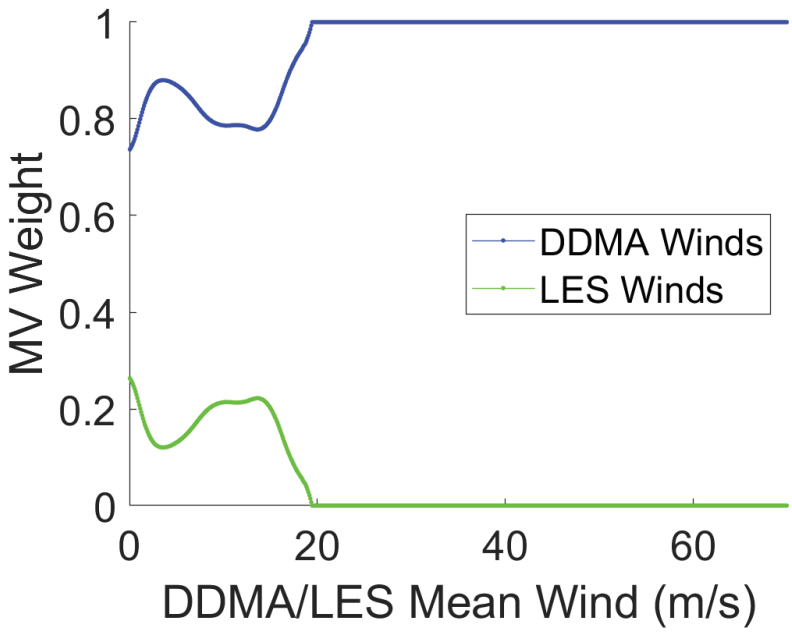

Figure B4. Minimum Covariance coefficients used to optimally combine DDMA and LES winds to form the minimum covariance wind speed estimate based on the weighted mean of the DDMA and LES winds (80% DDMA/20% LES). Coefficients were computed separately in .1 m/s intervals of mean DDMA, LES winds.

B.3 Debiasing Maps

Wind speed CDF matching debiasing is done separately for each antenna (starboard and port) of each FM as a function of incidence angle, azimuth angle, and commanded roll state, with .1 deg resolution in azimuth and incidence angles and .1 m/s resultion in wind speed. This is done sperately for DDMA and LES wind speeds, which are combined to comute the minimum variance wind, which itself is debiased for the final wind speed estimate. Maps are based on the 2019 matchups between CYGNSS retrievals and MERRA-2 winds. Example maps are shown in Figure

B5 for the DMA and LES winds and in Figure B6 for the MV winds. CDF-matched winds which lie along the 45° "one-to-one" line represent wind speed ranges where the probability distributions already match well and no adjustment is needed. Coefficients above and below the 1:1 line represent remappings where a range of retrieved wind speeds is compressed or expanded to more closely match the likelihood of occurrence of the MERRA-2 wind speed for the same wind speed interval.

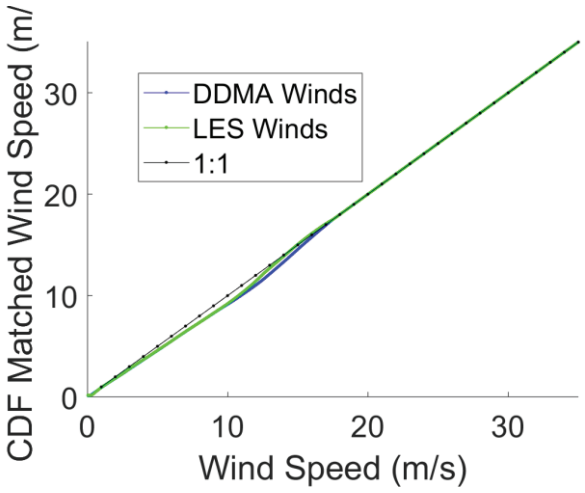

Figure B5. DDMA and LES wind debiasing maps used to match the global probability distribution of CYGNSS L2 fully developed seas minimum variance wind speeds to those of the MERRA-2 reanalysis numerical weather prediction product. This example is for the starboard antenna of FM1 at an incidence angle of 28 degrees (location of peak gain) and a commanded roll state of -22 degrees. Maps for other FM, roll states, incidence angles, and azimuth angles are similar.

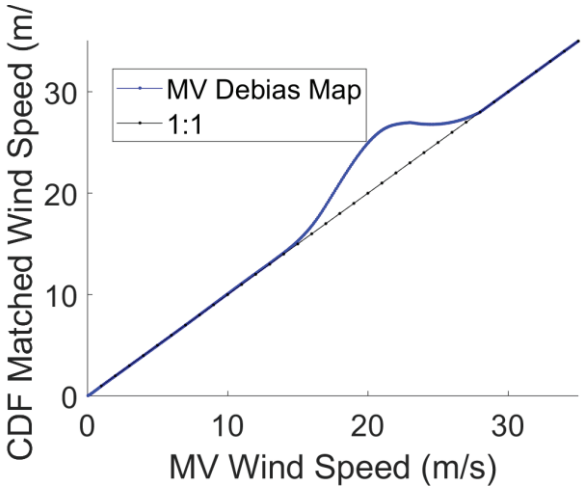

Figure B6. MV wind debiasing map used to match the global probability distribution of CYGNSS L2 fully developed seas minimum variance wind speeds to those of the MERRA-2 reanalysis numerical weather prediction product.

B.4 Time-averaging LUT

The time-averaging LUT contains the number of samples to time-average as a function of incidence angle. The incidence angle axis is defined as going from 0° to 89°, with a step of 1 °. Values are reported in Table B2 for specific incidence angle intervals.

Number of samples to time-average	Incidence angle interval [°]
5	$0° < \theta \leq 17°$
4	$17° < \theta \leq 31°$
3	$31° < \theta \leq 41°$
2	$41° < \theta \leq 48°$
1	$\theta > 48°$

Table B2. Number of samples to time-average as a function of incidence angle

B.5 Standard Deviation of the retrieval error LUT

The standard deviation of the error in the retrieved wind, associated with each GPS Block type, RCG, incidence angle, and wind speed interval, is reported in Tables B3. The values are empirically derived from statistical comparisons between retrieved winds and matchup ground truth winds provided by MERRA-2 (for the FDS MV retrievals) and by HWRF (for the YSLF retrievals at the higher wind speed intervals).

Table B3.1. Standard Deviation of FDS MV wind speed retrieval error

BLOCK IIA (SVN = 34)

Minimum Variance Wind Speed Range	Incidence angle ≤ 10 deg		
	RCG ≤ 10	10 < RCG ≤ 60	60 < RCG
$0 < u_{MV} \leq 5$ m/s	**2.0**	**1.5**	**1.5**
$5 < u_{MV} \leq 10$ m/s	**2.0**	**1.5**	**1.5**
$10 < u_{MV} \leq 15$ m/s	**4.0**	**3.5**	**3.0**
$15 < u_{MV} \leq 20$ m/s	**7.0**	**6.0**	**5.0**
$20 \text{ m/s} < u_{MV}$	**8.0**	**7.0**	**7.0**

Minimum Variance Wind Speed Range	10 deg < Incidence angle ≤ 60 deg		
	RCG ≤ 10	10 < RCG ≤ 60	60 < RCG
$0 < u_{MV} \leq 5$ m/s	**1.5**	**1.5**	**1.5**
$5 < u_{MV} \leq 10$ m/s	**1.5**	**1.5**	**1.5**
$10 < u_{MV} \leq 15$ m/s	**3.5**	**3.0**	**3.0**
$15 < u_{MV} \leq 20$ m/s	**7.0**	**6.0**	**5.0**
20 m/s < u_{MV}	**8.0**	**7.0**	**6.5**

Minimum Variance Wind Speed Range	60 deg < Incidence angle		
	RCG ≤ 10	10 < RCG ≤ 60	60 < RCG
$0 < u_{MV} \leq 5$ m/s	**1.5**	**1.5**	**1.5**
$5 < u_{MV} \leq 10$ m/s	**1.5**	**1.5**	**1.5**
$10 < u_{MV} \leq 15$ m/s	**4.0**	**3.0**	**3.0**
$15 < u_{MV} \leq 20$ m/s	**7.0**	**6.0**	**5.0**
20 m/s < u_{MV}	**8.0**	**7.0**	**7.0**

BLOCK IIR-Legacy (SVN = 41, 43, 44, 45, 46, 51, 54, 56)

Minimum Variance Wind Speed Range	Incidence angle ≤ 10 deg		
	RCG ≤ 10	10 < RCG ≤ 60	60 < RCG
$0 < u_{MV} \leq 5$ m/s	**2.0**	**1.5**	**1.5**
$5 < u_{MV} \leq 10$ m/s	**2.5**	**2.0**	**1.5**
$10 < u_{MV} \leq 15$ m/s	**5.0**	**4.0**	**3.0**
$15 < u_{MV} \leq 20$ m/s	**7.0**	**7.0**	**6.0**
20 m/s < u_{MV}	**9.0**	**9.0**	**8.0**

Minimum Variance Wind Speed Range	10 deg < Incidence angle ≤ 60 deg		
	RCG ≤ 10	10 < RCG ≤ 60	60 < RCG
$0 < u_{MV} \leq 5$ m/s	**1.5**	**1.5**	**1.5**
$5 < u_{MV} \leq 10$ m/s	**1.5**	**1.5**	**1.5**

$10 < u_{MV} \leq 15$ m/s	**3.5**	**3.0**	**2.5**
$15 < u_{MV} \leq 20$ m/s	**7.0**	**6.0**	**5.5**
20 m/s $< u_{MV}$	**8.0**	**7.5**	**7.0**

Minimum Variance Wind Speed Range	60 deg < Incidence angle		
	RCG ≤ 10	10 < RCG ≤ 60	60 < RCG
$0 < u_{MV} \leq 5$ m/s	**1.5**	**1.5**	**1.5**
$5 < u_{MV} \leq 10$ m/s	**1.5**	**1.5**	**1.5**
$10 < u_{MV} \leq 15$ m/s	**3.5**	**3.0**	**3.0**
$15 < u_{MV} \leq 20$ m/s	**7.0**	**6.0**	**6.0**
20 m/s $< u_{MV}$	**8.0**	**8.0**	**7.0**

BLOCK IIR Improved (SVN = 47, 59, 60, 61)

Minimum Variance Wind Speed Range	Incidence angle ≤ 10 deg		
	RCG ≤ 10	10 < RCG ≤ 60	60 < RCG
$0 < u_{MV} \leq 5$ m/s	**1.5**	**1.5**	**1.5**
$5 < u_{MV} \leq 10$ m/s	**1.5**	**1.5**	**1.5**
$10 < u_{MV} \leq 15$ m/s	**3.5**	**3.0**	**2.5**
$15 < u_{MV} \leq 20$ m/s	**7.0**	**6.0**	**5.0**
20 m/s $< u_{MV}$	**9.0**	**8.0**	**7.0**

Minimum Variance Wind Speed Range	10 deg < Incidence angle ≤ 60 deg		
	RCG ≤ 10	10 < RCG ≤ 60	60 < RCG
$0 < u_{MV} \leq 5$ m/s	**1.5**	**1.5**	**1.5**
$5 < u_{MV} \leq 10$ m/s	**1.5**	**1.5**	**1.5**
$10 < u_{MV} \leq 15$ m/s	**3.0**	**3.0**	**2.5**
$15 < u_{MV} \leq 20$ m/s	**6.0**	**5.0**	**4.5**
20 m/s $< u_{MV}$	**9.0**	**8.0**	**7.0**

Minimum Variance Wind Speed Range	60 deg < Incidence angle		
	RCG ≤ 10	10 < RCG ≤ 60	60 < RCG
$0 < u_{MV} \leq 5$ m/s	**1.5**	**1.5**	**1.5**
$5 < u_{MV} \leq 10$ m/s	**1.5**	**1.5**	**1.5**
$10 < u_{MV} \leq 15$ m/s	**3.0**	**3.0**	**2.5**
$15 < u_{MV} \leq 20$ m/s	**6.0**	**5.5**	**5.0**
20 m/s < u_{MV}	**9.0**	**8.0**	**7.0**

BLOCK IIR-M (SVN = 48, 50, 52, 53, 55, 57, 58)

Minimum Variance Wind Speed Range	Incidence angle ≤ 10 deg		
	RCG ≤ 10	10 < RCG ≤ 60	60 < RCG
$0 < u_{MV} \leq 5$ m/s	**1.5**	**1.5**	**1.5**
$5 < u_{MV} \leq 10$ m/s	**1.5**	**1.5**	**1.5**
$10 < u_{MV} \leq 15$ m/s	**3.0**	**2.5**	**2.5**
$15 < u_{MV} \leq 20$ m/s	**5.5**	**4.5**	**4.0**
20 m/s < u_{MV}	**9.0**	**8.0**	**7.0**

Minimum Variance Wind Speed Range	10 deg < Incidence angle ≤ 60 deg		
	RCG ≤ 10	10 < RCG ≤ 60	60 < RCG
$0 < u_{MV} \leq 5$ m/s	**1.5**	**1.5**	**1.5**
$5 < u_{MV} \leq 10$ m/s	**1.5**	**1.5**	**1.5**
$10 < u_{MV} \leq 15$ m/s	**3.0**	**2.5**	**2.5**
$15 < u_{MV} \leq 20$ m/s	**5.0**	**4.5**	**4.0**
20 m/s < u_{MV}	**7.5**	**6.5**	**6.0**

Minimum Variance Wind Speed Range	60 deg < Incidence angle		
	RCG ≤ 10	10 < RCG ≤ 60	60 < RCG
$0 < u_{MV} \leq 5$ m/s	**1.5**	**1.5**	**1.5**
$5 < u_{MV} \leq 10$ m/s	**1.5**	**1.5**	**1.5**

$10 < u_{MV} \leq 15$ m/s	**3.0**	**2.5**	**2.5**
$15 < u_{MV} \leq 20$ m/s	**6.5**	**5.5**	**5.0**
20 m/s $< u_{MV}$	**8.5**	**8.0**	**7.0**

BLOCK IIF (SVN = 62, 63, 64, 65, 66, 67, 68, 69, 70, 71, 72, 73)

Minimum Variance Wind Speed Range	Incidence angle ≤ 10 deg		
	RCG ≤ 10	10 < RCG ≤ 60	60 < RCG
$0 < u_{MV} \leq 5$ m/s	**1.5**	**1.5**	**1.5**
$5 < u_{MV} \leq 10$ m/s	**1,5**	**1.5**	**1.5**
$10 < u_{MV} \leq 15$ m/s	**3.0**	**3.0**	**2.5**
$15 < u_{MV} \leq 20$ m/s	**6.0**	**5.5**	**5.0**
20 m/s $< u_{MV}$	**9.0**	**8.0**	**7.0**

Minimum Variance Wind Speed Range	10 deg < Incidence angle ≤ 60 deg		
	RCG ≤ 10	10 < RCG ≤ 60	60 < RCG
$0 < u_{MV} \leq 5$ m/s	**1.5**	**1.5**	**1.5**
$5 < u_{MV} \leq 10$ m/s	**1.5**	**1.5**	**1.5**
$10 < u_{MV} \leq 15$ m/s	**3.0**	**3.0**	**2.5**
$15 < u_{MV} \leq 20$ m/s	**5.5**	**5.0**	**5.0**
20 m/s $< u_{MV}$	**9.0**	**8.0**	**7.0**

Minimum Variance Wind Speed Range	60 deg < Incidence angle		
	RCG ≤ 10	10 < RCG ≤ 60	60 < RCG
$0 < u_{MV} \leq 5$ m/s	**1.5**	**1.5**	**1.5**
$5 < u_{MV} \leq 10$ m/s	**1.5**	**1.5**	**1.5**
$10 < u_{MV} \leq 15$ m/s	**3.0**	**3.0**	**2.0**
$15 < u_{MV} \leq 20$ m/s	**7.0**	**6.0**	**5.0**
20 m/s $< u_{MV}$	**9.0**	**8.0**	**7.0**

BLOCK III (SVN = 74, 75)

Minimum Variance Wind Speed Range	Incidence angle ≤ 10 deg		
	RCG ≤ 10	10 < RCG ≤ 60	60 < RCG
$0 < u_{MV} \leq 5$ m/s	**1.5**	**1.5**	**1.5**
$5 < u_{MV} \leq 10$ m/s	**1.5**	**1.5**	**1.5**
$10 < u_{MV} \leq 15$ m/s	**4.0**	**3.0**	**2.5**
$15 < u_{MV} \leq 20$ m/s	**7.0**	**6.0**	**5.0**
20 m/s < u_{MV}	**9.0**	**8.0**	**7.0**

Minimum Variance Wind Speed Range	10 deg < Incidence angle ≤ 60 deg		
	RCG ≤ 10	10 < RCG ≤ 60	60 < RCG
$0 < u_{MV} \leq 5$ m/s	**1.5**	**1.5**	**1.5**
$5 < u_{MV} \leq 10$ m/s	**1.5**	**1.5**	**1.5**
$10 < u_{MV} \leq 15$ m/s	**3.0**	**2.5**	**2.5**
$15 < u_{MV} \leq 20$ m/s	**7.0**	**6.0**	**5.0**
20 m/s < u_{MV}	**9.0**	**8.0**	**7.0**

Minimum Variance Wind Speed Range	60 deg < Incidence angle		
	RCG ≤ 10	10 < RCG ≤ 60	60 < RCG
$0 < u_{MV} \leq 5$ m/s	**1.5**	**1.5**	**1.5**
$5 < u_{MV} \leq 10$ m/s	**1.5**	**1.5**	**1.5**
$10 < u_{MV} \leq 15$ m/s	**4.0**	**4.0**	**3.0**
$15 < u_{MV} \leq 20$ m/s	**7.0**	**6.0**	**5.0**
20 m/s < u_{MV}	**9.0**	**8.0**	**7.0**

Table B3.2. Standard Deviation of YSLF wind speed retrieval error

YSLF Wind Speed Range	Incidence angle ≤ 10 deg		
	RCG ≤ 3	3 < RCG ≤ 30	30 < RCG
$0 < u_{YSLF} \leq 10$ m/s	**3.0**	**3.0**	**3.0**

$10 < u_{YSLF} \leq 20$ m/s	**3.5**	**3.5**	**3.5**
$20 < u_{YSLF} \leq 60$ m/s	**6.0**	**6.0**	**5.0**
60 m/s $< u_{YSLF}$	**9.0**	**8.0**	**7.0**

YSLF Wind Speed Range	10 < Incidence angle ≤ 60 deg		
	RCG ≤ 3	3 < RCG ≤ 30	30 < RCG
$0 < u_{YSLF} \leq 10$ m/s	**2.5**	**2.5**	**2.5**
$10 < u_{YSLF} \leq 20$ m/s	**3.0**	**3.0**	**3.0**
$20 < u_{YSLF} \leq 60$ m/s	**6.0**	**5.0**	**4.0**
60 m/s $< u_{YSLF}$	**8.0**	**7.0**	**6.0**

YSLF Wind Speed Range	60 deg < Incidence angle		
	RCG ≤ 3	3 < RCG ≤ 30	30 < RCG
$0 < u_{YSLF} \leq 10$ m/s	**3.0**	**3.0**	**3.0**
$10 < u_{YSLF} \leq 20$ m/s	**3.5**	**3.5**	**3.5**
$20 < u_{YSLF} \leq 60$ m/s	**7.0**	**6.0**	**5.0**
60 m/s $< u_{YSLF}$	**9.0**	**8.0**	**8.0**

B.6 L2 Data Dictionary

Table B4 lists all the variables in the Level 2 wind speed NetCDF files.

Name	Long Name	netCDF Type	CF Conventions Units	netCDF Dimensions	Comment
Global Values					
time_coverage_start	<none>	file attribute, string	<none>	<none>	sample_time of the first sample in the file in ISO-8601 form
time_coverage_end	<none>	file attribute, string	<none>	<none>	sample_time of the last sample in the file in ISO-8601 form
time_coverage_duration	<none>	file attribute, string	<none>	<none>	The time interval between test_coverage_start and test_coverage_end in ISO1806 form
time_coverage_resolution	<none>	file attribute, string	<none>	<none>	The nominal time interval between samples in ISO1806 form

ddm_source	Level 0 data source	byte	<none>	<none>	The source of the Level 0 DDM raw counts and metadata utilized to derive wind_speed. 0 = E2ES (CYGNSS end-to-end simulator) 1 = GPS signal simulator 2 = CYGNSS spacecraft 3 = Source Unknown
time_averaging_lookup_tables_version	<none>	file attribute, string	<none>	<none>	The GMF time-averaging lookup table version number.
nbrcs_wind_lookup_tables_version	<none>	file attribute, string	<none>	<none>	The GMF NBRCS to wind speed lookup table version number.
les_wind_lookup_tables_version	<none>	file attribute, string	<none>	<none>	The GMF LES to wind speed lookup table version number.
covariance_lookup_tables_version	<none>	file attribute, string	<none>	<none>	The GMF minimum covariance lookup table version number.
standard_deviation_lookup_table_version	<none>	file attribute, string	<none>	<none>	The GMF standard deviation lookup table version number.

l2_algorithm_version	<none>	file attribute, string	<none>	<none>	L2 processing algorithm version number.
source	<none>	file attribute, string	<none>	<none>	Level 1 netCDF source file names.
Per-Sample Values					
spacecraft_id	CCSDS spacecraft identifier	short	1	sample	The CCSDS spacecraft identifier: 0xF7 (247): CYGNSS 1 0xF9 (249): CYGNSS 2 0x2B (43): CYGNSS 3 0x2C (44): CYGNSS 4 0x2F (47): CYGNSS 5 0x36 (54): CYGNSS 6 0x37 (55): CYGNSS 7 0x49 (73): CYGNSS 8 0x00 (0): E2ES 0x0E (14): engineering model 0x0D (15): default 0xFF (255): unknown
spacecraft_num	CYGNSS spacecraft number	byte	1	sample	The CYGNSS spacecraft number: Ranges from 1 through 8 and 99. 1 through 8 are on-orbit spacecraft. 99 is the CYGNSS end-to-end simulator.

prn_code	GPS PRN code	byte	1	sample	The PRN code of the GPS signal associated with the DDMs utilized to derive wind_speed. Ranges from 0 to 32. 0 = reflectometry channel idle. 1 to 32 represents PRN code.
sv_num	GPS space vehicle number	short	1	sample	The GPS unique space vehicle number that transmitted prn_code.
Antenna	Receive antenna	byte	<none>	sample	The CYGNSS nadir antenna that received the reflected GPS signal associated with the DDMs utilized to derive wind_speed. 0 = none 1 = zenith (never used) 2 = nadir_starboard 3 = nadir_port
sample_time	Sample time	double	seconds since time_coverage_ start	sample	The mean of ddm_timestamp_utc of the DDMs that were utilized to derive wind_speed. Note that the DDM sampling period is not synchronized with the UTC change of second so sample_time can occur at any time relative to the UTC change of second.
Lat	Latitude	float	degrees_north	sample	The mean of the specular point latitudes of the DDMs that were utilized to derive wind_speed, degrees North.

Lon	Longitude	float	degrees_east	sample	The mean of the specular point longitudes of the DDMs that were utilized to derive wind_speed, degrees East.
sc_lat	Subsatellite point latitude	float	degrees_north	sample	The mean of the subsatellite point latitudes of the DDMs that were utilized to derive wind_speed, degrees North.
sc_lon	Subsatellite point longitude	float	degrees_east	sample	The mean of the subsatellite point longitudes of the DDMs that were utilized to derive wind_speed, degrees East.
sc_alt	Spacecraft altitude	int	meter	sample	The mean of the satellite altitudes above the WGS-84 ellipsoid of the DDMs that were utilized to derive wind_speed, meters.

wind_speed	Retrieved wind speed using Minimum Variance estimator applied to Fully Developed Seas retrievals from NBRCS and LES	float	m s-1	sample	The average surface wind speed of the 25 x 25 km cell centered on lat and lon derived from both the NBRCS and the LES observables using the fully developed seas geophysical model function, m/s. Multiple DDMs are utilized to derive wind_speed. The number of utilized DDMs ranges from 1 to 5.
fds_nbrcs_wind_speed	Fully Developed Sea retrieval of wind speed from NBRCS	float	m s-1	sample	The average surface wind speed of the 25 x 25 km cell centered on lat and lon derived only from the NBRCS observable using the fully developed seas geophysical model function, m/s. Multiple DDMs are utilized to derive fds_nbrcs_wind_speed. The number of DDMs ranges from 1 to 5.
fds_les_wind_speed	Fully Developed Seas retrieval of wind speed from LES	float	m s-1	sample	The average surface wind speed of the 25 x 25 km cell centered on lat and lon derived only from the LES observable using the fully developed seas geophysical model function, m/s. Multiple DDMs are utilized to derive

					fds_les_wind_speed. The number of DDMs ranges from 1 to 5.
wind_speed_uncertainty	Uncertainty in MV FDS wind speed	float	m s-1	sample	Standard deviation of the additive wind speed error in the minimum variance fully developed seas wind speed (wind_speed) retrieval (dependent on the RCG of the specular point location and the wind speed), in m/s.
yslf_nbrcs_high_wind_speed	Young Seas/Limited Fetch retrieval of wind speed from NBRCS	float	m s-1	sample	The surface wind speed centered on lat and lon derived from the NBRCS observable using the young seas/limited fetch geophysical model function, m/s. Retrieval is only considered accurate at high wind speeds. Multiple DDMs are utilized to derive wind_speed. The number of utilized DDMs ranges from 1 to 5.

yslf_wind_speed	Retrieved wind speed using blended FDS MV (at low winds) and YSLF NBRCS (at high winds) retrievals.	float	m s-1	sample	The surface wind speed centered on lat and lon derived as a tapered linear combination of the FDS MV and YSLF NBRCS retrieved winds according to: yslf_wind_speed = a*wind_speed + (1 - a)*yslf_nbrcs_high_wind_speed, where a=((80 - yslf_nbrcs_high_wind_speed)/80)^3 if 0<=yslf_nbrcs_high_wind_speed<80, a=1 if yslf_nbrcs_high_wind_speed<0, a=0 if 80<=yslf_nbrcs_high_wind_speed.
yslf_wind_speed_uncertainty	Uncertainty in YSLF wind speed	float	m s-1	sample	Standard deviation of the additive wind speed error in yslf_wind_speed (dependent on the RCG of the specular point location and the wind speed), in m/s.
mean_square_slope	Mean square slope	float	1	sample	The average MSS of the 25 x 25 km cell centered on lat and lon, unitless.
mean_square_slope_uncertainty	Mean square slope uncertainty	float	1	sample	The uncertainty of mean_square_slope, unitless.
incidence_angle	Incidence angle	float	degree	sample	The mean of the incidence angles of the specular points of the DDMs that

					were utilized to derive wind_speed, degrees.
azimuth_angle	Azimuth angle	float	degree	sample	The mean of the orbit frame azimuth angles of the specular points of the DDMs that were utilized to derive wind_speed, degrees.
sc_roll	Spacecraft attitude roll angle	float	radian	sample	The mean of the spacecraft roll angle relative to the orbit frame for all the DDMS utilized to dervie wind_speed, radians
commanded_sc_roll	Commanded spacecraft attitude roll angle	float	radian	sample	Commanded spacecraft attitude roll angle, in radians at ddm_timestamp_utc.
nbrcs_mean	NBRCS mean	float	1	sample	The mean of the DDM NBRCS values that were utilized to derive wind_speed, unitless.
les_mean	LES mean	float	1	sample	The mean of the DDM LES values that were utilized to derive wind_speed, unitless.
range_corr_gain	Range corrected gain	float	1e-27 dBi meter-4	sample	The mean of the RCGs of the DDMs that were utilized to produce wind_speed. Individual RCGs are equal to the receive antenna gain in the direction of the specular point multiplied by 1e27 divided by the square of the receiver to the specular

					point range and the square of the transmitter to specular point range. Units: 1e27 *dBi * m^-4
fresnel_coeff	Fresnel power reflection coefficient	float	1	sample	The square of the left hand circularly polarized Fresnel electromagnetic voltage reflection coefficient at 1575 MHz for a smooth ocean surface at lat, lon. See UM document 148-0361 for a description of the calculation of the Fresnel coefficient, unitless.
num_ddms_utilized	Number of DDM utilized	byte	1	sample	The number of DDMs averaged together to produce wind_speed. The number of DDMs utilized depends on the incidence angle. Ranges from 1 to 5.
sample_flags	General status flags for the sample	short	<none>	sample	Set of flags indicating general conditions for the sample, set to 1 if condition is true. Flag bit masks: 1 (Bit 1) = spare_1, always zero

fds_sample_flags	Sample status flags for Fully Developed Seas wind speed retreval	short	<none>	sample	Set of FDS status flags, set to 1 if condition is true. Flag bit masks: 1 (Bit 1) = fatal_composite_wind_speed_flag, logical OR of fatal FDS flags (fatal_neg_wind_speed OR fatal_neg_fds_nbrcs_wind_speed OR fatal_neg_fds_les_wind_speed OR fatal_high_wind_speed OR fatal_high_fds_nbrcs_wind_speed OR fatal_high_fds_les_wind_speed OR fatal_retrieval_ambiguity OR fatal_single_observable OR fatal_low_range_corr_gain OR fatal_fds_noise_floor OR fatal_fds_gps_eirp) 2 (Bit 2) = spare_2, always zero 4 (Bit 3) = spare_3, always zero 8 (Bit 4) = spare_4, always zero 16 (Bit 5) = fatal_neg_wind_speed, wind_speed <= 0 m/s 32 (Bit 6) = fatal_neg_fds_nbrcs_wind_speed, fds_nbrcs_wind_speed <= 0 m/s
					64 (Bit 7) = fatal_neg_fds_les_wind_speed, fds_les_wind_speed <= 0 m/s 128 (Bit 8) = fatal_high_wind_speed, fatal_high_fds_nbrcs_wind_speed or fatal_high_fds_les_wind_speed are

					one 256 (Bit 9) = fatal_high_fds_nbrcs_wind_speed, fds_nbrcs_wind_speed >= 40 m/s 512 (Bit 10) = fatal_high_fds_les_wind_speed, fds_les_wind_speed >= 30 m/s
					1024 (Bit 11) = non_fatal_ascending, satellite is on the ascending node of the orbit (subsatellite point latitude is increasing) 2048 (Bit 12) = fatal_retrieval_ambiguity, wind_speed was derived from both fds_nbrcs_wind_speed and fds_les_wind_speed AND if wind_speed <= 6 m/s then |fds_nbrcs_wind_speed - fds_les_wind_speed| >= 2 else |fds_nbrcs_wind_speed - fds_les_wind_speed| >= 2 + 0.04*((wind_speed - 6)^1.75) 4096 (Bit 13) = fatal_single_observable, wind_speed was derived from a single observable, either fds_nbrcs_wind_speed or fds_les_wind_speed, but not both 8192 (Bit 14) = fatal_low_range_corr_gain,

					range_corr_gain < 1 16384 (Bit 15) = spare_5, always false. 32768 (Bit 16) = fatal_fds_noise_floor, the gain corrected noise floor is outside of the valid range 0.5 through 1.4 Watts 10.e+17.
					65536 (Bit 17) = fatal_fds_gps_eirp, the EIRP is outside of the valid range (range varies with GPS block type).

yslf_sample_flags	Sample status flags for Young Seas/Limited Fetch wind speed retreval	short	<none>	sample	Set of YSLF status flags, set to 1 if condition is true. Flag bit masks: 1 (Bit 1) = fatal_composite_yslf_wind_speed, logical OR of fatal FDS and YSLF flags (fatal_composite_wind_speed_flag OR fatal_high_yslf_nbrcs_wind_speed OR fatal_low_range_corr_gain OR fatal_yslf_noise_floor) 2 (Bit 2) = spare_6, always zero 4 (Bit 3) = spare_7, always zero 8 (Bit 4) = spare_8, always zero 16 (Bit 5) = non_fatal_neg_yslf_nbrcs_high_wind_speed, yslf_nbrcs_high_wind_speed <= -5 m/s 32 (Bit 6) = spare 9, always zero
					64 (Bit 7) = spare_10, always zero 128 (Bit 8) = spare_11, always zero 256 (Bit 9) = fatal_high_yslf_nbrcs_wind_speed, nbrcs_mean corresponds to a YSLF wind speed >= 99.9 m/s 512 (Bit 10) = spare_12, always zero

					1024 (Bit 11) = non_fatal_ascending, satellite is on the ascending node of the orbit (subsatellite point latitude is increasing) 2048 (Bit 12) = spare_13, always zero 4096 (Bit 13) = spare_14, always zero 8192 (Bit 14) = fatal_low_yslf_range_corr_gain, range corrected gain of the DDM used for YSLF winds is < 1 16384 (Bit 15) = spare_15, always zero 32768 (Bit 16) = spare_16, always zero
					65536 (Bit 17) = spare_17, always zero
sum_neg_brcs_values_used_for_nbrcs_flags	Sum of negative BRCS values used for NBRCS flags	byte	1	sample	The number of DDMs utilized to produce wind_speed that used at least one negative BRCS value to calculate NBRCS. Ranges from 1 to 5.

Per-DDM Values

Wind retrievals are produced utilizing from one to five one second averaged DDMs. The values below are five element arrays which contain per-DDM values. The DDMs that were utilized for wind retrieval are indicated by the ddm_obs_utilized_flag array. If less than 5 DDMs are used in the average, the unused positions of such variables are set to a fill value.

ddm_obs_utilized_flag	DDM-utilized flags	byte	1	sample, ddm	A five element array, one for each one second averaged DDM used in the temporal average for the wind speed product. Each element is a flag set to one if the corresponding DDM was utilized to produce wind_speed.
ddm_num_averaged_l1	Number of valid L1 samples averaged	byte	1	sample, ddm	A five element array, one for each DDM used in the temporal average for the wind speed product. Each value is the number of valid L1 samples averaged together to create a one Hz time averaged L1 sample.
ddm_channel	Level 1 DDM reflectometry channels	byte	1	sample, ddm	A five element array, one for each one second averaged DDM used in the temporal average for the wind speed product. Contains the Level 1 netCDF reflectometry channel of the corresponding DDM. Can be utilized together with the ddm_sample_index, spacecraft_num and 'source' to look up the corresponding Level 1 DDM data and metadata.
ddm_les	DDM leading edge slope observables	float	1	sample, ddm	A five element array, one for each one second averaged DDM used in the temporal average for the wind speed product. Contains the corresponding DDM leading edge slope value, unitless.

ddm_nbrcs	DDM normalized bistatic radar cross section observables	float	1	sample, ddm	A five element array, one for each one second averaged DDM used in the temporal average for the wind speed product. Contains the corresponding DDM normalized bistatic radar cross section value, unitless.
Per-Averaged L1 Values Up to 20 L1 DDMs can be contributed to an L2 sample. This dimension acocunts for the up to 4 DDMs that occur within the same second can be averaged together at the start of L2 processing. Up to 5 of those one second averaged L1 DDMs can contribute to an L2 sample. If less than 4 DDMs are used in the average, the unused positions of such variables are set to a fill value.					
ddm_sample_index	Level 1 netCDF sample indices	int	1	sample, ddm, averaged_l1	Contains the Level 1 netCDF sample index of the corresponding DDM. Can be utilized together with ddm_channel, spacecraft_num and 'source' to look up the corresponding Level 1 DDM data and metadata. There can be up to 20 L1 DDMs used for a single L2 sample. Up to 4 samples that occur within the same second can be averaged together to form a one second averaged DDM and up to 5 one second averaged DDMs can contribute to an L2 sample. All non-utilized values will be set to a fill value.

ddm_averaged_l1_utilized_flag	DDM Averaged L1 Utilized flags	byte	1	sample, ddm, averaged_l1	Each element is a flag set to one if the corresponding DDM was utilized to produce wind_speed. There can be up to 20 L1 DDMs used for a single L2 sample. Up to 4 samples that occur within the same second can be averaged together to form a one second averaged DDM and up to 5 one second averaged DDMs can contribute to an L2 sample.